ECOLE MILITAIRE POLYTECHNIQUE

ECOLE ROYALE MILITAIRE

THESE DE DOCTORAT EN SCIENCES

Spécialité : GENIE ELECTRIQUE
Option : ELECTRONIQUE

Présentée par

BOUARABA Azzedine
Magister en Techniques Avancées en Traitement du Signal de l'Ecole Militaire Polytechnique

COHERENT CHANGE DETECTION USING HIGH RESOLUTION SAR IMAGES

Soutenue le 18 / 12 / 2014

Devant le jury

Président:	SMARA Youcef	Professeur / U.S.T.H.B. (Algérie)
Examinateurs:	NEYT Xavier	Professeur / E.R.M. (Belgique)
	KHENCHAF Ali	Professeur / E.N.S.T.A.- Bretagne (France)
	HAMAMI Latifa	Professeur / E.N.P. (Algérie)
	KIMOUCHE Hocine	Maître de Conf. A/ E.M.P. (Algérie)
Rapporteurs:	ACHEROY Marc	Professeur / E.R.M. (Belgique)
	BELHADJ-AISSA Aichouche	Professeur/ U.S.T.H.B. (Algérie)

N° d'enregistrement: …………..

to my parents

to Fadila and Melissa

to my brothers and sisters

Acknowledgments

This doctoral thesis was realized under the joint supervision program between the École Militaire Polytechnique (Algeria), and the Royal Military Academy (Belgium).
The work presented in this thesis was accomplished with the help of many colleagues and friends. The main guidance was provided by my thesis advisors, Professor Marc Acheroy from the Royal Military Academy and Professor Aichouche Belhadj-Aissa, from the USTHB university of Algeria. They taught me InSAR processing in IDL environment and give me constant support during the time of this thesis. Thanks for the confidence you have placed in me.
I am deeply indebted to my committee members: Professor Youcef SMARA, Professor Neyt XAVIER, Professor Ali KHENCHAF, Professor Latifa HAMAMI and Dr. Hocine KIMOUCHE for accepting to assess this modest work.
I also want to thank Damien Closson from RMA, for sharing SAR data and to have taught me InSAR and all the related data processing and interpretations. I would like to thank my colleagues: Frederic Allot, Dirk Borghys, Nada Milisavljevic, Olga Lopera and all researchers of CISS department of RMA for their great hospitality and help make my life in Brussels very easy.
I am very grateful to Dr. Noureddine HANOUN from the USTHB university for reading this manuscript.
I would like to thank the private companies Sarmap and EXELisvis for their support in providing a full Sarscape^{TM} license (v.4.8, 2011) embedded in the ENVI software. Special thanks go to Paolo Pasquali for his support and encouragement and for sharing SAR data.
The majority of the used SAR data (CSK, TSX, ALOS, ENVISAT, ERS) were obtained under the SPARE-SAFE project, launched by the Belgian Ministry of Defense, and processed at the CISS Department of the Royal Military Academy of Belgium. The RADARSAT-2 data were obtained under the SOAR2009 joint project between the LTIR laboratory (USTHB University - Algeria) and the Canadian Space Agency.

Contents

I PREAMBLE **1**

I.1 Introduction . . . 2

I.2 Significance of InSAR coherence images . . . 3

I.3 InSAR coherence mis-estimation . . . 5

I.4 Used SAR data . . . 6

I.5 Outline of the thesis . . . 7

II SYNTHETIC APERTURE RADAR **8**

II.1 Brief history of radar . . . 9

II.2 Radar basics . . . 9

II.3 Radar for remote sensing . . . 11

II.3.1 What is remote sensing ? . . . 11

II.3.2 Why using radar for remote sensing ? . . . 11

II.4 Side Looking Airborne radar . . . 11

II.4.1 Geometry . . . 11

II.4.2 Spatial resolution . . . 12

II.4.3 Geometrical distortions . . . 15

II.5 Synthetic Aperture Radar . . . 18

II.5.1 SAR signal processing and image formation . . . 18

II.5.2 SAR data acquisition modes . . . 20

II.5.3 SAR image interpretation . . . 20

II.5.4 Speckle in SAR images . . . 22

II.5.5 Important SAR data parameters . . . 22

II.6 Summary . . . 23

III SAR INTERFEROMETRY 25

III.1 Introduction . . . 26

III.2 Interferometric configuration . . . 27

III.3 SAR interferometric process . . . 29

III.3.1 SAR images co-registration . . . 29

III.3.2 Interferogram formation . . . 30

III.3.3 Interferogram flattening . . . 32

III.3.4 Interferogram filtering . . . 34

III.4 InSAR coherence and decorrelation sources . . . 40

III.5 Interferometric phase components . . . 43

III.6 Limitation of SAR interferometry . . . 45

III.7 Summery . . . 46

IV INSAR COHERENCE ESTIMATION 47

IV.1 Introduction . . . 48

IV.2 Statistical modeling of decorrelation . . . 48

IV.2.1 Complex PDF SAR resolution cell . . . 48

IV.2.2 Complex PDF interferometric resolution cell . . . 50

IV.2.3 Coherence estimation bias . . . 51

IV.3 InSAR coherence and decorrelation sources . . . 53

IV.3.1 Decorrelation sources . . . 53

IV.3.2 Phase corrected coherence . . . 56

IV.4 Coherence of high resolution SAR images . . . 56

IV.4.1 Influence of the SAR speckle in InSAR coherence . . . 56

IV.4.2 Influence of the number of samples N . . . 59

IV.5 Conclusion . . . 60

V INSAR COHERENCE IMPROVEMENT 61

V.1 Introduction . . . 62

V.2 Coherent Change Detection . . . 62

V.2.1 Mean Level Detector (MLD) . . . 63

V.2.2 Ordered Statistic (OS) detector . . . 63

V.2.3 Censored Mean Level Detector (CMLD) . . . 64

V.2.4 Guard Cell (GC) to improve detection performance . . . 64

V.3 Experimental evaluation of the ROC curves . . . 65

V.4 Improving CCD performance by using LFF 68
V.4.1 LFF estimation 69
V.4.2 LFF-based cleaning method 71
V.4.3 LFF-based adaptive method 72
V.5 Application for earthquakes damages assessment 77
V.6 Conclusion 82

VI CHANGE CLASSIFICATION **84**
VI.1 Introduction 85
VI.2 Classification scheme 86
VI.3 Overview of the dataset 88
VI.4 Application in agricultural environment 90
VI.4.1 Agricultural area 91
VI.4.2 Urban area 92
VI.5 Application in a harbor environment 92
VI.5.1 Sea area 95
VI.5.2 Container terminal area 96
VI.6 LFF-based cleaning method versus LFF-based adaptive method 97
VI.7 Application to monitoring man-made changes 99
VI.8 Summary 102

VII CONCLUSION **104**
VII.1 Summary of our contributions 106
VII.2 Future work 108

References **114**

APPENDIX **115**

A MUSIC FOR LFF ESTIMATION **116**

List of Figures

I.1 Geocoded InSAR coherence image evaluated over the ERS repeat-pass images of 29 July and 10 october 1995. Light-colored pixels represent high values of coherence, while dark pixels represent low values. 4

II.1 Basic block diagram of full-polarimetric radar system. 10
II.2 Geometry of a Side Looking Radar. 12
II.3 The geometric difference between slant and ground ranges. 13
II.4 A geometrical view of four targets. Targets A and B will be inseparable in the radar image since they are separated by less than half a pulse length. Targets C and D will give separate responses in the image because they are separated by more than half a pulse length. 14
II.5 Range resolution: pulses. The equivalent of Figure II.4 in terms of pulses received by the radar. 14
II.6 Azimuth resolution of SLAR. 16
II.7 Foreshortening: length BC appears much shorter in slant range than in ground range. 16
II.8 Layover: point C appears before point B in slant range. 17
II.9 Shadow: terrain blocks radar signal. 17
II.10 Synthetic Aperture principle. The target is in many radar returns, from a real antenna length L, moving along track. Processing can synthesize a large antenna length L_{synth} characterized by a fine beam. 19
II.11 Range-doppler processing. 19
II.12 SAR scanning modes. 20

II.13 Part of the Zeebrugge harbour (Belgium) imaged with SAR and optical sensors. (a) CSK SAR intensity image acquired in spotlight mode (sub-set size of 200 × 200 pixels). (b) Optical image from Google Earth™ of the site of interest. COSMO-SkyMed™ Product - ASI [2011] processed under license from ASI - Agenzia Spaziale Italiana. All rights reserved. 21

III.1 Interferometric configuration. Satellite positions 1 and 2 have ranges, to target P, R_1 and R_2 respectively. The separation between the satellites is called the spatial baseline and is denoted by B. 27

III.2 SAR images co-registration. 30

III.3 CSK intensity image of a flat area in Goma (R. D. of Congo). Sub-set size of 1400 × 1400 pixels, acquired in spotlight mode. COSMO-SkyMed™ Product - ASI [2011] processed under license from ASI - Agenzia Spaziale Italiana. All rights reserved. 31

III.4 SAR interferogram of the area shown in Figure III.3. Baseline: $B_\perp = 307$ m $\rightarrow z_{2\pi} =$ 15 m. The time delay between the two acquisitions is 4 days. 32

III.5 Interferograms spectrum. (a) Original interferogram, (b) Flattened interferogram. 33

III.6 Flattened interferogram of Figure III.4 using the fringe-frequency algorithm. 34

III.7 Result of Goldstein filter: same interferogram as Figure III.6. Baseline: $B_\perp = 307$ m $\rightarrow z_{2\pi} =$ 15 m. The time delay between the two acquisitions is 4 days. COSMO-SkyMed™ Product - ASI [2011] processed under license from ASI - Agenzia Spaziale Italiana. All rights reserved. 36

III.8 Formulation of joint spatial steering vector using a 3 × 3 pixel pair window. 37

III.9 Horizontal interferometric phase profiles. 39

III.10 Result of the complex multilooking (by factor 2 in both range and azimuth direction) followed by Goldstein filtering for the same interferogram as Figure III.7. 40

III.11 Schematic representation of the different steps used for coherence evaluation in case of a CCD application. 42

III.12 Sample coherence evaluated over the repeat-pass image pair using $N = 3\times3$ pixel spatial estimation window: same area as Figure III.6. Light-colored pixels represent values of InSAR coherence near 1, while dark pixels represent values near 0. (1) Undisturbed parcels characterized by high coherence values, (2) Cultivated parcel with low coherence values, and (3) Natural vegetated area that is affected by volumetric decorrelation. COSMO-SkyMed$^{\mathrm{TM}}$ Product - ASI [2011] processed under license from ASI - Agenzia Spaziale Italiana. All rights reserved. 43

III.13 Interferometric products of Zeebrugge port obtained using two CSK SAR images: covering same area as in Figure II.13. Baseline: $B_{\perp}$= 22 m $\rightarrow z_{2\pi}$= 231 m. (a) Interferometric phase: (1) Topographic fringe of the port quay, (2) Phase change corresponding to the sea area, and (3) Displacement fringes of the floating barge. (b) Coherence image obtained by $N = 5 \times 5$ pixel spatial estimation window. 45

IV.1 Summation of scatterers responses within a resolution cell k. (a) The distribution of N individual scatterers within a resolution cell. (b) All scatterers translated to the same origin. (c) The sum of all scatterers. The bold arrow indicates the sum, which is the complex observable s_k. 49

IV.2 Probability density function for different number of looks of: (a) interferometric phase. (b) Coherence (ϕ_0 is assumed to be zero and $|\gamma| = 0.5$). . . . 52

IV.3 Bias of the coherence estimate for different values of N. 53

IV.4 Schematic diagram for studying the influence of the SAR speckle on coherence estimation. N is the number of samples used for the coherence estimation. L_r and L_a are the multilooking factors respectively in range and azimuth direction. 57

IV.5 Influence of the complex multilooking operation into the interferometric products. (a) Interferometric phase obtained without complex multilooking. (b) Interferometric phase obtained with a complex multilooking factor of 2 (both in range and azimuth directions). (c) Coherence image obtained without complex multilooking. (d) Coherence image obtained with a complex multilooking factor of 2 (both in range and azimuth directions). . . . 58

IV.6 Coherence histograms evaluated for different values of N. (a) Coherence of changed and unchanged areas obtained without complex multilooking. (b) Coherence of changed and unchanged areas obtained using complex multilooking. 59

V.1 General scheme of the CCD map generation process. 63
V.2 Spatial correlation of the coherence samples. 64
V.3 Moving window configurations. (a) Classical moving window. (b) Moving window with incorporation, in range direction, of two guard cells directly adjacent to the pixel under test. 65
V.4 Experimental probability of false alarm versus threshold T. $M = 3 \times 3$, $n_{os} = 5$ and $k = 5$. 66
V.5 Change detection results for $P_{fa} = 5 \times 10^{-3}$. (a) MLD change map with $M = 1 \times 1$, $T = 0.556$, and $P_d = 0.734$. (b) MLD change map with $M = 3 \times 3$, $T = 0.656$, and $P_d = 0.958$. (c) CMLD change map with $M = 3\times3$, $T = 0.603$, $k = 5$, and $P_d = 0.968$. (d) CMLD (with GC)change map for $M = 3 \times 3$, $T = 0.587$, $k = 5$, and $P_d = 0.994$. 67
V.6 Experimental ROC curves corresponding to coherence of Figure III.12. $M = 3 \times 3$, $n_{os} = 5$ and $k = 5$. 68
V.7 Histograms of the statistic z_4 in the selected changed and unchanged areas of Figure III.12. 70
V.8 Scheme of the LFF-based cleaning method. 71
V.9 Experimental ROC curves of the LFF-based cleaning method. Number of samples $N = 3 \times 3$. 72
V.10 CCD results for $N = 3 \times 3$ and $P_{fa} = 10^{-3}$. (a) MLD change map with $M = 1$ and $P_d = 0.64$. (b) MLD change map with $M = 3\times3$ and $P_d = 0.94$. (c) Change map with the LFF-based cleaning method, $M = 3 \times 3$ and $P_d = 0.99$. (d) Zoom on a cultivated parcel. 73
V.11 Scheme of the LFF-based adaptive method. 74
V.12 Experimental ROC curves of the two LFF-based methods. 74
V.13 Optical image from Google Earth of the test site. The rectangle indicates the area of interest corresponding to the SAR image sub-chip size of 1000×1000 pixels. 75

V.14 Coherence map of the Zeebrugge harbour. Sub-set size of 1000×1000 pixels, and $N = 3 \times 3$. COSMO-SkyMed^{TM} Product-ASI [2011] processed under license from ASI-Agenzia Spaziale Italiana. All rights reserved. . . . 76

V.15 SAR intensity images and CCD results. (a) SAR intensity image of 15 June, 2011. (b) SAR intensity image of 19 June, 2011. (c) CCD map obtained with fixed-size window of $N_1 = 3 \times 3$ samples. (d) CCD map obtained with the adaptive method. 77

V.16 Zoom on unmoved vehicles surrounded by surface changes. (a) SAR image intensity of 15 June, 2011. (b) SAR image intensity of 19 June, 2011. (c) CCD map obtained with fixed-size window of $N_1 = 3 \times 3$ samples. (d) CCD map obtained with the proposed adaptive method. (e) CCD map obtained with fixed-size window of $N_2 = 5 \times 5$ samples. Sub-chip size of 70×70 pixels. The vehicles 1, 2 and 3 in (b) are unmoved between the two dates. . 78

V.17 (a) Linwood Avenue and its neighborhood. Black dots correspond to GPS track of the field survey carried out in April 2011. (c) Seismic waves' absorption sites recorded during the 22-Feb-11 aftershock (center and upper left corner). (b) and (d): Comparison with the ground deformations recorded in September 2010 and June 2011 events. 79

V.18 (a) and (b): Coherence images for the 22-Feb-11 and 13-Jun-11 events; (c) and (d): same information but enhanced to define the boundaries of the areas having preserved the coherence (white color) after the tremors. Red dots correspond to GPS tracks recorded in April 2011. Green square represents an area of 1×1 km (see Figure V.19) over a representative segment of boundary between high and low coherence. 80

V.19 (a) 1×1 km color orthophotography at 10 cm resolution (www.koordinates.com, accessed 03-Jun-2013) used to map soil liquefaction, roof and building collapses; (c) detailed view, red line are vectors digitized in the GIS; (b) enhanced coherence image of the 22-Feb-11 event with polygons of damages, essentially liquefaction. Green lines come from GPS deformation map realized by GNS Science; (d) enhanced coherence image of the 13-Jun-11 event and the same polygons than in (b). 82

VI.1 Schematic overview of the change detection and classification scheme. . . . 86

VI.2 Histograms of the learning set. 87

VI.3 Optical image from Google Earth of Maymana (Afghanistan). The red rectangle indicates the test area that corresponds to the available CSK SAR images of 19255×14403 pixels size. © Google Earth 2012. All rights reserved. 89
VI.4 CSK SAR intensity image of the Maymana region (Afghanistan), sub-set size of 4000×4000 pixels. COSMO-SkyMed^{TM} Product - ASI [2010] processed under license from ASI - Agenzia Spaziale Italiana. All rights reserved. 90
VI.5 Change classification results of the agricultural area in Maymana (Afghanistan), sub-set size of 320×320 pixels. (a) CSK SAR image intensity of January 1, 2010. (b) coherence image evaluated by using 3×3 pixel spatial estimation window. (c) Change classification result obtained by the classical MLD method. (d) Change classification result obtained by the proposed LFF-based cleaning method. 91
VI.6 Change classification results of the urban area in Maymana (Afghanistan), sub-set size of 320×320 pixels. (a) CSK SAR image intensity of January 1, 2010. (b) coherence image evaluated by using 3×3 pixel spatial estimation window. (c) Change classification result obtained by the classical MLD method. (d) Change classification result obtained by the proposed LFF-based cleaning method. 93
VI.7 Optical image from Google Earth of the Zeebrugge harbor (Belgium). The red rectangle indicates the test area that corresponds to the available CSK SAR images of 15312×14486 pixels size. © Google Earth 2012. All rights reserved. 94
VI.8 CSK SAR intensity image of the Zeebrugge harbor (Belgium), sub-set size of 2000×2000 pixels. COSMO-SkyMed^{TM} Product - ASI [2011] processed under license from ASI - Agenzia Spaziale Italiana. All rights reserved. . . 94
VI.9 Change classification results of the selected sea area in Zeebrugge (Belgium), sub-set size of 300×200 pixels. (a) CSK SAR image intensity of June 15, 2011. (b) coherence image evaluated by using 3×3 pixel spatial estimation window. (c) Change classification result obtained by the classical MLD method. (d) Change classification result obtained by the proposed LFF-based cleaning method. 95

VI.10 Change classification results of the container terminal area in Zeebrugge (Belgium), sub-set size of 300×300 pixels. (a) CSK SAR image intensity of June 15, 2011. (b) coherence image evaluated by using 3×3 pixel spatial estimation window. (c) Change classification result obtained by the classical MLD method. (d) Change classification result obtained by the proposed LFF-based cleaning method. 97
VI.11 Change classification results. (a) RGB color composition of test area, Red: coherence image, Green: CSK SAR image intensity of June 15, 2011 and Blue: CSK SAR image intensity of June 19, 2011. (b) Fixed window of 3×3 samples. (c) LFF-based adaptive method. (d) LFF-based cleaning method. (e) Fixed window of 5×5 samples. Sub-set size of 220×220 pixels. 98
VI.12 Change classification results: Zoom on unmoved vehicles. (a) RGB color composition of test area, Red: coherence image, Green : CSK SAR image intensity of June 15, 2011 and Blue: CSK SAR image intensity of June 19, 2011. (b) Fixed window of 3×3 samples. (c) LFF-based adaptive method. (d) LFF-based cleaning method. (e) Fixed window of 5×5 samples. Sub-set size of 60×60 pixels. 99
VI.13 Geographical location of the test site in Goma, in the Democratic Republic of Congo, that is characterized by a flat topography. The rectangle indicates the imaged scene corresponding to the used CSK SAR images of 14568×14376 pixels. 100
VI.14 Change classification results. (a) Visible image of the test site. (b) CSK SAR image intensity of 3/24/2011. (c) Coherence map of 3/24 and 3/28/2011. (d) Change classification result of 3/24 and 3/28/2011. (e) Coherence map of 3/28 and 4/1/2011. (f) Change classification result of 3/28 and 4/1/2011. 101

List of Tables

I.1 Overview of the used SAR images. 6

VI.1 Overview of the eight classes resulting from the change detection and classification. 88

VI.2 Overview of the COSMO-SkyMed SAR images characteristics used in the validation process. 89

List of Symbols

The values between brackets are those of the satellite ERS.

θ	Incident angle ($\approx 20°$)
λ	Radar wavelength (5.66 cm)
τ	Pulse length
s	Radar signal
n	Additive noise
f_c	Carrier frequency (5.3 GHz)
B_s	Pulse modulation bandwidth (15.5 MHz)
PRF	Pulse Repetition Frequency (between 1640 and 1720 Hz)
R_A	Azimut resolution
R_s	Slant range resolution
R_G	Ground range resolution
L	Real radar antenna length (10 m)
R	Distance antenna-object
ϕ	Interferometric phase
$I(\cdot)$	Interferogram
B	Geometric (spatial) baseline
$B_\perp$	Perpandicular (normal) baseline
$h_{2\pi}$	Altitude ambiguity
γ	InSAR coherence
γ_{SNR}	Decorrelation determined by the SNR
γ_{proc}	Decorrelation related to mismatch between primary and repeat-pass imagery
γ_{base}	Baseline decorrelation
γ_{vol}	Volumetric decorrelation
γ_{temp}	Temporal decorrelation

z	Detection statistic
T	Detection threshold
P_d	Detection probability
P_{fa}	False alarm probability
H_0	Null hypothesis (scene changes of interest absent)
H_1	Alternative hypothesis (scene changes of interest present)
N	Local window size (coherence estimation)
M	Local window size (space averaging)

List of Abbreviations

ALOS	Advanced Land Observing Satellite (Japanese Satellite)
ASI	Agenzia Spaziale Italiana
ESA	European Spatial Agency
RADAR	RAdio Detection And Ranging
RAR	Real Aperture Radar
SLC	Single Look Complex
SAR	Synthetic Aperture Radar
SLAR	Side Looking Airborne Radar
ERS	European Remote Sensing
ENVISAT	Environmental Satellite (Launched by the ESA)
ASAR	Advanced Synthetic Aperture Radar
CSK	COSMO-SkyMed: Constellation Of small Satellites for Mediterranean basin Observation (Italian Satellite)
RADARSAT	RADAR Satellite (Canadian Satellite)
TSX	TerraSAR-X (German Satellite)
SIR	Shuttle Imaging Radar (USA Satellite)
SEASAT	Sea Satellite (USA Satellite)
SRTM	Shuttle Radar Topography Mission
DTM	Digital Terrain Model
CCD	Coherent Change Detection
LFF	Local Fringe Frequencies
IDL	Interactive Data Language
InSAR	Interferometric Synthetic Aperture Radar
PolSAR	Polarimetric Synthetic Aperture Radar
PolInSAR	Polarimetric Interferometric Synthetic Aperture Radar
D-InSAR	Differential InSAR

LOS	Line Of Sight
RDP	Range Doppler Processing
PS	Permanent Scatterers
SBAS	Small baseline Subset
PDF	Probability Density Function
SNR	Signal to Noise Ratio
OS	Ordered Statistic
MLD	Mean Lavel Detector
CMLD	Censored MLD
GC	Guard Cell
ROC	Receiver Operating Characteristics
GIS	Geographic Information System
GPS	Global Positioning System
CRB	Cramer-Rao Bound
MUSIC	MUltiple Signal Classification
ML	Maximum Likelihood

$\boxed{\text{CHAPTER I}}$

PREAMBLE

I.1 Introduction

The temporal evolution of the landscape which is exemplified by changes in the cities' extension, sudden or slow deformations of the Earth's surface, critical infrastructure stability, has prompted the international scientific community to design systems enabling the surveillance at different scales in order to monitor and control any changes of the earth's surface. It is in this context that our research work is taking place. We are dealing with the overall processing chain dedicated to the measurement of changes in strategic and sensitive areas by using Earth observation systems. In particular, we are focusing on detection and mapping of ground changes using remote sensing techniques.

Change detection is the process of identifying differences in the state of an object by observing it at different times. The temporal, spatial, spectral and radiometric resolutions of remotely sensed data have a significant impact on the success of a remote sensing change detection application. In the literature, change detection problems are generally addressed for specific types of sensors (i.e. passive or active). In change detection using passive sensors (e.g., optical images), the difference image is usually evaluated and provides a valid change measure. However, the use of optical images remains limited in cloudy or rainy regions. From this point of view, Synthetic Aperture Radar (SAR) imagery can be considered as the best alternative for remote sensing applications [1].

SAR sensors have the capability of acquiring images night and day, regardless of the weather conditions. SAR sensors can monitor and survey wide ground surfaces from a long range and have some penetrability. Moreover, SAR sensors provide complex images where both amplitude and phase carry information which may be useful for change analysis. All of these advantages give SAR data a great potential for change detection applications [2].

Change detection with remote sensing SAR images involves a pair of co-registered images acquired over the same area at different times. To identify changes, different methods are commonly applied. These methods differ with respect to the parameters that are used to indicate changes. Since SAR data contain amplitude and phase information, more than one parameter could be used as a change indicator. Two forms of change detection in repeat-pass SAR imagery may be considered, namely coherent and incoherent change detection. Incoherent change detection identifies changes using only the backscattered power taken from the repeat pass image pair. Typically, sample estimates are obtained by spatially averaging the image pixel intensities over local regions in the image pair [1].

The presence of speckle in SAR data limits the application of incoherent change detection methods and the speckle filtering is still a challenging problem [3].
Coherent Change Detection (CCD), on the other hand, uses the magnitude of the sample complex cross correlation (i.e. coherence) of an Interferometric SAR (InSAR) image pair to quantify changes in the observed amplitude and phase of the image pixels [4, 5]. In this technique, an InSAR process is required to evaluate the coherence image. At the origin, InSAR coherence was used to guide phase filtering and unwrapping in the Digital Terrain Model (DTM) generation process [6, 7]. Then, the InSAR coherence image that is highly sensitive to the scene disturbance became the basic input parameter for most CCD methods. Indeed, ground changes of the order of the centimeter significantly increase the interferometric phase variance in the impacted resolution element. This change shows a decorrelation or a decrease in InSAR coherence [8], which offer to CCD methods the potential to detect very subtle scene changes that may remain undetectable using incoherent techniques [5].
The main objective of the present thesis is to propose and validate a methodological approach based on InSAR coherence, for mapping fine ground changes. This consists mainly of four blocks of processing and analysis of the InSAR data as following:

1. The development of an interferometric SAR process including interferogram formation, flattening and filtering.

2. InSAR coherence estimation using high resolution SAR images. This includes the developed methods of coherence improvement based on using the interferometric phase variability as a second change information.

3. The development of an efficient change classification scheme that permits the overall scene analysis. This consists of using SAR intensity images in addition to the corresponding improved coherence map, to identify the man-made changes of interest.

4. Testing and validating the developed approach using suitable test sites.

I.2 Significance of InSAR coherence images

InSAR coherence provides a quantitative measure of surface property change during the time span of the interferometric pair. Since InSAR coherence is a measure of the degree of similarity between two SAR images, high coherence values indicate no change while low

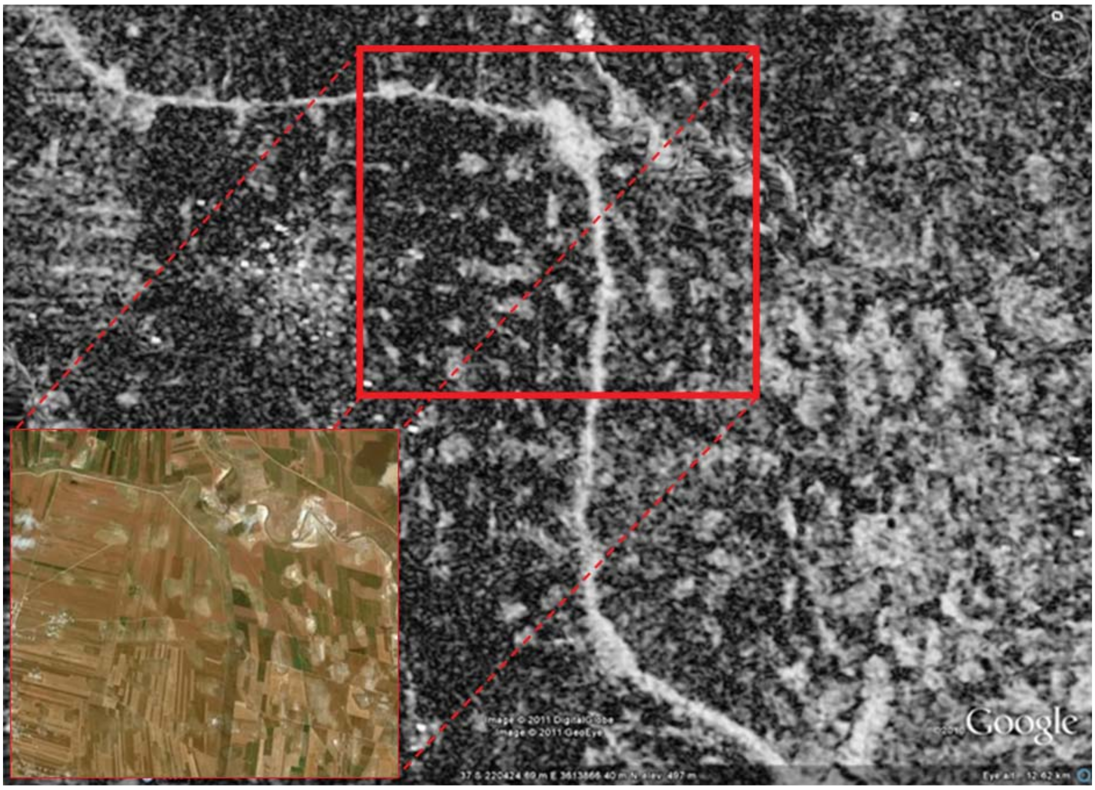

Figure I.1: Geocoded InSAR coherence image evaluated over the ERS repeat-pass images of 29 July and 10 october 1995. Light-colored pixels represent high values of coherence, while dark pixels represent low values.

coherence implies changes in the observed scene. Zebker et al. [9] used coherence to detect changes due to lava flow on the Kilauea volcano with SIR-C, while Dietterich et al. [10] used coherence images from ENVISAT to track the same volcano. InSAR coherence is widely used for earthquake damage assessment. Simons et al. [11] used coherence image from ERS for mapping ground surface disturbances caused by intense shaking during the 1999 Hector Mine earthquake. Fielding et al. [12] and Hoffman et al. [13] used coherence to map surface ruptures and damages to the city of Bam, Iran. InSAR coherence is also used for man-made change detection. Milisavljevic et al. [14] used coherence from ENVISAT pair images to detect potential human activities.
To show the ability of the InSAR coherence to measure ground changes, an example of coherence image of an agricultural area at the border between Jordan and Syria is presented in Figure I.1. The interferometric SAR process of Figure I.1 is achieved using ERS image pair over an area of 10 km $\times$ 6 km and with a ground pixel resolution of 20 m. The coherence of the cultivated fields appears to be low (dark pixels) on one side which indicates the existence of agricultural activities during the acquisition times. on

other side, the urban area (left side of Figure I.1) is characterized by high coherence values (light-colored pixels). The uncultivated parcels on the right side of Figure I.1 are also characterized by high coherence values. Notice the white continuous diagonal band (about 100 m wide) on the coherence image, which corresponds to the no man's land (minefield) separating Jordan and Syria. Despite a temporal interval of 70 days, coherence is preserved (high values) because no human activities took place in the minefield area. Optical images cannot deliver this type of information about the minefield regardless of spectral band and pixel resolution. This is due to the fact that the temporal changes (i.e. no changes) are mainly indicated by the interferometric phase, a parameter that does not exist in optical imagery and is not used in incoherent change detection methods. The example in Figure I.1 clearly shows the importance of using InSAR coherence as a ground change indicator.

I.3 InSAR coherence mis-estimation

The recent advent of satellite constellations that deliver high-resolution SAR images made it possible to detect surface changes with fine spatial details and short temporal baseline. These advantages make CCD techniques ideal for use in military and scientific applications such as border security and environmental monitoring. All of these advantages led to the development of new methods that improve change detection performance [4, 5, 14]. Unfortunately, the sample coherence estimator is biased, especially for low-coherence values [15]. The cause of this bias, in addition to the presence of speckle in SAR data [16], is the appearance of highly coherent pixels inside changed areas which are considered as outliers. Within this context, the detection performance will considerably degrade, particularly when using high-resolution SAR data [17].
As demonstrated in [15], the bias decreases when the number of samples used to estimate the coherence increases. However, a large number of samples also causes the loss of subtle changes in the coherence image. Touzi et al. [15] proposes a method to reduce the bias by space-averaging coherence samples over a local area. This method allows the improvement of detection performance but a large window size is needed to detect all the changes. For that reason, another change information source is suitable to better analyze the InSAR coherence image. This idea is one of our important contributions in the present work.

Country	Satellite	Nbr. of SAR images	Pixel Resolution (m)	Polarization
Libya	ALOS	4	20	HH
Egypt	ALOS	4	10	HH, HV, VH and VV
Syria	ERS1-2	2	20	HH
Jordan	ENVISAT	2	20	HH
Algeria	ERS1-2	2	20	HH
Algeria	RADARSAT-2	2	10	HH, HV VH and VV
Afghanistan	CSK	6	1	HH
Belgium	CSK and TSX	8	1	HH
D. R. of Congo	CSK	4	1	HH
New Zealand	CSK	8	1	VV

Table I.1: Overview of the used SAR images.

I.4 Used SAR data

For the test and validation of the proposed change detection approach, various SAR data sets has been used as presented in Table I.1. The data delivered by the satellites ALOS, ERS, ENVISAT and RADARSAT-2 are of medium resolution with ground pixel size of about 20 m. The high resolution SAR data are delivered by the two satellites TSX and CSK with ground pixel resolution of about 1 m.

The advantage of using high-resolution SAR data, in addition to the detection of fine changes, is that it is possible to select faithfully large changed and unchanged areas as ground truth in order to assess the validity of the developed change detection methods. The probability of detection and false alarm are estimated experimentally and the Receiver Operating Characteristic (ROC) curves are used to quantify the change detection performance.

Co-registration of the SAR images is performed with Sarscape^{TM}. Developments are carried out using Interactive Data Language (IDL). During the validation process, various high resolution visible images have served as ground truth and the final geocoded change maps were visually assessed using ArcMap^{TM} Geographical Information System (GIS).

I.5 Outline of the thesis

The thesis is broadly organized into two parts: conventional SAR Interferometry and improvement of the coherent change detection technique. The first part consists of chapters II, III and IV and is organized as follows. Chapter II gives an introduction to Synthetic Aperture Radar, outlining the basics of radar remote sensing and image geometry. Chapter III introduces interferometric techniques for SAR processing. The steps for producing interferograms are discussed. Particular attention has been given to the phase filtering, which is of great importance for the success of all InSAR processing. The subspace projection based filter is presented, together with our contribution in the improvement of the phase estimation. Chapter IV gives an overview of sample coherence estimation.

The second part of the thesis is dedicated to the improvement of the CCD technique and consists of two chapters V and VI. Chapter V proposes several methods to improve the change detection performance. It then goes on to describe the use of Local Fringe Frequencies (LFF), which measures the interferometric phase variability, as additional change information to better analyze InSAR coherence. In this chapter, two proposed LFF-based methods are presented and tested. Chapter VI describes the proposed change classification scheme in order to obtain reliable change maps. A comparative study of the change classification results obtained with and without introducing the LFF information to the change classification is performed. A set of high resolution CSK SAR data are selected for the validation process, which concerns different types of environments; agricultural region in Maymana (Afganistan), harbour in Zeebrugge (Belgium) and airport in Goma (Democratic Republic of Congo). Various results are presented and discussed to assess the validity of the proposed approach.

CHAPTER II

SYNTHETIC APERTURE RADAR

II.1 Brief history of radar

Radar is an acronym for RAdio Detection And Ranging. The basic use of a radar is as a measuring device, whether it be for distance or time. It operates in the microwave portion of the electromagnetic wave scale, usually with wavelengths between 1 mm and 1 m. The first pulse radar system was developed in 1934 with operating frequency 60 MHz by Naval Research Laboratory (NRL), USA. At the same time, radar systems for tracking and detection of aircraft were developed both in Great Britain and Germany during the early 1930s [18]. The evolution from using radar as a location device to an imaging tool came with the application of the Side Looking Airborne Radar (SLAR) in the 1950s. Scanning had been achieved with the SLAR by fixed beam pointed to the side with aircraft's motion moving the beam across the land. The early versions of SLAR systems were primarily used for military reconnaissance purposes. In the mid 1960s, the first high-resolution SLAR image was declassified and made available for scientific use. In the 1970s, the SLAR image was used for many land mapping campaigns. One such campaign involved mapping 500000 km^2 of the United States [19]. From this work in SLAR, the design of Synthetic Aperture Radar (SAR) systems was born.
Synthetic Aperture Radar (SAR) relies on the use of signal processing techniques to improve the resolution beyond the limitation of physical antenna aperture [20]. SEASAT, launched in June 1978, was the first civilian SAR satellite. This was followed by the Shuttle Imaging Radar missions and Soviet missions of the 1980's. In the early 1990's, three more satellites bearing SAR were launched: the European ERS-1, Japan's JERS-1 and the Soviet's ALMAZ-1. These were quickly followed by Canada's RADARSAT-1 and ERS-2 in the mid 1990's, and by European's ENVISAT and USA's Shuttle Radar Topography Mission (SRTM) in February 2000. The recent developments in the high resolution SAR data sources, such as RADARSAT-2 from Canada, the COSMO-Skymed satellite from Italy and the German TerraSAR-X, give the opportunity of mapping with much finer level of detail and the SAR data will be available for at least the next decade at X- (3 cm), C- (6 cm) and L-band (24 cm) wavelengths.

II.2 Radar basics

Radar is an active sensor; it emits a pulse of electromagnetic radiation from the transmitting antenna and then listens for the returning echo at the receiving antenna. Most radar

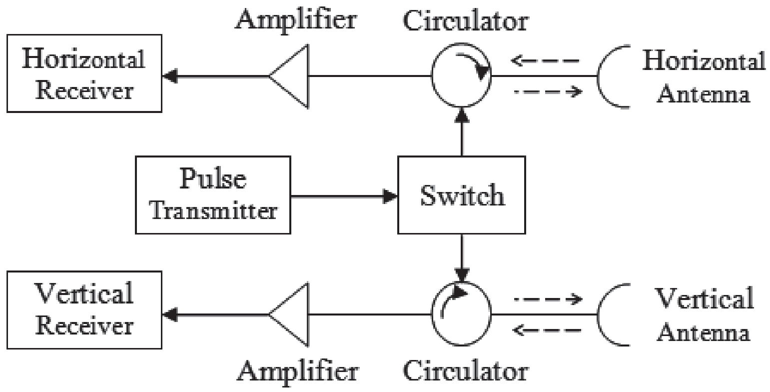

Figure II.1: Basic block diagram of full-polarimetric radar system.

systems are mono-static as they use the same antenna for transmitting and receiving. When the return pulse is received various signal parameters are stored. These can include the amplitude and the phase of the return signal [18]. The Doppler shift and the time delay between transmit and receive can also be derived. The time delay, τ, can be used to calculate the range distance using the simple equation $r = c\tau/2$, where r is the range and c the speed of light. Throughout the scanning of the scene and with the ordering of return pulses, it is possible to form the radar image. In radar imaging systems, the emitted waves are generally linearly polarised in 2 directions horizontal (H) and vertical (V). The wave scattered by a target at the Earth surface is partially depolarized. However, modern radar systems are designed to record the two polarizations. Two letters thus define the polarization of a radar imaging system. The first letter (H or V) designates the polarization of the emitted wave while the second letter refers to the recorded component. A radar image noted HV is obtained with emitting in horizontal polarization and recording in a vertical polarization. Generally, radar emits a signal in a single plane and records the backscattered signal in the same or in the other plane. The full-polarimetric radar is able to emit and to record the complex signal simultaneously in the 2 polarizations. Figure II.1 shows the basic block diagram of full-polarimetric radar system [21]. The pulses are transmitted through a horizontal polarized antenna and received signal from both antennas, then followed by pulses transmitted through a vertical polarized antenna and received by both antennas. Circulators permit a single antenna to be used for both transmission and reception.

II.3 Radar for remote sensing

II.3.1 What is remote sensing ?

Remote Sensing is a term used to describe a group of techniques that can give information about something without physical contact with the object [19]. Remote sensors collect data by detecting the energy that is reflected from Earth. These sensors can be on satellites or mounted on aircraft. Remote sensing makes it possible to collect data on dangerous or inaccessible areas and can be applied in various fields; namely agriculture, forestry, geology, land cover/change, hazard, fire, pollution, hydrology, and other environmental areas.

II.3.2 Why using radar for remote sensing ?

Comparing to optical sensors, radar uses relative long wavelengths which allows these systems to "see" through clouds. Also, being an active system, it can be operated day or night, no matter if there is sunlight or not, giving it an advantage over optical sensors [19]. This allows the interpretation of the radar images no matter if the sky was overcast or not. These two reasons show the benefits of using radar where optical imaging might fail, but another reason to use radar is that it gives complimentary information compared to an optical image [22]. Also, microwaves are able to penetrate vegetation and soil depending on the wavelengths used and the water content of the soil.

II.4 Side Looking Airborne radar

Side Looking Airborne Radar (SLAR) is an aircraft- or satellite-mounted imaging radar. As its name suggests, it is pointed perpendicular to the direction of travel at an angle above the nadir. This angled perspective is necessary because this causes a delay between the parts of the returned pulse that are the farthest from the antenna and the parts that are the closest.

II.4.1 Geometry

The geometry of the Side Looking Radar is shown in Figure II.2. The radar moves in the azimuth direction and looks into the range direction. The satellite track is the path the satellite follows projected onto the ground surface in the nadir direction. The azimuth beamwidth of the radar is equal to λ/L, and determines the size of the area illuminated,

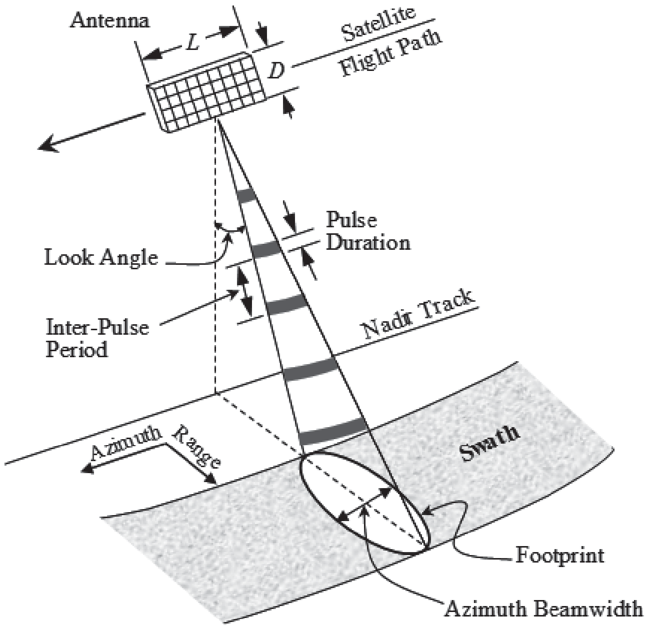

Figure II.2: Geometry of a Side Looking Radar.

in the azimuth direction, of each pulse. The swath width, or size of the illuminated area in the range direction, is determined by the elevation beamwidth which is equal to λ/D. This together with the look angle determines the imaged area . The edge of the radar image nearest to the radar is called near-range, and the farthest is called far-range.

As the radar moves along, it flies in a straight line emitting short pulses at a rate called the Pulse Repetition Frequency (PRF). The returns of each one of these pulses makes up a range line in the radar image. The pulse returns are arranged parallel so as to form an image. Each pixel of the image has two associated coordinates: an azimuth time coordinate which gives the time the range line was imaged, and a range time coordinate which gives the elapsed time between transmitting and receiving the pulse echo. The term range can be confusing when discussing radar images; the terms slant-range and ground-range are used to distinguish between distances relating to radar geometry and ground respectively. This is illustrated in Figure II.3, where S is the position of the antennas, and the range between two targets A and B is shown in both slant range and ground range.

II.4.2 Spatial resolution

Spatial resolution is defined as the shortest distance between two points such that they can be distinguished as separate points in the radar image. The spatial resolution can be

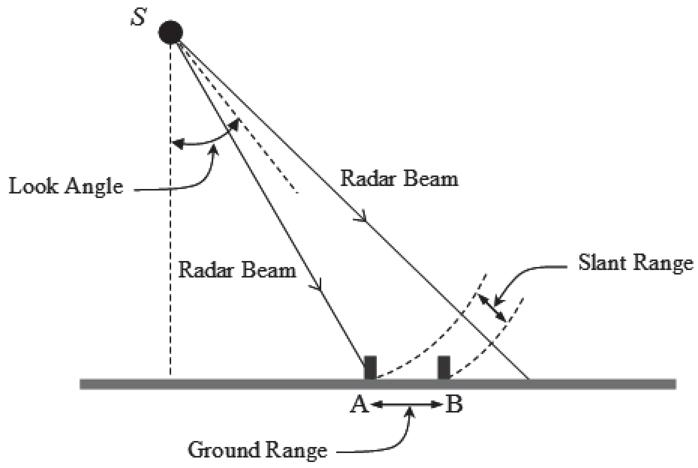

Figure II.3: The geometric difference between slant and ground ranges.

described in two separate parts; *range resolution* and *azimuth resolution*.

Range resolution

The range resolution describes the spatial resolution in the range direction, i.e. for each pulse, that is the minimum separation (in ground-range) of two targets such that they can be resolved in the radar image. This is equivalent to having two separate echoes received at the radar. For this to occur, the separation of the two targets (A and B) must be such that the pulse cannot travel from point A to B and back to A again before the whole pulse has been reflected from A [20]. That is, the two targets A and B must be separated by a distance (in slant range) greater than half the pulse length. Figure II.4 shows this from a geometrical point of view. Two objects A and B will not give two resolvable echoes, whereas the two targets C and D will be discernible. Figure II.5 shows the same thing in terms of the pulse responses. This implies that a shorter pulse width will give a better spatial resolution in the range direction, as Equation II.1 shows,

$$R_G = \frac{R_s}{sin(\theta)} = \frac{c\tau}{2sin(\theta)} \tag{II.1}$$

where R_G is the ground range resolution, R_s the resolution in slant range, τ is the pulse length and θ the incident angle (look angle).
In practice, the pulsewidth of the radar is limited by hardware constraints and the amount of "energy on target" required to get sufficient Signal to Noise Ratio (SNR) to obtain a good image [20]. To achieve a high range resolution without a short pulse, frequency

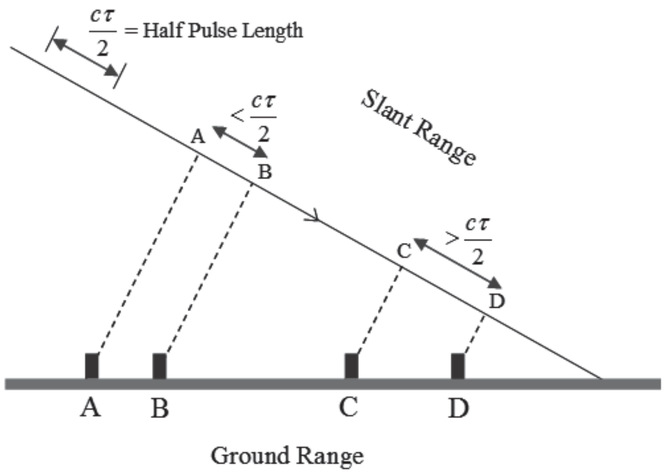

Figure II.4: A geometrical view of four targets. Targets A and B will be inseparable in the radar image since they are separated by less than half a pulse length. Targets C and D will give separate responses in the image because they are separated by more than half a pulse length.

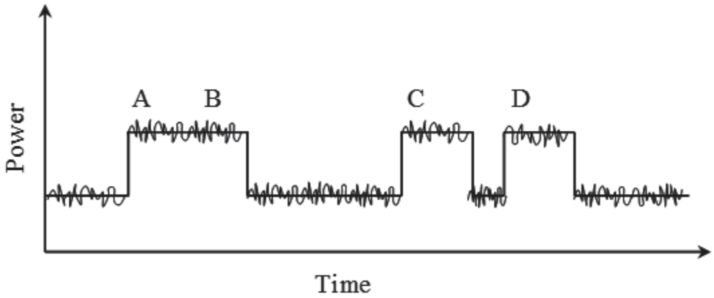

Figure II.5: Range resolution: pulses. The equivalent of Figure II.4 in terms of pulses received by the radar.

modulation can be used to synthesize an effectively short pulse. This process of generating a narrow synthetic pulsewidth is called pulse compression. The approach is to introduce a modulation on the transmitted pulse, and then pass the received signal through a filter matched to the transmit signal modulation [19]. The most common transmit waveform used for pulse compression is linear FM (or chirp), and the ground range resolution equation becomes:

$$R_G = \frac{c}{2Bsin(\theta)} \tag{II.2}$$

where B is the bandwidth of the chirp pulse.

The ground range resolution is a function of the bandwidth of the transmitted pulse and look angle but **independent of height**. Using pulse compression, a SLAR system can achieve a very high range resolution, but the cross-range resolution of the SLAR is limited by the physical beamwidth of the antenna.

Azimuth resolution

Azimuth resolution is the minimum distance on the ground in the direction parallel to the flight path of the instrument platform at which two targets can be separately imaged. Two targets located at same slant range can be resolved only if they are not in the radar beam at the same time. Figure II.6 shows the angular spread of the radar beam in the azimuth direction is equal to

$$\beta = \frac{\lambda}{L} \tag{II.3}$$

Thus, the azimuth resolution can be written as,

$$R_A = \frac{R\lambda}{L} \tag{II.4}$$

where R is the distance antenna-object (refer to the Figure II.2).

It can be seen that a large antenna length and small wavelength will give a better resolution, but that the resolution deteriorates with range from the satellite. Figure II.6 shows the azimuth resolution deteriorating as slant range increases. As an example, the SEASAT antenna at an altitude of 800 km would attain a SLAR resolution of 18 km with an antenna size of 10 m [20]. This apparent limitation is overcome by SAR systems (see Section II.5).

II.4.3 Geometrical distortions

SLAR images have three main geometrical distortions associated with the side looking aperture. The points A, B and C are imaged as A', B' and C' in the slant range plane (see Figure II.7). This shows how minor differences in elevation can cause considerable range distortions. These relief induced effects are called Foreshortening, Layover and Shadow.

Foreshortening is the name given to the phenomenon shown in Figure II.7. This occurs when the radar beam reaches the base of a tall feature tilted towards the radar before it reaches the top. Because the radar measures distance in slant-range, the slope (from point B to point C) will appear compressed and the length of the slope will be represented incorrectly (B' to C') at the image plane.

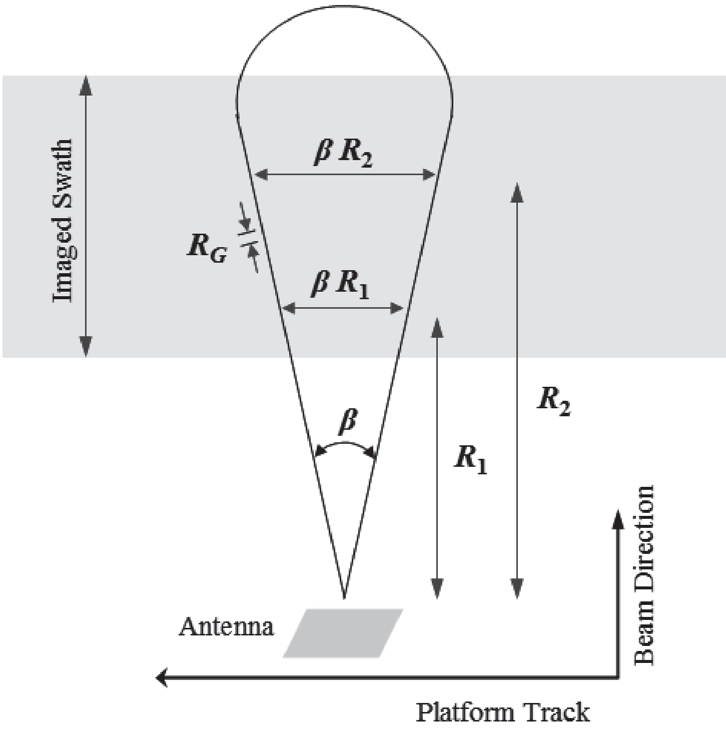

Figure II.6: Azimuth resolution of SLAR.

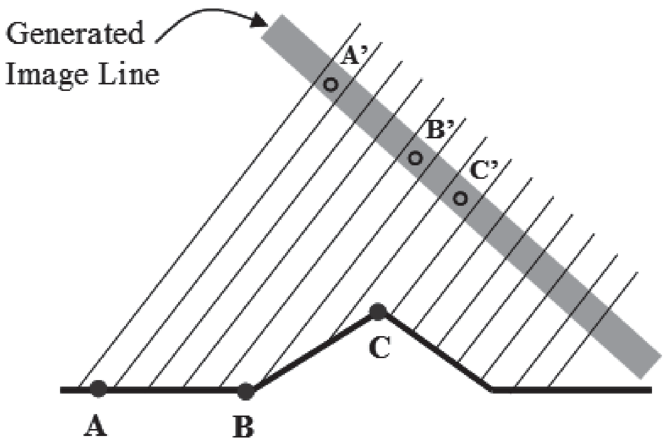

Figure II.7: Foreshortening: length BC appears much shorter in slant range than in ground range.

Figure II.8 describes Layover, which occurs when the terrain slope is much greater than the incidence angle [20]. In the image, it would appear that the top of the slope is 'laying over' the bottom. Finally, shadow is shown in Figure II.9. This is caused by objects, which cover part of the terrain behind them. The shadowing effect increases with

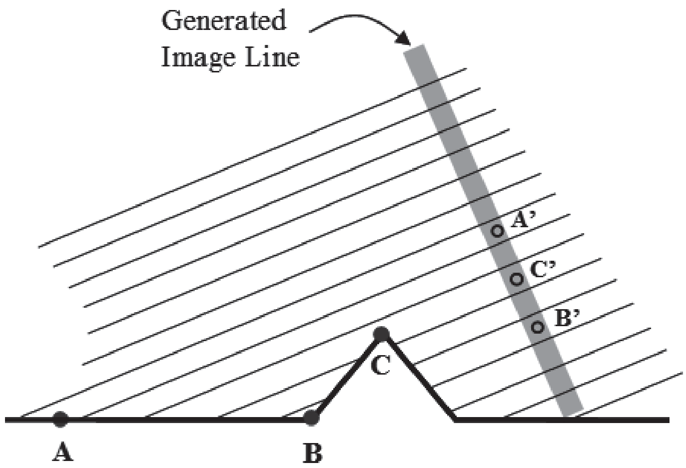

Figure II.8: Layover: point C appears before point B in slant range.

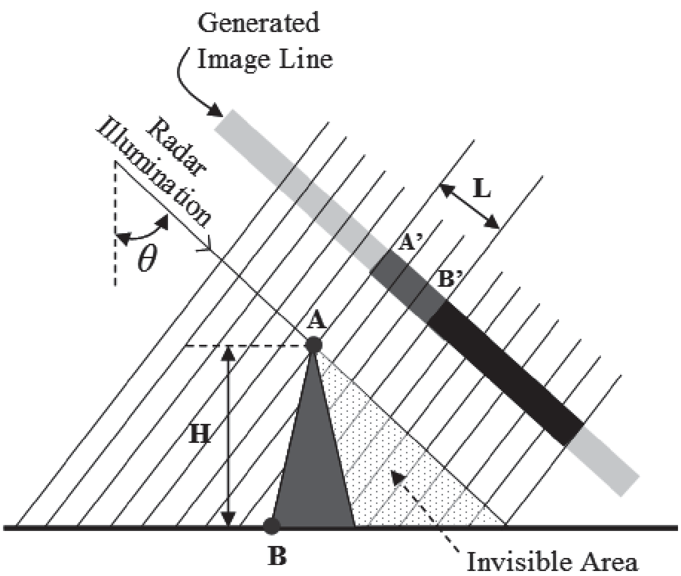

Figure II.9: Shadow: terrain blocks radar signal.

the incident angle θ and the invisible area will appear in black in the image.

II.5 Synthetic Aperture Radar

Synthetic Aperture Radar (SAR) systems are a special case of SLAR that overcomes the problems of poor azimuth resolution by some further signal processing algorithms. The SAR principle is shown in Figure II.10. The target is in each of the pulse returns represented in the figure and thus contributes to each of these pulses by returning an echo composed of an amplitude and phase. The phase of each pulse will be offset mainly caused by the path propagation delay, in addition to the dielectric and geometric properties of the target. One simple solution is to modify the phase of the samples to which the target has contributed, so that they all have the same phase. The coherent summation of these returns leads to a significant improvement of the Signal to Noise Ratio (SNR) related to the target. From this processing a large antenna length is synthesized which is characterized by a much more narrow beam, as shown in Figure II.10.
The target may be illuminated by the SAR during the azimuthal distance $L_{synth} = 2R\lambda/L$. According to equation II.4, the new azimuth resolution for the SAR process is given by [20]

$$R_A = \frac{R\lambda}{L_{synth}} = \frac{R\lambda}{\frac{2R\lambda}{L}} = \frac{L}{2} \tag{II.5}$$

where L is the real SAR antenna length, which seems counter-intuitive that a smaller antenna should lead to a better resolution. This can be partly explained by the fact that a smaller antenna size will lead to a larger beam-width, meaning a target will be in more returns and hence a larger aperture can be synthesized.

II.5.1 SAR signal processing and image formation

Like most of the electromagnetic signals, a radar echo carries an amplitude and a phase simultaneously. Thus the data are complex numbers, an indispensable feature for SAR focusing. During the scanning of a scene, the SAR collected data are arranged in a two dimensional array (range direction and azimuth direction) to form the raw data. In a SAR signal processor there are specific operations required to convert a raw data set into an interpretable image. The raw SAR data are not forming a useful image since point targets are spread out in range and in azimuth directions [20]. The main goal of SAR data processing, also known as focusing process, is the determination of the range and azimuth coordinates of the targets. The most common algorithm employed in the SAR processing system is the Range Doppler Processing (RDP) algorithm, which is a two-dimensional correlating procedure as shown in Figure II.11 [20]. The two dimensions of

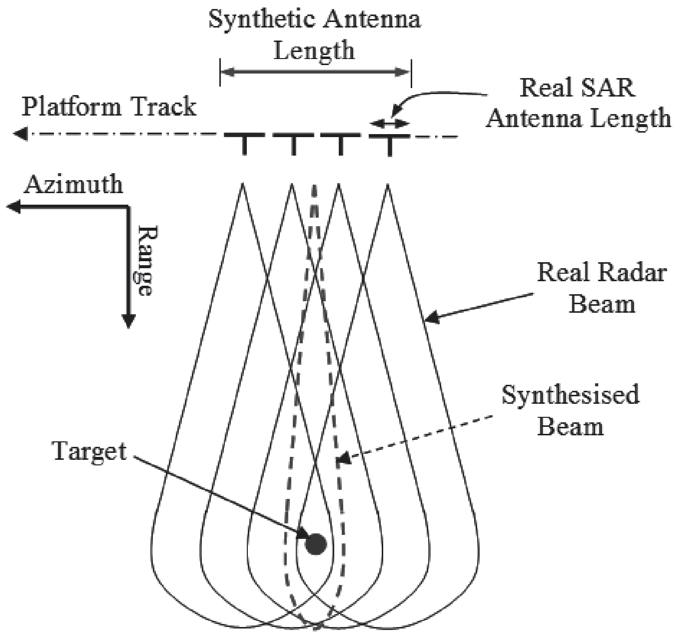

Figure II.10: Synthetic Aperture principle. The target is in many radar returns, from a real antenna length L, moving along track. Processing can synthesize a large antenna length L_{synth} characterized by a fine beam.

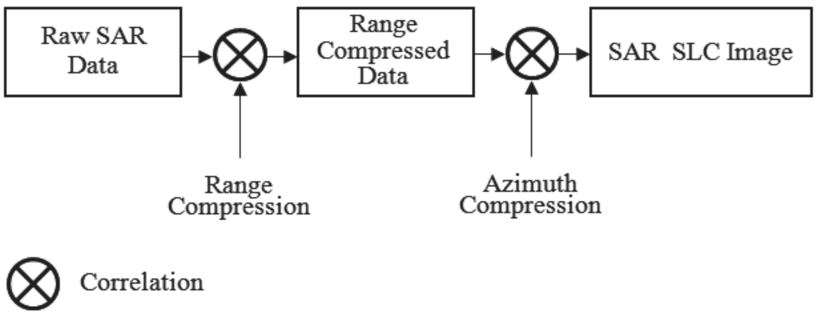

Figure II.11: Range-doppler processing.

the correlation processing are realised as two one-dimensional matched filter operations namely range compression and azimuth compression. The first matched filtering operates on the single pulse radar returns (pulse compression) and the second matched filtering on the Doppler signal. After the raw data focusing step, the obtained SAR image is called a Single Look Complex (SLC) image.

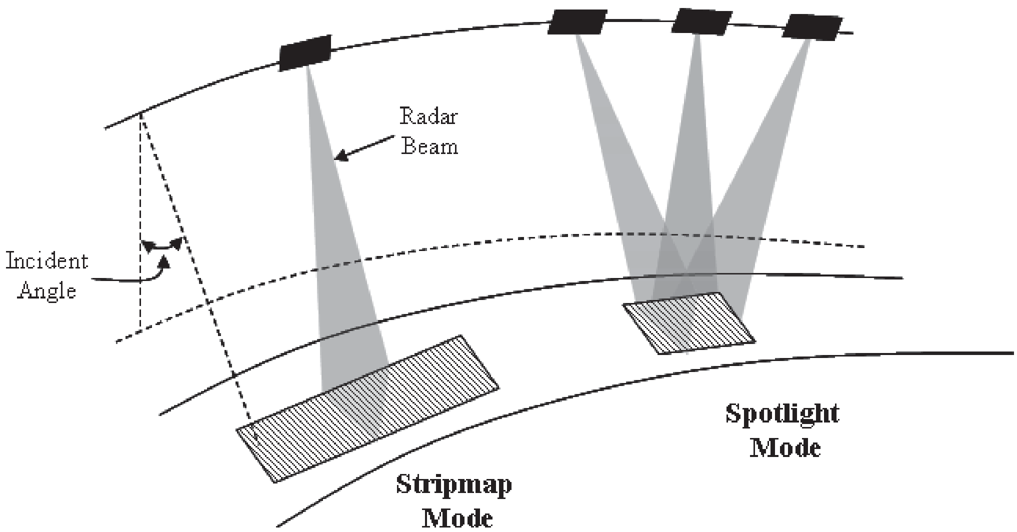

Figure II.12: SAR scanning modes.

II.5.2 SAR data acquisition modes

Two common modes of gathering SAR data are stripmap SAR and spotlight SAR, as shown in Figure II.12. The stripmap SAR is one of the most dominant operating modes of SAR remote sensing. In this mode, the beam remains in a constant pointing direction as the platform moves. As a result, a strip of the earth's surface parallel to the flight path is continuously illuminated. In the same way, the scan SAR mode can provide a large area coverage by scanning several adjacent ground sub-swaths with simultaneous beams, each with a different incidence angle [23]. Due to the reduced azimuth bandwidth the azimuth resolution of a scan SAR product is lower than in stripmap mode. With the spotlight mode, the antenna beam will be steered so that the scene will be illuminated over a large aspect angle and hence the synthetic aperture becomes larger [23]. Spotlight mode provides the highest geometrical resolution, therefore the size of the ground observed area is smaller than the one in the other modes.

II.5.3 SAR image interpretation

Radar images have certain characteristics that are fundamentally different from images obtained by using optical sensors. As said before, the radar data contain amplitude and phase information. The amplitude of the SAR image records reflectivity, the variable ability of the terrain to send the incident energy back to the radar. If the backscattered signal of a particular resolution cell is high then the image pixel will be bright. Otherwise,

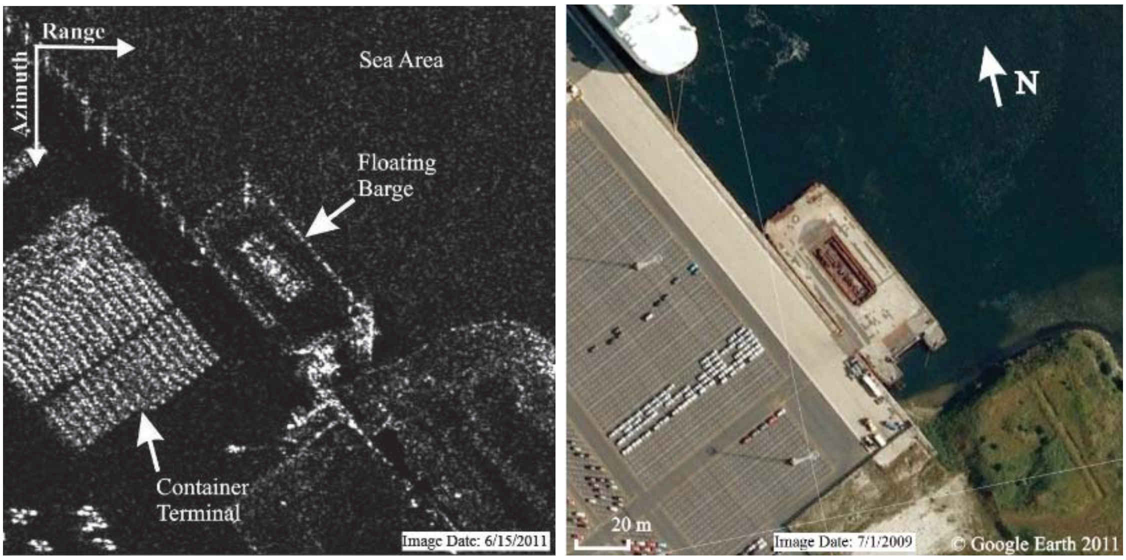

(a) (b)

Figure II.13: Part of the Zeebrugge harbour (Belgium) imaged with SAR and optical sensors. (a) CSK SAR intensity image acquired in spotlight mode (sub-set size of 200 × 200 pixels). (b) Optical image from Google Earth™ of the site of interest. COSMO-SkyMed™ Product - ASI [2011] processed under license from ASI - Agenzia Spaziale Italiana. All rights reserved.

for low backscattering values the pixels will be dark. There are various parameters that affect the amount of backscatters received by the radar: wavelength of the transmitted pulse, polarization, incidence angle, surface roughness and soil moisture content. Smooth surfaces (like roads or water) act as specular reflectors, which do not reflect much of the signal back to the radar and appear black in the image. A rough surface acts as a diffuse reflector and will reflect more of the signal back to the radar. The amplitude of the SAR image is visualized by means of grey-scale levels as is shown in the example of Figure II.13. The bright pixels correspond mostly to corner reflections, double bounces and surfaces orientated within the container terminal area, whereas dark pixels correspond to the sea area and to the ground surface along the port edge. In addition to amplitude information, a radar echo carries phase information which results from superposition of several effects related to the propagation and the backscattering of the electromagnetic wave. Therefore, the phase information appears as a noisy image with values uniformly distributed between 0 and 2π. The phases become meaningful only when some of these effects are isolated by comparing radar images.

II.5.4 Speckle in SAR images

The presence of several scatterers within each SAR resolution cell generates the so-called 'speckle' effect that is common to all coherent imaging systems. Homogeneous areas, see Figure II.13, that extend across many resolution cells are imaged with different amplitudes. The speckle effect is a direct consequence of the superposition of the signals reflected by many small elementary scatterers (those with a dimension comparable to the radar wavelength) within the resolution cell [24]. These signals, which have random phase because of multiple reflections between scatterers, add to the directly reflected radiation. Intuitively, the resulting amplitude will depend on the imbalance between signals with positive and negative sign. Speckle in SAR images complicates the image interpretation and image analysis. However, the speckle effect can be reduced by taking multiple looks (summation of several adjacent pixels to obtain single pixel) or by using some specialized filters [3].

II.5.5 Important SAR data parameters

The basic characteristics of SAR data are substantially related to the following three frequencies, described here from the highest to the lowest:

1. The radar's carrier frequency f_c is the frequency of the instrument's oscillator. This frequency defines the radar's wavelength λ by: $\lambda = c/f_c$, where c is the speed of light. Typical pulse carrier wavelengths used are approximately 3 cm (X-band), 6 cm (C-band), 9 cm and 24 cm (L-band). In addition to the polarization, the wavelength is the most important parameter that determines the penetration of the wave into a medium. Generally, the longer the wavelength, the stronger the penetration into the target is. The data available today for the scientific researchers are mostly those of the civilian satellites that work in one of the following microwave bands:

    - C band - 5.3 GHz (the European ERS and Envisat, the Canadian Radarsat, and the US shuttle missions).
    - L band - 1.2 GHz (the Japanese J-ERS and ALOS).
    - X band - 10 GHz (the German TerraSAR-X and the Italian COSMO-SkyMed).

2. The sampling frequency in range f_r defines the size of the range pixel R_S by $R_S = c/2f_r$ where the factor 2 takes into account of the fact that the difference between two

pixels includes the round trip. A correct sampling of the echo requires a sampling frequency f_r larger than the pulse modulation bandwidth B_s which controls the range resolution of the instrument, in order to satisfy Shannon's sampling conditions. Typical used bandwidth B values are in the range of 10-400 MHz.

3. The pulse repetition frequency (PRF) defines the size of the azimuth pixel R_A by $R_A = v/PRF$, where v is the modulus of the instrument platform velocity, here assumed to be constant and linear. The relationship is more complicated when the velocity of the instrument platform has a non-zero curvature, case of satellite mounted radar. Typical used PRF values are in the range of 1-10 kHz.

The polarization of the transmitted and received wave is another parameter that has great influence on the radar signature of complex scatterers. The use of a fully polarimetric SAR allows for the separation of different scattering mechanisms, e.g. surface, volume. The combination of polarimetry and interferometry enables the coherence optimization [25].
The incidence angle θ determines the radar response of a scatterer. For a given altitude of the sensor, the swath increases with the incidence angle and the SNR reduces. From an interferometric point of view θ should be chosen such as to balance the probability for layover and shadow and to move the 'blind angle' region towards less critical terrain slopes.
The CSK SAR images, that represent the most important part of the SAR data used during the preparation of this thesis was acquired in spot light mode, horizontally polarized with the following parameters: f_c = 9.6 GHz (X-band), PRF = 9883 Hz and B_s = 380 MHz, which allows a pixel size of R_A = 70 cm in azimuth and R_S = 31 cm in range. The incidence angle of θ =26°, leads to a ground range resolution of R_G = 71 cm.

II.6 Summary

An introduction to radar for remote sensing has been given. The geometry and the terminology of remote sensing radar have been described for side-looking systems. An emphasis is given to the SAR which is an all-weather imaging tool that achieves fine azimuth resolution by taking the advantage of radar motion to synthesize a large antenna aperture. It has been shown that both range and azimuth resolution of the SAR image are independent of height, which makes the SAR systems ideal for use in military and scientific applications such as border security and environmental monitoring. The SAR image formation has been given, together with the SAR data acquisition modes. The radar image interpretation and the speckle effect in SAR data have been discussed. The basic parameters of the SAR data are summarized.

CHAPTER III

SAR INTERFEROMETRY

III.1 Introduction

SAR Interferometry (InSAR) is a technique that exploits the phase differences of at least two SAR images acquired from different orbit positions and/or at different times [2]. In other words, the phase difference (known also as the interferogram) of the SAR images is formed. The derived interferogram information can be used to measure several geophysical quantities, such as topography, surface deformations, glacier flows, vegetation properties, etc... [26]. The basic principle of using InSAR techniques for Earth observation dates to years 1970s [27]. However, in view of terrestrial applications it was only in the 1980s that the first results were published [28]. As far as space-borne InSAR is concerned, in the beginning only few well-selected SAR data sets of the SEASAT mission were available. An enormous amount of SAR data sets suitable for interferometry became available after the launch of the ESA satellite ERS-1 in 1991. In 1995 ESA launched a second SAR capable satellite, ERS-2, with the same instrument characteristics as ERS-1. ERS-2 was put into an orbit 24 hours behind ERS-1, allowing interferometry to be performed with a short temporal baseline, or separation, between image observations. Interferograms made up of two images separated by this 1 day baseline are called Tandem pairs.

Today it is generally accepted that SAR interferometry is an extremely powerful tool for mapping the Earth's land, i.e. generation of Digital Elevation Model (DEM). The so-called differential InSAR represents a unique method for detection and mapping of surface displacements over large temporal and spatial scales with a precision in the cm and even mm range [26]. As previously stated, the main uses of interferometry concern topographic mapping and land classification. A CCD map, based on the use of InSAR coherence, can provide a very sensitive indicator of activity in an observed area between the two SAR passes [2]. Recently, with the advent of satellite constellations delivering high-resolution SAR images such as CSK and TSX, it makes it possible to detect surface changes with fine spatial details and with a short temporal baseline. These advantages confers to InSAR coherence to be suitable for use in military and scientific applications such as border security and environmental monitoring.

This chapter reviews the technology and the signal theoretical aspects of InSAR process. Emphasis is given to the SAR interferogram formation. Coherence is shown to be a measurement of interferogram quality. Focus is then given on the application of coherence to ground change detection, together with several results obtained by real SAR data.

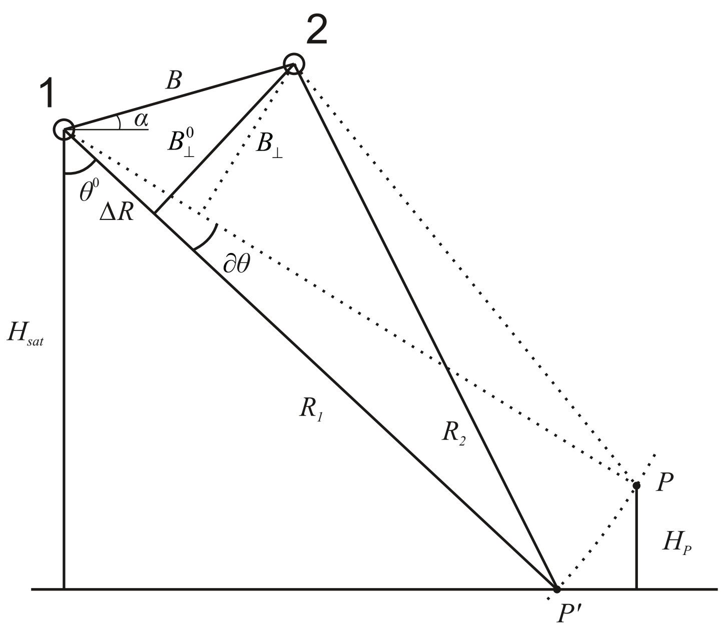

Figure III.1: Interferometric configuration. Satellite positions 1 and 2 have ranges, to target P, R_1 and R_2 respectively. The separation between the satellites is called the spatial baseline and is denoted by B.

III.2 Interferometric configuration

In Repeat-pass interferometry the SAR system fly on (ideally) parallel tracks and view the terrain from slightly different directions at different times. Figure III.1 shows a typical spaceborne InSAR configuration. "1" and "2" denote the satellite positions when the first and second SAR images were taken. The distance between them is called the (geometric) baseline and is denoted as B in Figure III.1. The perpendicular baseline, $B_\perp$, is the component of B in the direction perpendicular to the look direction. R_1 and R_2 denote the ranges to the target P from satellite positions "1" and "2" respectively. The principle of the SAR Interferometry technique is the use of the phase information of every pixel to measure the parallaxes $\Delta R = R_2 - R_1$. Let

$$s_1(R,\ x) = |s_1(R,\ x)|\ \exp\{j\phi_1(R,\ x)\}\ \text{ and }\ s_2(R,\ x) = |s_2(R,\ x)|\ \exp\{j\phi_2(R,\ x)\} \tag{III.1}$$

be the two SAR images forming the interferogram

$$I(\cdot) = s_1(\cdot)s_2^*(\cdot) \tag{III.2}$$

where the phase of the interferogram $I(\cdot)$

$$\phi(\cdot) = \phi_1(\cdot) - \phi_2(\cdot) \tag{III.3}$$

is the interferometric phase.
The phase of the SAR image response of a point scatterer is proportional to range plus a possible shift due to the scatterer itself [27], i.e.

$$\phi_1 = -\frac{4\pi}{\lambda} R_1 + \phi_{\text{scat, } 1} \tag{III.4}$$

$$\phi_2 = -\frac{4\pi}{\lambda} R_2 + \phi_{\text{scat, } 2} \tag{III.5}$$

Assuming that the scattering phase is the same in both images ($\phi_{\text{scat, } 1} = \phi_{\text{scat, } 2}$), the interferogram phase measures the range difference:

$$\phi = 4\pi/\lambda \; \Delta R \tag{III.6}$$

of course, ϕ is still ambiguous to within integer multiples of 2π. In literature, this is addressed as phase unwrapping problem [26].
ΔR can be written as the projection of the baseline B on the first antenna line of sight:

$$\Delta R = B \sin(\theta - \alpha) \tag{III.7}$$

Now, let see how a topographic height change causes a proportional change in the interferometric phase. Consider point $P^{'}$ with a different height H_p with respect to point P. The interferogram related to the point $P^{'}$ is given by:

$$\phi^{'} = 4\pi/\lambda \; B \sin(\theta + \Delta\theta - \alpha) \tag{III.8}$$

The change in height H_p is reflected in the difference of the interferometric phases $\phi_p = \phi - \phi^{'}$. Using a small angle approximation, we obtain [29]:

$$\phi_p = -\frac{4\pi}{\lambda}\left(\frac{B_{\perp,p}}{R \sin\theta} H_p - B \sin(\theta_p - \alpha)\right) \tag{III.9}$$

This provides the relation between the measured phase ϕ_p and the height H_p. The second term in Equation III.9 is called phase of flat area ($H_p = 0$), which causes orbital fringe in the interferogram (see Section III.3.3).
The altitude of ambiguity of the interferometer is defined as [26]

$$z_{2\pi} = \frac{\lambda}{2} \frac{R \sin\theta}{B_\perp} \tag{III.10}$$

$z_{2\pi}$ represents the altitude difference that generates an interferometric phase change of one fringe (2π). It can be seen that the altitude of ambiguity is inversely proportional to the perpendicular baseline $B_{\perp}$. Indeed, for large values of $B_{\perp}$, the interferogram will be characterized by high density of fringes which complicate the phase unwrapping step. For small values of $B_{\perp}$, the fringes become too much broad, inducing the loss of topographic details.

III.3 SAR interferometric process

Recall that the interferogram is the interference pattern between two SAR images. The interferometric processing chain can be split up into several different stages. The processing chain, starting from SLC data is outlined below. SLC data is the raw SAR data which has already been focused (see Chapter II). The main steps in generating the interferogram summarized below are highlighted afterwards.

1. Co-register the two SAR images;
    - Coarse co-registration (pixel to pixel)
    - Fine co-registration (sub-pixel to sub-pixel)
2. Create the complex interferogram.
3. Flatten the interferogram.
4. Filter the interferogram.
5. Generate a coherence image (see Section III.4).
6. Unwrap the phase and generate the DEM.

The phase unwrapping step is not of interest in the CCD application, so it will not be discussed in this thesis. Hanssen R. [29] made an exhaustive study about forming interferogram, steps and applications. A description of the above steps follows.

III.3.1 SAR images co-registration

The co-registration, which is the first stage of the processing chain, must be addressed since for interferometry it is fundamental that the two images are registered to sub-pixel accuracy [29] as described below. Due to the repeat-pass geometry they will almost

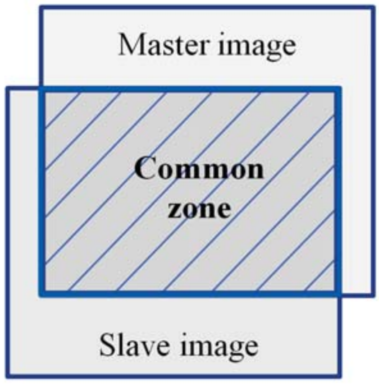

Figure III.2: SAR images co-registration.

certainly have some small shift and rotation between the two SAR acquisitions. One of these two SAR images must be assigned as the master (reference) image and the other one is the slave (match) image. Through the whole co-registration process, only the slave image will be modified (shifted and re-sampled). The co-registration is usually split up into two stages; coarse and fine co-registration:

1. Coarse co-registration: This is performed either using the orbit information [29] or by calculating the correlation between the magnitudes of the two images at various points. Using either of these techniques can give the offsets between master and slave images, as indicated in Figure III.2, with co-registration error of one pixel.

2. Fine co-registration: The whole slave image is up-sampled by 1/10 and the cross-correlation (i.e. coherence, see Section III.4) is calculated for a set of windows over the two images, which yields an offset vector for that window. Then these offset vectors can be used to determine a polynomial equation to calculate the offsets for every pixel in the slave image [28].

Bamler and Hartelet [26] show that an accuracy of $1/8^{\text{th}}$ of a pixel in SAR co-registration is sufficient for interferometry, since it yields a negligible 4% decrease in the coherence. Co-registration for SAR interferometry is well discussed by Gabriel and Goldstein in [28]. In this thesis the co-registration of the SAR images was performed with the Sarscape$^{\text{TM}}$ software.

III.3.2 Interferogram formation

The interferogram can now be formed using the master and the co-registered slave images. Because the SAR images are complex the interferogram can be formed by multiplying one

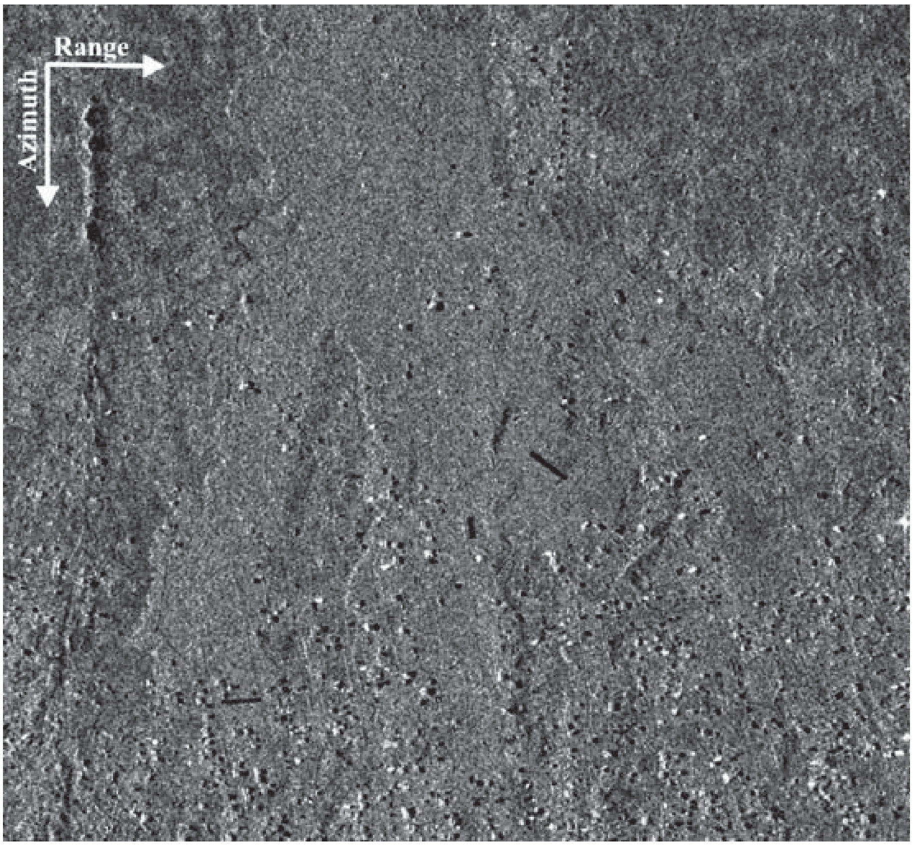

Figure III.3: CSK intensity image of a flat area in Goma (R. D. of Congo). Sub-set size of 1400 × 1400 pixels, acquired in spotlight mode. COSMO-SkyMed^{TM} Product - ASI [2011] processed under license from ASI - Agenzia Spaziale Italiana. All rights reserved.

SAR image with the conjugate of the other (see Equation III.2). In InSAR applications, we are generally interested only by the phase information and the term interferogram is used to describe the phase interferogram. To decrease the noise in the interferogram, Gabriel and Goldstein [28] propose a multilook approach, in which the complex interferogram data in a specified window are simply averaged. Multilooking can be performed simultaneously with the complex multiplication, and is often applied to a range-azimuth ratio that yields approximately square pixels, such as 1 : 4, 1 : 5, etc.

Figures III.3 and III.4 show a SAR image together with the interferogram of the same agricultural area in Goma, Democratic Republic of the Congo (DRC). It is a rather flat plain with few houses. In the SAR intensity image, the small hills (top left of Figure III.3) exhibit the geometric distortions discussed earlier. On the lower part of the image, the shadow is clearly visible beside the different houses. It is important to note that the two SAR images used appear identical to the eye, since the acquisition period is of only 4 days. The interferometric phase in Figure III.4 is coded in color. The iso-phase contours

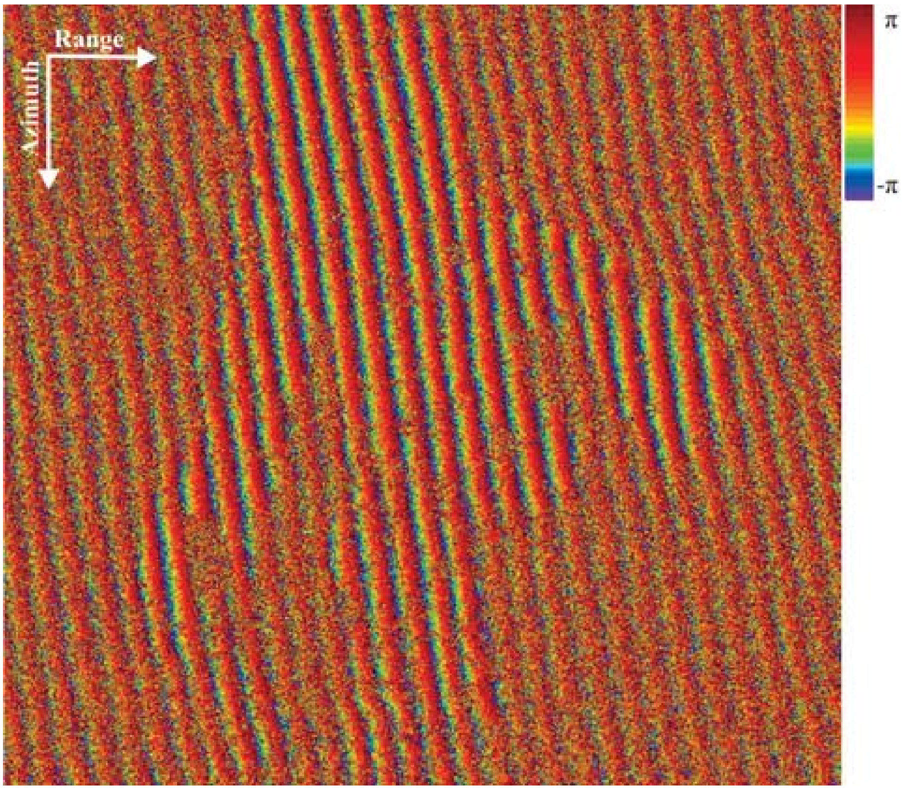

Figure III.4: SAR interferogram of the area shown in Figure III.3. Baseline: $B_{\perp} = 307$ m $\rightarrow z_{2\pi} = 15$ m. The time delay between the two acquisitions is 4 days.

form a pattern that is usually referred to as *fringe* pattern.

III.3.3 Interferogram flattening

As shown in Equation III.9, the interferometric phase is made from two kinds of fringe. The first one is the topographic fringe generated by terrain height variations. The second term, namely orbital fringe, consists of a dominant frequency in the range direction which is due to the ellipsoidal shape of the earth (see Figure III.4). Flattening is the process to eliminate the orbital fringe, it is also called orbital fringe correction. In recent years, some flattening approaches for InSAR have been proposed and can be categorized into two classes:

1. Orbit-equation algorithm: It is based on the orbit Ephemerids and computes the flat-Earth phase by solving a set of equations (Doppler, range, and ellipsoid) [30].
2. Fringe-frequency algorithm: It is based on the interferogram itself and carries out flattening by measuring the maximum fringe frequency where the flat-Earth phase

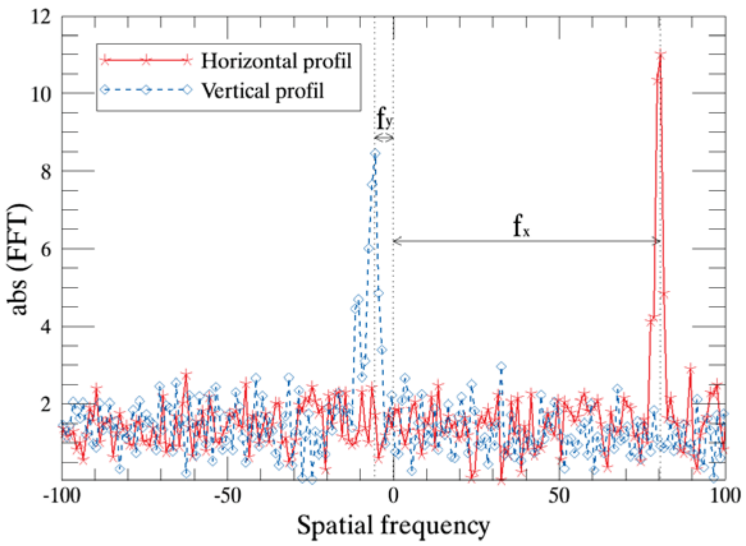

(a)

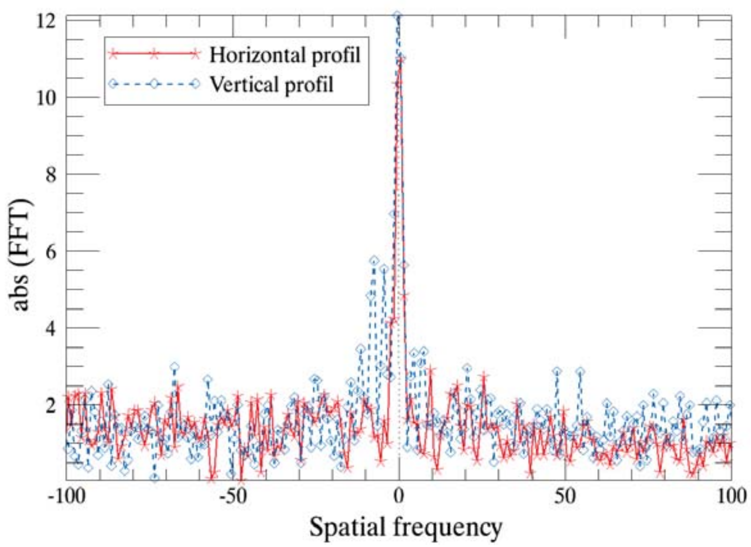

(b)

Figure III.5: Interferograms spectrum. (a) Original interferogram, (b) Flattened interferogram.

dominates [31]. For that, the fast Fourier transform may be computed along the range and azimuth directions.

Figure III.5 shows interferogram spectrum before and after the flattening operation. Once the two frequency shifts (f_x and f_y) are estimated from Figure III.5(a), the flat-Earth phase $e^{j\phi_0(i,j)} = e^{j2\pi(f_x i + f_y j)}$ is subtracted causing the shift of the interferogram spectrum

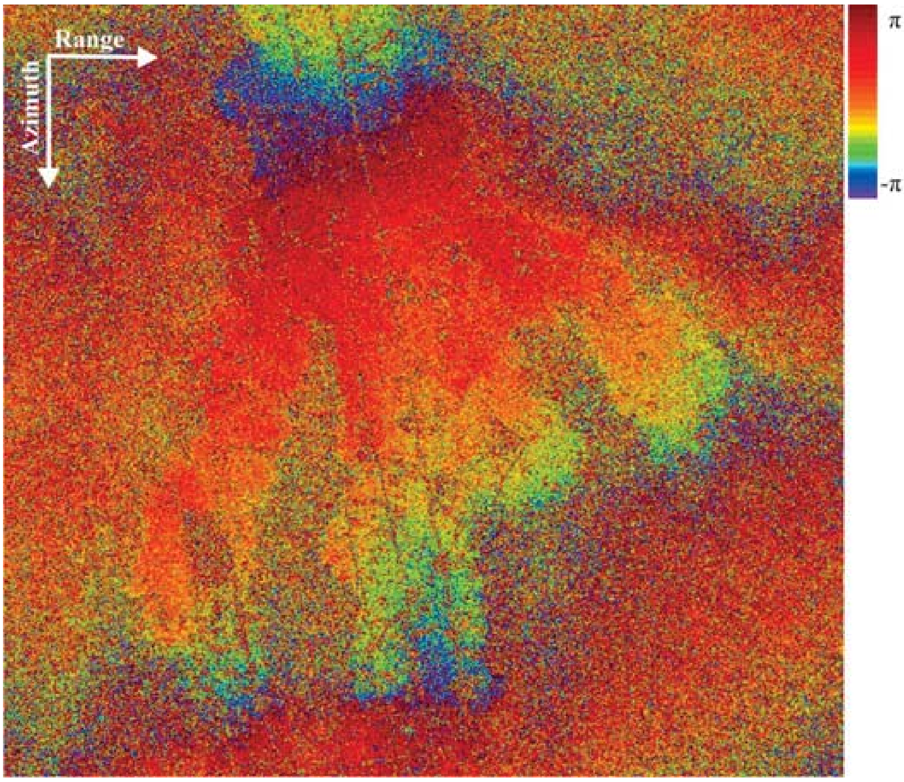

Figure III.6: Flattened interferogram of Figure III.4 using the fringe-frequency algorithm.

peak to the zero frequency, as indicated in Figure III.5(b).
The flattened example from Figure III.4 is shown in Figure III.6. The resulting flattened interferogram shows fringes which relate only to the topography variation.

III.3.4 Interferogram filtering

Throughout the interferometric process, the operation of filtering takes place at two levels. A priori filtering is applied to the original SAR data, before interferogram generation and a posteriori filtering is applied after the interferogram has been formed. Many a posteriori filters have been proposed to enhance the quality of the interferogram. The most commonly used filter is the boxcar filter applied in the complex phase plane. Other filters, such as the median filter [32] and the two dimensional (2-D) Gaussian filter [33], have also been applied. All these filters do not adapt to local noise level variations.

Goldstein filter

Goldstein and Werner [6] proposed an adaptive interferogram filter given by

$$H(u,v) = S\{Z(u,v)\}^{\beta} \times Z(u,v) \tag{III.11}$$

where $H(u,v)$ is the spectrum of the filtered interferogram, $Z(u,v)$ is the Fourier transform of a small interferogram patch, $S\{\cdot\}$ is a smoothing operator and (u,v) are spatial frequencies. The filter parameter β is an arbitrarily chosen value between zero and one and has the biggest impact on the filter performance. For β=0, no filtering occurs. However, for β=1, the filtering is significant but at the expense of the topographic details preservation.
In [34], the filter is modified by making the parameter β dependent on the coherence γ as follow

$$\beta = 1 - \overline{\gamma} \tag{III.12}$$

The parameter $\overline{\gamma}$ is the mean value of the absolute coherence computed over the corresponding patch on the coherence map (see Equation III.25).
This modification adapts the filter to the interferogram more effectively by preventing the areas characterized by high coherence being overfiltered. On the other hand, it allows stronger filtering on the areas with low coherence. An example of an interferogram filtered using Goldstein filter is shown in Figure III.7. It can be seen that the effect of the phase noise is highly reduced using this method.

Subspace projection based filtering

Recently, numerous studies have focused on SAR interferometric phase filtering via subspace projection [35]-[36]. In addition to the phase noise reduction benefits, subspace projection based methods present the advantage of being robust in the presence of coregistration errors. In [35], a joint subspace projection method has been proposed to estimate the InSAR interferometric phase in the presence of large coregistration errors. In [37], the generalized correlation steering vector is used to auto-coregister SAR images as well as to reduce the interferometric phase noise. Subspace projection based methods use the projection of the signal subspace onto the corresponding noise subspace, which is obtained from the eigen-decomposition of the covariance matrix, to estimate the optimal interferometric phase value [35]-[36].
Assuming that the two SAR images are coregistered and the interferometric phase is flattened, the complex data vector $s(i)$ of a pixel pair i of the two SAR images can be formulated as follows [37]

$$s(i) = [s_1(i), s_2(i)]^T = \mathbf{a}(\varphi_i) \odot \mathbf{x}(i) + n(i) \tag{III.13}$$

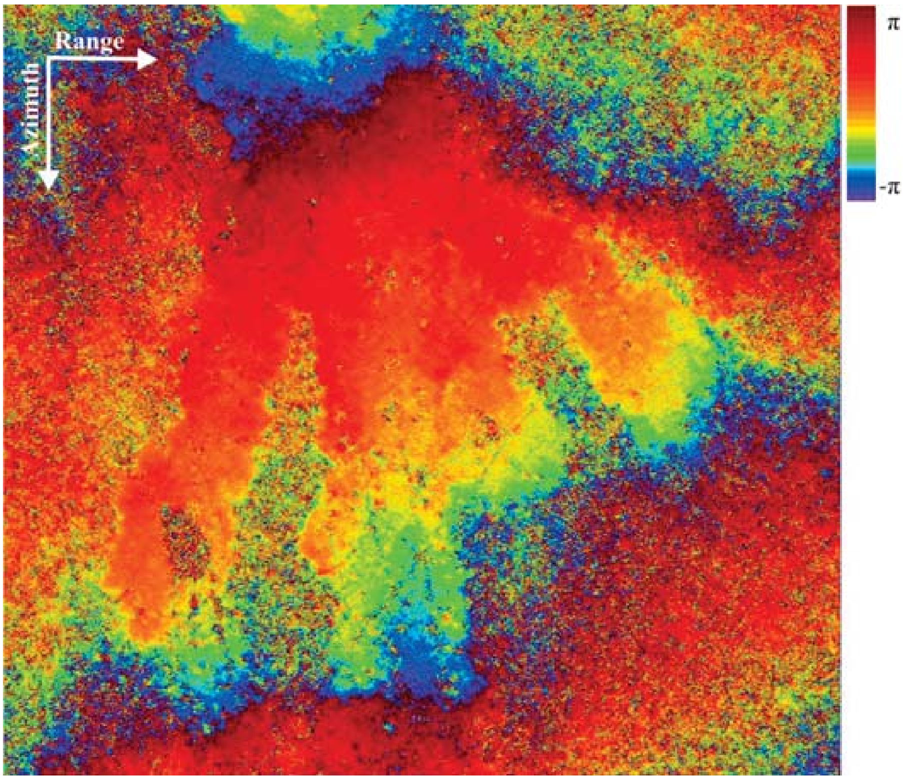

Figure III.7: Result of Goldstein filter: same interferogram as Figure III.6. Baseline: $B_\perp = 307$ m $\rightarrow z_{2\pi} = 15$ m. The time delay between the two acquisitions is 4 days. COSMO-SkyMed^{TM} Product - ASI [2011] processed under license from ASI - Agenzia Spaziale Italiana. All rights reserved.

where $\mathbf{a}(\varphi_i) = [1, e^{j\varphi_i}]^T$ is the steering vector of pixel i, superscript T denotes the vector transpose operation, φ_i is the terrain interferometric phase to be estimated, $\odot$ denotes the Hadamard product, $\mathbf{x} = [x_1(i), x_2(i)]^T$ is the complex magnitude vector of the scene reflectivity received by the satellites, and $n(i)$ is the additive noise term.
The complex data vector $s(i)$ can be modeled as a joint complex circular Gaussian random vector with zero-mean and the corresponding covariance matrix $C_s(i)$ is given by

$$C_s(i) = E\{s(i)s^H(i)\} = \mathbf{a}(\varphi_i)\mathbf{a}^H(\varphi_i) \odot E\{\mathbf{x}(i)\mathbf{x}^H(i)\} + \sigma_n^2\mathbf{I} \qquad \text{(III.14)}$$

$E\{\}$ denotes the statistical expectation, superscript H denotes vector conjugate transpose, $\sigma_n^2(i)$ is the noise power, and $\mathbf{I}$ is 2×2 identity matrix. $R_s(i) = E\{\mathbf{x}(i)\mathbf{x}^H(i)\}$ is called the correlation matrix. Normally, when the SAR images are accurately coregistered, the number of the principal eigenvalues of the covariance matrix $C_s(i)$ is one. In this situation, the dimensions of the signal subspace and the noise subspace are both one.

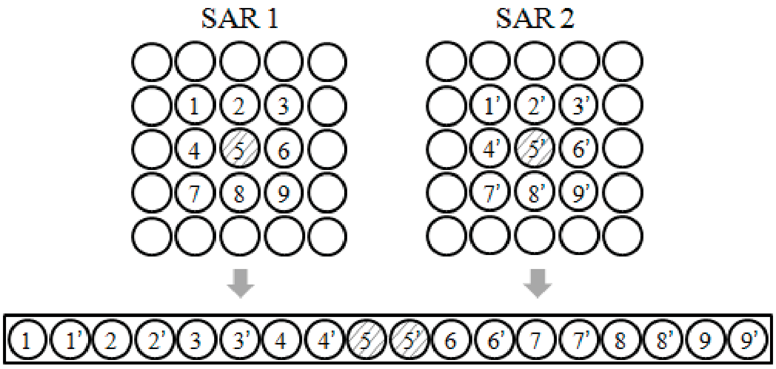

Figure III.8: Formulation of joint spatial steering vector using a 3×3 pixel pair window.

The eigen-decomposition of the covariance matrix $C_s(i)$ follows:

$$C_s(i) = (\lambda_s + \sigma_n^2)(\mathbf{a}(\varphi_i) \odot \beta_s)(\mathbf{a}(\varphi_i) \odot \beta_s)^H + \sigma_n^2 \beta_n \beta_n^H \tag{III.15}$$

where λ_s and β_s are the principal eigenvalue and the corresponding eigenvector of $R_s(i)$ respectively and β_n is the noise eigenvector corresponding to the insignificant eigenvalue of $C_s(i)$. The eigenvectors β_s and β_n span two orthogonal subspaces, namely the signal plus noise subspace and the noise only subspace. From III.15, the steering vector $\mathbf{a}(\varphi_i)$ corresponding to the interferometric phase is orthogonal to the noise subspace β_n, which is the key idea of the MUSIC (MUltiple Signal Classification) method [38]. In this method, the optimum estimate of the interferometric phase may be obtained by searching the value of φ which maximizes the pseudospectrum (i.e. cost function) given by

$$J_1 = 1/\mathbf{a}^H(\varphi)\beta_n\beta_n^H\mathbf{a}(\varphi) \tag{III.16}$$

In practice, Formulation III.13 is insufficient. It causes a misestimate of the noise subspace β_n. For that reason the specified pixel pair and its neighboring pixel pairs are used to jointly perform the interferometric phase estimation . An example to formulate the joint data vector $j_s(i)$ is shown in Figure III.8 [37], where circles represent SAR image pixels and (i) denotes the centric pixel pair whose interferometric phase is to be estimated.

As shown in Figure III.8, the joint data vector $j_s(i)$ can be written:

$$j_s(i) = [s(i-4)^T, s(i-3)^T, \ldots, s(i)^T, \ldots, s(i+4)^T]^T \tag{III.17}$$

The corresponding joint covariance matrix is given by

$$C_{js}(i) = E\{j_s(i)j_s^H(i)\} = \alpha(\varphi)\alpha^H(\varphi) \odot R_{js}(i) + \sigma_n^2\mathbf{I} \tag{III.18}$$

where $\alpha(\varphi) = [\mathbf{a}^T(\varphi_{i-4}), \mathbf{a}^T(\varphi_{i-3}), \ldots, \mathbf{a}^T(\varphi_{i+4})]^T$ and $R_{js}(i)$ are referred to as the joint steering vector and the joint correlation coefficient matrix of the pixel pair i, respectively. Assuming that the neighboring pixels almost have identical terrain height [37], the joint steering vector will be as

$$\alpha(\varphi) = [1, e^{j\varphi_i}, 1, e^{j\varphi_i}, \ldots, 1, e^{j\varphi_i}]^T \tag{III.19}$$

The simplified steering vector of pixel i is denoted by $\mathbf{aj}(\varphi_i) = [1, e^{j\varphi_i}, \ldots, 1, e^{j\varphi_i}]^T(18 \times 1)$.

The present method can be summarized as follows. We first evaluate the (18×18) joint covariance matrix $C_{js}(i)$, which is eigen-decomposed, giving 18 eigenvalues $\lambda_i(i = 1, 2, \ldots, 18)$ along with their associated eigenvectors β_i $(i = 1, 2, \ldots, 18)$. The eigenvalues are sorted from largest to smallest in order to divide the matrix β into the two subspaces: $\beta = [\beta_s \beta_n]$. The noise subspace β_n includes $18 - K$ eigenvectors (instead of one eigenvector in Equation III.15), where K is the number of the principal eigenvalues of the matrix $C_{js}(i)$. When the SAR images are accurately coregistered $K = 1$. The MUSIC pseudospectrum is given by

$$J_2 = 1/\mathbf{aj}^H(\varphi)\beta_n\beta_n^H\mathbf{aj}(\varphi) \tag{III.20}$$

The optimal interferometric phase value is obtained by searching (with a step $\Delta\varphi$) in the phase interval $[-\pi, \pi]$ the value of φ that maximizes the pseudospectrum III.20. To improve the estimation accuracy for φ, the parameter $\Delta\varphi$ may be reduced but this increases the computational cost.

Here we propose a fast and efficient technique based on polynomial rooting instead of searching for peaks in the pseudospectrum III.16 (or III.20). The polynomial formulation is commonly used for estimating direction of arrival of multiple signal sources [39]. Here we propose the application of the method to the SAR interferometric phase estimation problem.

By defining the following matrix

$$Q = \beta_n\beta_n^H = \begin{bmatrix} q_{1,1} & q_{1,2} & \cdot & \cdot & q_{1,18} \\ q_{2,1} & q_{2,2} & \cdot & \cdot & q_{2,18} \\ \cdot & & & & \cdot \\ \cdot & & & & \cdot \\ q_{18,1} & q_{18,2} & \cdot & \cdot & q_{18,18} \end{bmatrix} \tag{III.21}$$

The denominator in III.20 becomes

$$\mathbf{aj}^H(\varphi)Q\mathbf{aj}(\varphi) = [1, z, \ldots, 1, z]Q[1, z^{-1}, \ldots, 1, z^{-1}]^T \tag{III.22}$$

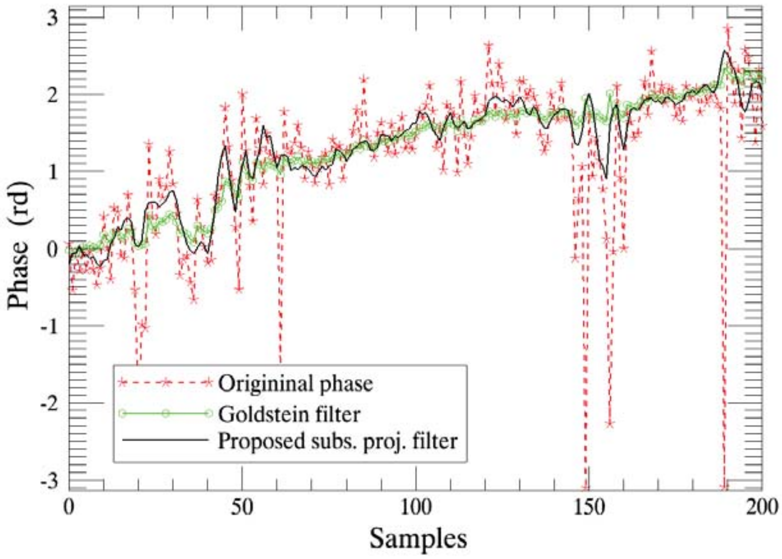

Figure III.9: Horizontal interferometric phase profiles.

where $z = e^{-j\varphi_i}$. We can cast Equation III.22 in the form of a polynomial whose coefficients are c_i.

$$D(z) = c_0 + c_1 z^{-1} + c_2 z^{-2} \tag{III.23}$$

with

$$\begin{cases} c_0 = \sum_{i,j=1}^{9} q_{2i-1,2j} \\ c_1 = \sum_{i,j=1}^{9} q_{2i-1,2j-1} + \sum_{i,j=1}^{9} q_{2i,2j} \\ c_2 = \sum_{i,j=1}^{9} q_{2i,2j-1} \end{cases} \tag{III.24}$$

$D(z)$ is a 2$^{\text{nd}}$ order polynomial which has two complex roots z_1 and z_2. The root $z_i = |z_i| \exp(j \arg[z_i])$ closest to the unit circle is selected and the interferometric phase is evaluated as $\varphi(i) = -\arg[z_i]$. Compared to existing methods based on the minimization of III.13 (or III.20), the proposed technique enjoys a substantially reduced computational complexity and improves the estimation of the interferometric phase φ.

The key steps of the proposed method are summarized as follows. After the image pair coregistration, the joint data vector is used to estimate the corresponding covariance matrix which is eigen-decomposed to form the joint noise subspace. A second order polynomial equation is solved and the root closest to the unit circle is selected. The corresponding argument is the optimal InSAR interferometric phase. The effectiveness of the method is verified using real SAR data. Figure III.9 depicts horizontal phase profiles over same flat area. It can be seen that the Goldstein filter offers smooth interferometric fringes, whereas the proposed method ensures topographic details preservation. For more information about the proposed method, please refer to [40].

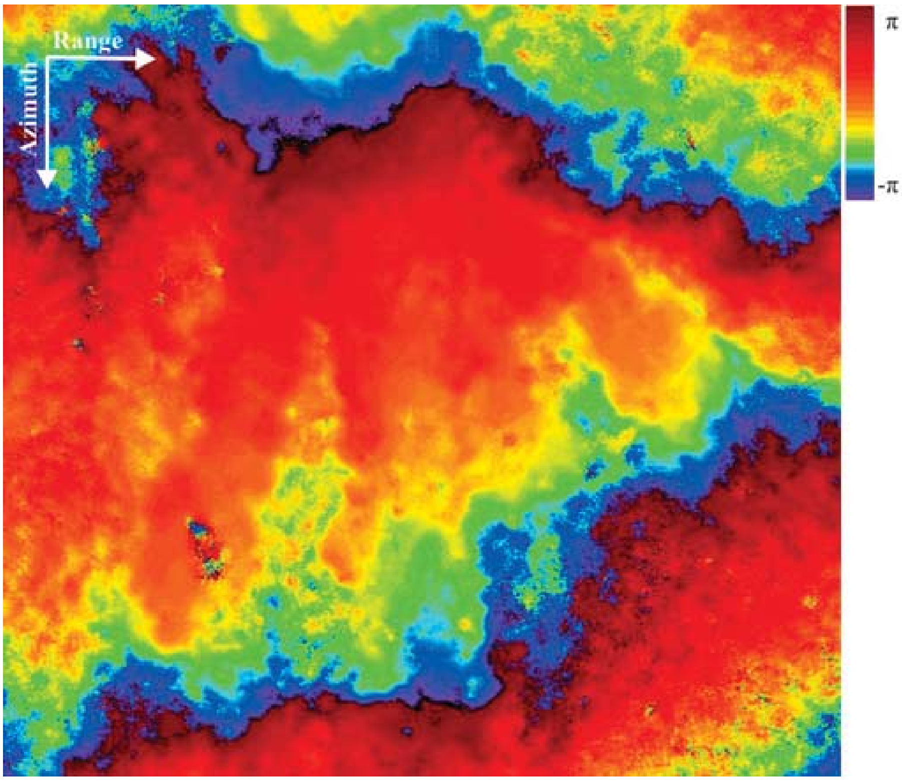

Figure III.10: Result of the complex multilooking (by factor 2 in both range and azimuth direction) followed by Goldstein filtering for the same interferogram as Figure III.7.

Complex multilooking

The complex multilooking during interferogram formation is considered as an "a priori" filtering operation. Indeed, the multilooking operation is famous for being efficient to reduce the speckle in SAR images but at the expense of the spatial resolution. Figure III.10 shows the obtained interferogram when using the complex multilooking. It can be clearly seen that details about altitude contours are more visible in the interferogram, which is of great importance for the phase unwrapping step (case of DEM generation). Obviously, this quality improvement has a cost: it is done at the expense of the spatial resolution which leads to the loss of details when detecting subtle changes.

III.4 InSAR coherence and decorrelation sources

The complex cross correlation coefficient is an important by-product of the interferogram formation. It is estimated as [31]:

$$\gamma = |\gamma| e^{j\phi} = \frac{\sum_{i=1}^{N} s_{1,i} \; s_{2,i}^{*}}{\sqrt{\sum_{i=1}^{N} |s_{1,i}|^2 \sum_{i=1}^{N} |s_{2,i}|^2}} \tag{III.25}$$

Here, the coherence $|\gamma|$ (magnitude of the complex cross correlation coefficient) measures the average correlation between two corresponding images s_1 and s_2 over a N-pixel local area in the scene and encodes the degree of scene similarity as a value in the range [0, 1]. It basically gives an evaluation of the reliability of the interferometric phase, and is used in the unwrapping process as a quality index of the pixel. In repeat pass interferometry, the coherence is mainly degraded by the acquisition geometry parameters, and by the target itself. Indeed, the coherence may be expressed as the product of a number of contributions [8]:

$$|\gamma| = \gamma_{SNR}\, \gamma_{proc}\, \gamma_{base}\, \gamma_{vol}\, \gamma_{temp} \tag{III.26}$$

- γ_{SNR} is determined by the relative backscatter signal to radar receiver noise ratio in the interferometric image pair.
- γ_{proc} is the decorrelation related to mismatch between primary and repeat-pass imagery.
- γ_{base} is the baseline decorrelation, which is related to the different look angles of the two SAR acquisitions, and leads to a critical baseline, above which the interferometric phase is pure noise. For ERS, assuming flat terrain, the critical baseline is about 1150 m.
- γ_{vol} is the volumetric decorrelation, which is caused by penetration of the radar wave through the scattering medium(e.g., vegetation and forest). It depends highly on the radar wavelength and the dielectric constant [8].
- γ_{temp} is the decorrelation caused by temporal changes in the land surface. It is due to geometrical or electrical changes in the properties of the surface, as a function of time between the acquisitions. These changes may be caused by moving parts of vegetation, erosion on the land surface, or Man-made activities. Temporal decorrelation is highly dependent on the operating frequency of the radar [8]. InSAR data acquired with longer wavelengths, for example L-band, exhibits a lower temporal decorrelation than those acquired in X-band.

If the repeat-pass imaging geometry is carefully designed and if the interferometric processing steps are performed correctly, it is possible to achieve $\gamma_{SNR}\, \gamma_{proc}\, \gamma_{base} \simeq 1$ [5]. In this case, the estimated coherence will reflect the underlying true scene coherence. Man-made scene disturbance may be detected as areas of low coherence against undisturbed

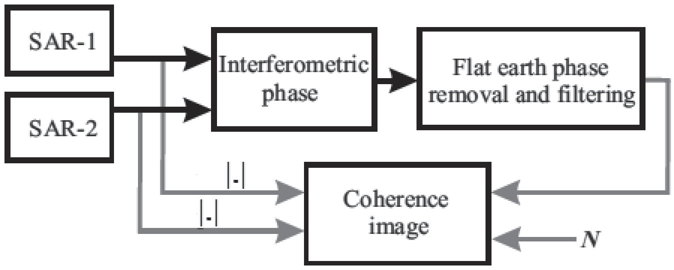

Figure III.11: Schematic representation of the different steps used for coherence evaluation in case of a CCD application.

areas that are characterized by high values of coherence [5].
In CCD, the detection of subtle surface changes requires great attention during coherence evaluation and analysis process. In fact, it is of great importance to get high coherence contrast between the changed and unchanged areas. For this reason, the coherence must be evaluated by using the following modified formula

$$\gamma' = \frac{\sum_{i=1}^{N} |s_{1,i}|\ |s_{2,i}| e^{j\phi_k}}{\sqrt{\sum_{i=1}^{N} |s_{1,i}|^2 \sum_{i=1}^{N} |s_{2,i}|^2}} \tag{III.27}$$

As shown in Figure III.11, the coherence is evaluated by using the filtered interferometric phase instead of the original interferogram. This means that the contribution of the orbital fringes and the interferogram noise are eliminated before coherence evaluation.

Figure III.12 depicts the coherence image that corresponds to the filtered interferogram of Figure III.7. The coherence map is obtained from the image pair using a $N = 3 \times 3$ sliding estimation window. Light-colored pixels represent values of γ near 1, while dark pixels represent values near 0. The selection of the case study was based on the availability of the high resolution CSK SAR data with an area composed of different types of soil. The agricultural fields, that are established on a lava emitted by the Niragongo volcano near Goma, preserve the coherence (light-colored surface). In this area, we can also distinguish roads and some cultivated parcels which are characterized by low coherence (dark-colored pixels). The rest of the scene is globally composed of vegetated fields. In this case the coherence is affected by the volumetric decorrelation, what makes the coherence low. This is due to the unstable individual leaves that comprise the composite response of each pixel, effectively randomizing the pixel reflectivity phase between the two passes. The interpretation of the coherence was validated using high resolution image of Google Earth. Through the present case study, we can conclude that the coherence faithfully

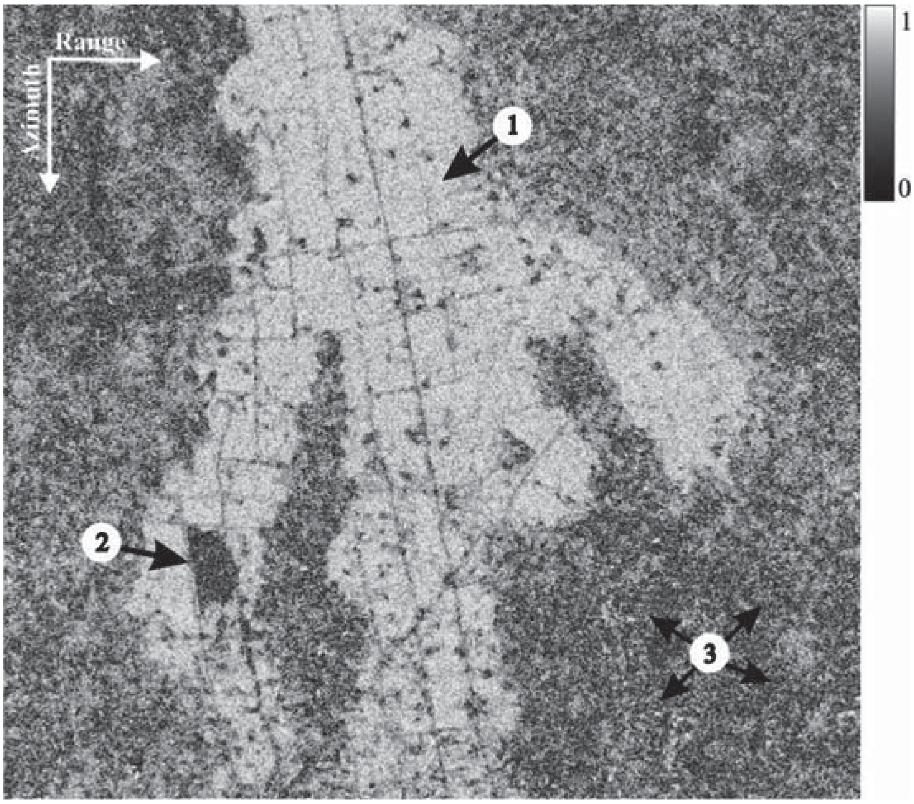

Figure III.12: Sample coherence evaluated over the repeat-pass image pair using $N = 3 \times 3$ pixel spatial estimation window: same area as Figure III.6. Light-colored pixels represent values of InSAR coherence near 1, while dark pixels represent values near 0. (1) Undisturbed parcels characterized by high coherence values, (2) Cultivated parcel with low coherence values, and (3) Natural vegetated area that is affected by volumetric decorrelation. COSMO-SkyMed^{TM} Product - ASI [2011] processed under license from ASI - Agenzia Spaziale Italiana. All rights reserved.

measures any changes that occur on the ground surface even if the two SAR intensity images appear identical to the eye.

III.5 Interferometric phase components

Recall that the expression of the interferometric phase given by Equation III.9 was obtained under the assumption that the scattering mechanism is identical in the two images. In repeat pass configuration, and due to the time delay between the two acquisitions, the flattened interferometric phase contains additional terms as follow [26]:

$$\phi = \phi_{topo} + \Delta\phi_{prop} + \Delta\phi_{scat} + \Delta\phi_{\delta R} \tag{III.28}$$

where:

- $\phi_{topo} \cong \frac{4\pi}{\lambda} \frac{B_\perp}{R \sin\theta} z$ is the topographic term [41].
- $\Delta\phi_{prop}$ is a possible delay difference due to ionospheric and tropospheric propagation conditions [29]. Tropospheric water vapor and rain cells are dominant sources for this phase error.
- $\Delta\phi_{scat}$ represents the influence of any change in scattering behavior. It may be a deterministic phase offset (i.e. change in dielectric constant) or a random phase (i.e. temporal decorrelation).
- $\Delta\phi_{\delta R}$ represents a possible displacement of the scatterers between the observations. ΔR is the projection of the displacement vector along the line-of-sight direction. In X-band ($\lambda = 3$ cm), one fringe (2π) in the differential interferogram represents a displacement δR of $\lambda/2$ (1.5 cm).

In each interferometry application, we are interested in one of the interferometric phase components. For DEM generation, the first term ϕ_{topo} is isolated when the other terms are minimised. In CCD application, the term $\Delta\phi_{scat}$ is of interest whose variability is measured by the coherence. In Differential-InSAR application, the last term $\Delta\phi_{\delta R}$ is extracted by eliminating the topographic contribution. Typically, the topography-related phase term is calculated from an external coarse DEM or from a second interferogram (three-pass). Therefore, while in the topographic applications the height corresponding to a phase cycle is dependent on the normal baseline, for a deformation interferogram a fringe corresponds always to the same amount of deformations, equal to half the used wavelength. The main limitation of the classical D-InSAR is that the interferogram can be corrupted by atmospheric artifacts [2]. Recently, some advanced techniques have been developed which use stacks of images (more than 10) to reduce the atmospheric artifacts. We can cite the two most well known techniques, namely Permanent Scatterers (PS) [42] and Small Baseline Subset (SBAS) [43]. However, the availability of the stacks of SAR images is not evident especially for the case of high-resolution data.

As said before, a pair of SAR images characterized by a small normal baseline reduces the effect of the relief, and in some uncommon situation it is possible to visually distinguish all of the various terms of the interferogram. As depicted in Figure III.13-a, the interferogram (flattened and filtered) shows clearly the fringes related to the displacement of the floating barge (shown previously in Figure II.13), in addition to the topographic fringes and the

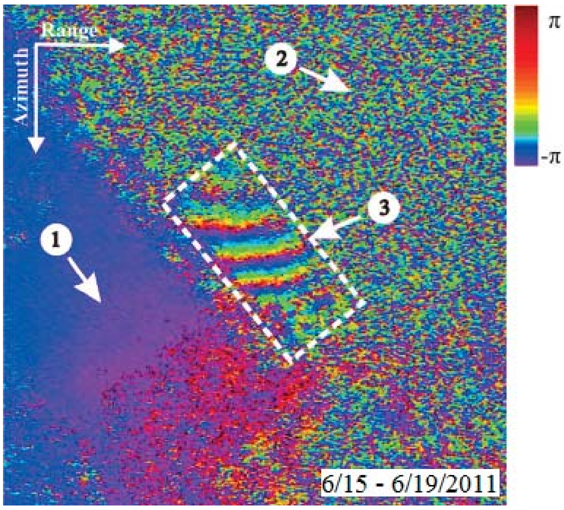

(a)

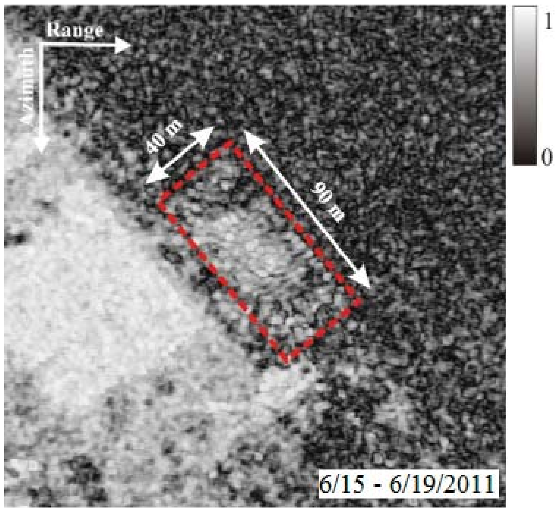

(b)

Figure III.13: Interferometric products of Zeebrugge port obtained using two CSK SAR images: covering same area as in Figure II.13. Baseline: $B_\perp$= 22 m $\rightarrow$ $z_{2\pi}$= 231 m. (a) Interferometric phase: (1) Topographic fringe of the port quay, (2) Phase change corresponding to the sea area, and (3) Displacement fringes of the floating barge. (b) Coherence image obtained by $N = 5 \times 5$ pixel spatial estimation window.

phase related to surface change (sea area). The reason of the visual identification between the two types of the fringes is that they are not of the same order. Indeed the altitude of ambiguity (topographic fringe) of the interferogram is about $z_{2\pi}$= 231 m while the displacement fringe is about δR = 1.5 cm. Since the floating barge is attached to the port, only the vertical movement is possible which is due to the variation of the tide level. Indeed, the barge coherence (see Figure III.13-b) is preserved over the two SAR acquisitions and about four fringes (δR =6 cm) can be measured on the interferogram.

III.6 Limitation of SAR interferometry

Repeat-pass SAR interferometry is mainly feasible from L-band to X-band. Below L-band, ionospheric signal will deteriorate the observations and above X-band the instrument is too sensitive to weather conditions. SAR interferometry only works under coherent conditions, for which the received reflections are correlated between the two SAR images. obviously, this is the most important condition for interferometry. Ideally, the interferometric phase would be related to the topography of the scene. Unfortunately this is not

true and the phase will be erroneous, probably due to a number of sources including (but not limited to): speckle noise, atmospheric artifacts, temporal decorrelation, geometric decorrelation and orbital inaccuracies.
As said before, the effect of some sources of decorrelation, e.g., as introduced by the alignment and interpolation of the images, can be reduced by using well-designed filtering procedures. Other sources of decorrelation are more significant and non-reversible [29]. The "pixel size limit" restricts the spatial extent of an observable movement to values much larger than the dimension of a focused radar pixel. Due to the limited bandwidth, a phase gradient larger than cycles/pixel (approximately 0.822 for ERS) results a complete loss of correlation [26]. In practice, abrupt changes in topography, such as volcanic eruptions, can exceed this limit.
Other limitations in the interpretation of interferometry depend on the application of the products. For example, for DEM generation, micro-topography may have to be considered. Within each resolution cell the actual height may vary considerably, for example in the case of buildings depend on the dominant scatterers within the resolution cell, e.g., a roof top. In layover areas, scattering from various separated locations may contribute to the phase observation, leading to an ambiguity that cannot be solved. For areas that lack significant return signal (low backscatter areas, i.e., due to specular reflection) the phasors are too short to provide a useful phase observation. Finally, strong scatterers may create significant sidelobes in the interferogram. These sidelobes can contaminate significantly the phase observations in the neighboring resolution cells , which can result in an erroneous interpretation of these phase values [29].

III.7 Summery

The principle of SAR interferometry (InSAR) has been introduced, together with various applications and the processing steps used to generate the interferogram. Particular attention has been given to the phase filtering, which is of great importance for the success of all InSAR processing. The subspace projection based filter is presented, together with our contribution in the improvement of the phase estimation. The InSAR coherence has been introduced together with the different decorrelation sources. Several examples obtained with high resolution SAR data have been given and discussed. Finally, some limitations of the InSAR technique have been highlighted.

CHAPTER IV

INSAR COHERENCE ESTIMATION

IV.1 Introduction

In repeat-pass configuration, the two SAR images are taken at different times, and the coherence reveals various decorrelations. An analysis of the sources of decorrelation in interferometric radar echoes may be found in [8]. The observed coherence is influenced by different factors, which depend both on sensor geometry and target characteristics. As said in Chapter III, if the interferometric processing steps are performed correctly, the InSAR coherence may reflect the true scene coherence over the repeat-pass interval. The InSAR coherence is useful in giving information about the man-made activities, but unfortunately the coherence estimator is biased [15], which complicates the coherence map analysis and interpretation.

This chapter introduces the concept of the InSAR coherence estimation. The statistical modeling of decorrelation is presented. It is shown that the sample coherence estimator is biased, especially for low-coherence values. The coherence estimation performance are studied using high resolution SAR images. Focus is given to the influence of the SAR speckle and the number of samples used to estimate the coherence, which are the two most determinant parameters that limit the CCD performance.

IV.2 Statistical modeling of decorrelation

In the following paragraph, we present the statistical modeling first of single image, and then of the interferometric process as the combination of two such images. Finally, the statistical description of the coherence bias is described.

IV.2.1 Complex PDF SAR resolution cell

The response of the resolution cell on earth to the arriving radar pulse is strongly dependent on the scattering mechanisms involved. For SAR systems where size of the resolution cell is many times larger that the radar wavelength, many terrain elements or scatterers contribute to the response of the resolution cell [24]. The measured reflection is therefore the sum of many scatterers responses, see Figure IV.1. Let us assume the following [24]:

1. No single scatterer dominates the others in a resolution cell.

2. The phase of every individual scatterer is uniformly distributed between $-\pi$ and π.

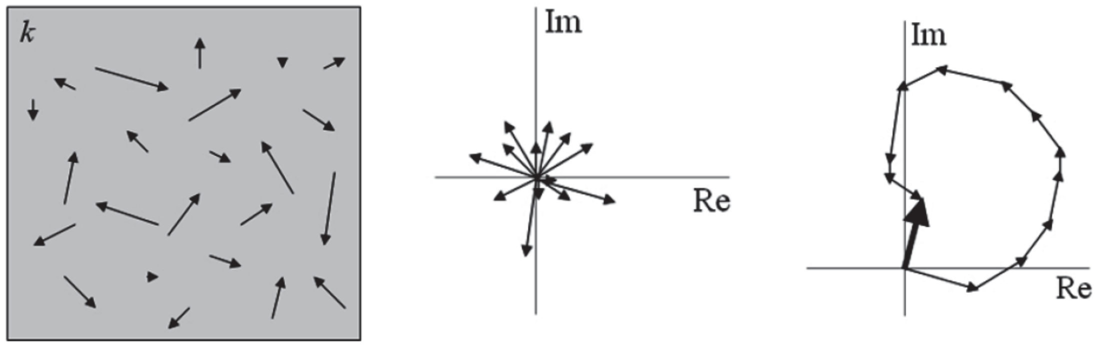

(a) (b) (c)

Figure IV.1: Summation of scatterers responses within a resolution cell k. (a) The distribution of N individual scatterers within a resolution cell. (b) All scatterers translated to the same origin. (c) The sum of all scatterers. The bold arrow indicates the sum, which is the complex observable s_k.

3. The scatterers have phase and amplitude statistically independent (uncorrelated) from each other.

Using these assumptions, it is possible to apply the central limit theorem, which defines the observations s_k as zero mean complex circular Gaussian random variables. The probability density function (pdf) of s (or the joint pdf of its real and imaginary component) is written as [29]:

$$\mathrm{pdf}(s) = \mathrm{pdf}(\mathrm{Re}\{s\},\ \mathrm{Im}\{s\}) = \frac{1}{2\pi\sigma^2}\exp\left(-\frac{(\mathrm{Re}\{s\})^2 + (\mathrm{Im}\{s\})^2}{2\sigma^2}\right) \tag{IV.1}$$

where

$$\sigma^2 = \sigma_s^2 = \sigma^2_{\mathrm{Re}\{s\}} = \sigma^2_{\mathrm{Im}\{s\}} \tag{IV.2}$$

is the mean backscatter power of the scene.

Equation IV.1 can be expressed in terms of amplitude a and phase ψ by the following relations:

$$\mathrm{Re}\{s\} = a\ \cos(\psi) \qquad \mathrm{Im}\{s\} = a\ \sin(\psi) \tag{IV.3}$$

Since the Jacobian determinant of this transformation is a, the pdf takes the form:

$$\mathrm{pdf}(a,\ \psi) = \begin{cases} \frac{a}{2\pi\sigma^2}\exp(-\frac{a^2}{2\sigma^2}) & \text{for } a \geq 0 \text{ and } -\pi \leq \psi \leq \pi \\ 0 & \text{otherwise.} \end{cases} \tag{IV.4}$$

The marginal pdf for the magnitude a is obtained by integrating ψ out, between $-\pi$ and π. This yields

$$\text{pdf}(a) = \begin{cases} \frac{a}{\sigma^2} \exp(-\frac{a^2}{2\sigma^2}) & \text{for} \quad a \geq 0 \\ 0 & \text{otherwise.} \end{cases} \tag{IV.5}$$

Equation IV.5 is the Rayleigh distribution [29]. The marginal pdf for the phase ψ is found by integrating IV.4 over a , between 0 and ∞:

$$\text{pdf}(\psi) = \begin{cases} \frac{1}{2\pi} & \text{for} \quad -\pi \leq \psi \leq \pi \\ 0 & \text{otherwise.} \end{cases} \tag{IV.6}$$

Equation IV.6 describes a uniform distribution. This explains why the phase from only one SAR image does not bear any useful information. From IV.4, IV.5, and IV.6 it follows that a and ψ are uncorrelated, since

$$\text{pdf}(a,\ \psi) = \text{pdf}(a)\ \text{pdf}(\psi) \tag{IV.7}$$

The pixel intensity variation for a distributed scene, expressed by the exponential pdf, is known as speckle. Assuming ergodicity, averaging of resolution cells is often applied to reduce the effect of speckle. As a result the pdf of the intensity value of N averaged resolution cells can be described by a χ^2-distribution pdf with $2N$ degrees of freedom [24]:

$$\text{pdf}(I_{2N}) = \frac{I^{N-1}}{(2\sigma^2)^N \Gamma(N)} \exp(-\frac{I}{2\sigma^2}) \tag{IV.8}$$

Note that for $N = 1$ this equal to the exponential pdf, while $N \rightarrow \infty$ it equals a Gaussian pdf.

IV.2.2 Complex PDF interferometric resolution cell

The behavior of a single SAR resolution cell, under the assumption of a distributed scattering mechanism, was described by circular Gaussian statistics. Although the pdf of the phase has a uniform distribution, the phase of the complex product of two circular Gaussian signals is **not necessarily uniform**, as long as the two signals have some degree of correlation [26]. The joint pdf of two circular Gaussian signals s_1 and s_2, with $E\{s_1\}$=$E\{s_2\} = 0$ and $E\{s_1^2\}$=$E\{s_2^2\}$ can be written as [24]:

$$\text{pdf}\{s_1,\ s_2\} = \frac{1}{\pi^2 |C_s|} \exp\{-[s_1^*,\ s_2^*] C_s^{-1} \begin{bmatrix} s_1 \\ s_2 \end{bmatrix} \} \tag{IV.9}$$

where C_s is the complex covariance matrix, defined by

$$C_s = E\{\begin{bmatrix} s_1 \\ s_2 \end{bmatrix} [s_1^*,\ s_2^*]\} = \begin{bmatrix} E\{|s_1|^2\} & \gamma\sqrt{E\{|s_1|^2\}E\{|s_2|^2\}} \\ \gamma^*\sqrt{E\{|s_1|^2\}E\{|s_2|^2\}} & E\{|s_2|^2\} \end{bmatrix} \tag{IV.10}$$

and its determinant is given by

$$|C_s| = E\{|s_1|^2\}E\{|s_2|^2\}(1 - |\gamma|^2) \tag{IV.11}$$

The complex coherence (or normalized complex correlation coefficient) γ is defined as [15]

$$\gamma = \frac{E\{s_1 s_2^*\}}{\sqrt{E\{|s_1|^2\}E\{|s_2|^2\}}} \tag{IV.12}$$

where $E\{.\}$ denotes the expectation (ensemble average). From Equation IV.12, γ represents simply the average of the cross multiplication of the two complex signals normalized by square root of the products of the individual signal powers.

IV.2.3 Coherence estimation bias

In practical situations, the phase observations of a uniform region is assumed to be stationary. Under the assumption of ergodicity, it is possible to estimate the expectation in Equation IV.12 with the spatial average, obtained over a limited area surrounding the pixel of interest. This assumption is used to obtain the maximum likelihood estimator, given by Equation III.25, of γ over an estimation window of N pixels [41]. As shown previously in Chapter III the magnitude $|\gamma|$, i. e. the coherence, is a measure of the interferometric phase variability. Rodriguez and Martin [41] also showed that the maximum likelihood estimator of the interferometric phase, for distributed scattering mechanisms (constant phase), is given by

$$\hat{\phi} = \phi_0 = \arctan\left(\frac{\mathrm{Im}\sum_{i=1}^{N} s_{1,i}\ s_{2,i}^*}{\mathrm{Re}\sum_{i=1}^{N} s_{1,i}\ s_{2,i}^*}\right). \tag{IV.13}$$

which is unbiased modulo 2π. The probability density function for the estimated phase is complicated. Joughin and Winebrenner [44] found an equivalent expression, using a hyper-geometric function:

$$\mathrm{pdf}(\hat{\phi},\ N) = \frac{\Gamma(N+1/2)(1-|\gamma|^2)^N|\gamma|\cos(\hat{\phi}-\phi_0)}{2\sqrt{\pi}\Gamma(N)(1-|\gamma|^2\cos^2(\hat{\phi}-\phi_0))^{N+1/2}} + \frac{(1-|\gamma|^2)^N}{2\pi} \times {}_2F_1(N,\ 1;\ 1/2;\ |\gamma|^2\cos^2(\hat{\phi}-\phi_0)) \tag{IV.14}$$

where Γ is the Gamma function and ${}_nF_m$ is the hyper-geometric function [29].

The pdf of the phase for different number of samples is shown in Figure IV.2-(a), where

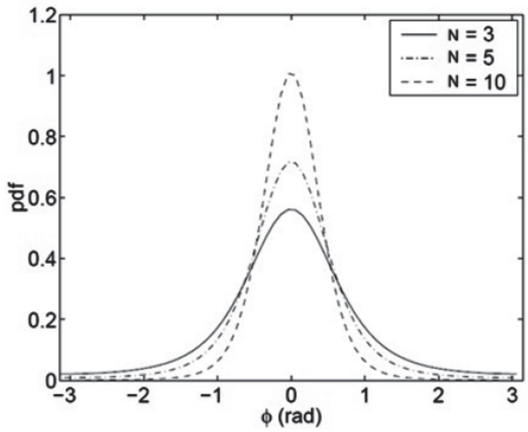

(a)

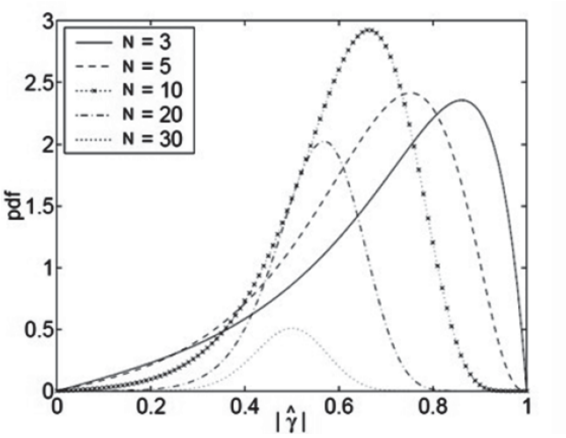

(b)

Figure IV.2: Probability density function for different number of looks of: (a) interferometric phase. (b) Coherence (ϕ_0 is assumed to be zero and $|\gamma| = 0.5$).

coherence value of 0.5 has been assumed. As can be seen in the figure, with increasing number of looks the distribution becomes narrower (better estimation). As for the coherence, the probability density function of its estimated value, represented in Figure IV.2-(b), takes the form [15]:

$$\mathrm{pdf}(|\hat{\gamma}|,\ N) = 2(N-1)(1-|\gamma|^2)^N|\hat{\gamma}|(1-|\hat{\gamma}|^2)^{N-2} \times\ {}_2F_1(N,\ N;\ 1; |\gamma|^2|\hat{\gamma}|^2) \quad \text{(IV.15)}$$

The mean value is given by [15]:

$$E\{|\hat{\gamma}|\} = \frac{\Gamma(N)\Gamma(3/2)}{\Gamma(N+1/2)} \times\ {}_3F_2(3/2,\ N,\ N;\ N+1/2,\ 1; |\hat{\gamma}|^2) \times\ (1-|\hat{\gamma}|^2)^N \quad \text{(IV.16)}$$

As already mentioned in Chapter III, the coherence estimator is biased. The bias affects particularly the lower coherence values, as shown in Figure IV.3, and decreases for increasing number of samples N. For example, for $N = 10$, the coherence is significantly **over estimated** for $|\gamma| \leq 0.4$. The variance of the coherence magnitude estimator is derived from Equation IV.15 as well:

$$\sigma^2_{|\hat{\gamma}|} = \frac{\Gamma(N)\Gamma(2)}{\Gamma(N+1)} \times\ {}_3F_2(2,\ N,\ N;\ N+1,\ 1; |\hat{\gamma}|^2) \times\ (1-|\hat{\gamma}|^2)^N - E\{\hat{\gamma}\}^2 \quad \text{(IV.17)}$$

The Cramer-Rao bound, which is a lower bound for the variance (assuming unbiased estimation) is defined as

$$CRB_{|\hat{\gamma}|} = \frac{(1-|\gamma|^2)^2}{2N} \leq \sigma^2_{|\hat{\gamma}|} \quad \text{(IV.18)}$$

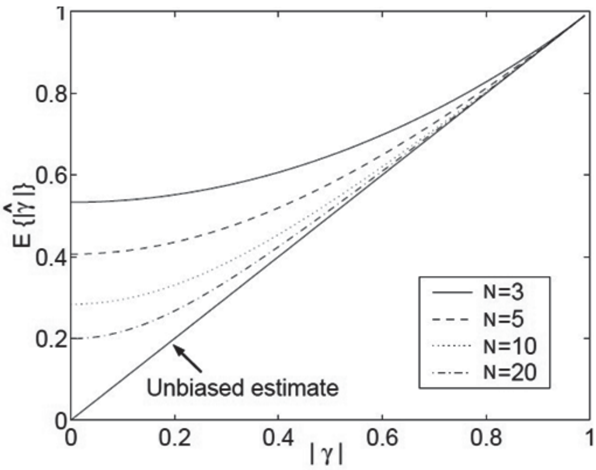

Figure IV.3: Bias of the coherence estimate for different values of N.

Touzi et al. [15] propose different methods to reduce the coherence bias. The first method namely space averaged coherence samples is efficient particularly using high resolution SAR data, and will be discussed in Chapter V. The second method is based on the inversion of the Equation IV.16 which is only possible when the variance $\sigma^2_{|\hat{\gamma}|}$ is low or when N is sufficiently large.

IV.3 InSAR coherence and decorrelation sources

IV.3.1 Decorrelation sources

The observed coherence depends not only on target properties but also on geometric relations between the two acquisitions and on radar thermal noise. The coherence may be expressed mainly as the product of the dominant contributions [8]:

$$\gamma = \gamma_{SNR}\gamma_{\text{geom}}\gamma_{\text{temp}} \tag{IV.19}$$

- The component γ_{SNR} is the relative backscatter signal to radar receiver noise ratio (SNR) in the interferometric image pair,
- γ_{geom} is the geometric decorrelation that is mostly related to the satellite tracks separation, and
- γ_{temp} is the temporal decorrelation caused by changes in the land surface, e.g., man-made objects, vegetation change or ploughing. It is the dominant factor in the repeat pass configuration.

Thermal decorrelation

Using the correlation model of Zebker and Villasenor [8], we model the radar echoes as consisting of correlated part c common to the both images and also of noise parts n_1, and n_2

$$s_1 = c + n_1 \qquad s_2 = c + n_2 \tag{IV.20}$$

where the noise terms may be due to the radar thermal noise, or coregistration errors or any artifacts present in the signals. The thermal decorrelation γ_{SNR}, which ranges between 0 and 1, can be equivalently described as a function of signal to noise ratio (SNR)

$$\gamma_{SNR} = \frac{SNR}{SNR + 1} \tag{IV.21}$$

Generally in the absence of temporal changes, the signal is significantly stronger than the noise (high values of SNR). There are, however, several common situations where the signal is weak. One situation is when the area is a smooth surface that reflects the radar energy away with little backscatter. Bodies of water, asphalt roads, and building roofs are such areas. Another situation is in areas of shadow. Areas of low SNR show up as dark areas in a SAR image intensity. Obviously, if the SNR is too low, it is not possible to detect changes or generating the DEM. In this thesis, the problem of low SNR will be addressed later as a problem of change classification (Chapter VI).

Geometric decorrelation

Geometric (spatial baseline) decorrelation is a result of a difference in the angle of incidence between the two sensors at the earth's surface [45]. There are two ways to estimate the spatial decorrelation. One way is by using a range spectral filter [45], and the other way is by using the following model [8].
We define $B_{\perp,\mathrm{crit}}$ as the baseline causing a spectral shift equal to the signal bandwidth B. It is a function of the wavelength λ, the incidence angle θ and the terrain slope ξ [8]

$$B_{\perp,\mathrm{crit}} = \lambda(B/c)R\tan(\theta - \xi) \tag{IV.22}$$

The geometric decorrelation can be simply defined as

$$\gamma_{\mathrm{geom}} = \begin{cases} 1 - \frac{B_\perp}{B_{\perp,\mathrm{crit}}}, & |B_\perp| \leq B_{\perp,\mathrm{crit}} \\ 0, & |B_\perp| > B_{\perp,\mathrm{crit}} \end{cases} \tag{IV.23}$$

For a flat terrain, the ERS critical baseline is approximately 1.1 km. A rectangular spectrum was assumed in this derivation. In mountainous area, high values of the topographic slope ξ, the geometric decorrelation is significant and must be eliminated as in [46] to isolate only the temporal component of interest.

Temporal decorrelation

Temporal decorrelation include both the natural surface changes and the man-made changes. The natural surface changes, also known as volumetric decorrelation, increases with the amount of vegetation cover because the scatterers on the plants change with time. CCD often seeks to isolate only the man-made changes, which can be caused by walking across grass, driving over a gravel road, cultivating parcels,...etc. Man-made objects, such as moved vehicles or containers, cause also decorrelation in the coherence image. For flat areas, and through an appropriate interferometric processing, it is possible to achieve $\gamma_{SNR}\gamma_{\text{geom}} \simeq 1$ [5]. In this case, the coherence γ will only measure the temporal changes γ_{temp} of the imaged scene.
In order to distinguish between the changed and unchanged pixels in the scene, the CCD map can be easily obtained by a simple thresholding of the coherence image. The natural changes, caused by the vegetation, introduce undesired decorrelation in the scene creating false CCD targets. High coherence values are generally obtained for areas without lush vegetation (i.e., arid areas or polar areas). Especially for vegetated areas longer wavelength radar data, for instance L-band, are preferred over C-band or X-band data, since these instruments are less sensitive to small changes in the scattering characteristics.
CCD at X-band is, on the one hand, difficult because that many of the decorrelation sources (geometric, volumetric) are inversely proportional to the wavelength. While using high resolution SAR data, more advanced algorithms of image coregistration and filtering are then required to reduce as possible thermal decorrelation. On the other hand, X-band presents the advantage of being sensitive to smaller man-made changes in the scene because of the smaller wavelength. A general rule is that a change of 0.2 times the wavelength will cause complete decorrelation [4]. X-band is therefore sensitive to changes on the order of several millimeters versus several centimeters for L-band. Finally, we can conclude that the CCD with high resolution SAR X-band data, and with a short revising time, can be considered as the most interesting technology to detect and monitor accurately the man-made activities over a large flat area.

IV.3.2 Phase corrected coherence

The coherence as determined using Equation III.25 (or III.27) is affected by interferometric phase variation due to (i) noise in the data and/or to (ii) systematic phase variation within the coherence estimation window. The systematic phase variation (known also as local phase slope) is a result of effective path variations over the scene, which can mainly be attributed to the terrain topography. For this reason, the local phase slope needs to be corrected in mountainous areas. This is to avoid the coherence misestimation due to the phase rotation within the estimation window. This necessitates an adapted definition of the coherence, the phase-corrected coherence $\hat{\gamma}_{PC}$ defined as [47]:

$$\hat{\gamma}_{PC} = \frac{|\sum_{i=1}^{N} s_{1,i}\ s_{2,i}^{*} \exp(-j\phi_{sys}^{i})|}{\sqrt{\sum_{i=1}^{N} |s_{1,i}|^2 \sum_{i=1}^{N} |s_{2,i}|^2}} \tag{IV.24}$$

where ϕ_{sys} is the systematic phase component for each pixel.
The local phase slope can be compensated by using an external DEM or by using the Local Fringe Frequency (LFF) components [48].
By processing various high resolution SAR images over flat areas, it is found that the LFF components represent also useful parameters in the CCD map improvement (more details about LFF estimation will be given in Chapter V).

IV.4 Coherence of high resolution SAR images

As showed previously, the sample coherence estimator is biased particularly for low-coherence values. The bias decreases when the number N of samples increases. In the following paragraphs, we illustrate the difficulty of using InSAR coherence for the CCD application.

IV.4.1 Influence of the SAR speckle in InSAR coherence

In order to study the effect of the SAR speckle on the coherence estimation, it is interesting to investigate the influence of the complex multilooking (see Chapter III) during the interferometric process. In fact, the multilooking operation is famous for being efficient to reduce the speckle in SAR images but only at the expense of spatial resolution.
As presented in Figure IV.4, we propose in this section to study the impact of speckle reduction before coherence estimation when the complex multilooking operation is used.

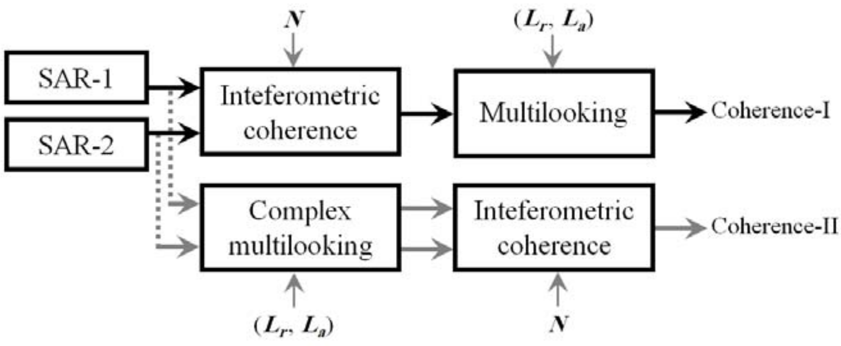

Figure IV.4: Schematic diagram for studying the influence of the SAR speckle on coherence estimation. N is the number of samples used for the coherence estimation. L_r and L_a are the multilooking factors respectively in range and azimuth direction.

The area of interest, showed in Figure IV.5, concerns flat agricultural fields that are established on a laved emitted by the Niragongo volcano near Goma city. Figure IV.5-(a) shows the filtered interferometric phase, obtained without complex multilooking (full resolution processing). For areas without surface activity, as in Figure IV.5(a)-1, the interferometric phase mainly consists of the topographic information with quite steady values. For a cultivated area as in Figure IV.5-2, and for the natural vegetated areas as in Figure IV.5-3, the interferometric phase is characterized by random values.
As shown in Figure IV.5-(b), the use of SAR complex multilooking of only 4 samples during the interferometric process, highly improves the estimation of the different phase components. It can be clearly seen that details about altitude contours in Figure IV.5(b) are now clearly visible, which is of great importance for the phase unwrapping step (case of the DEM generation). The situation in which the multilooking factor is equal to 4 is often encountered when medium resolution images (ERS, ALOS, Envisat) are used, and then a similar phase quality improvement as in Figure IV.5(b) is achieved. Obviously, when using high resolution SAR data, the phase quality improvement has a cost; it is at the expense of the spatial resolution which leads to the loss of details when detecting changes as in Figure IV.5(b)-2.
Figure IV.5-(c) depicts the coherence image that corresponds to the interferometric phase of Figure IV.5-(a). The coherence map is estimated with $N = 3 \times 3$ sliding estimation window. Light-colored pixels represent values of the coherence near 1, while dark pixels represent values near 0. The uncultivated agricultural fields, as in Figure IV.5(c)-1, preserve the coherence (light-colored surface). The roads that delimitate the parcels and the

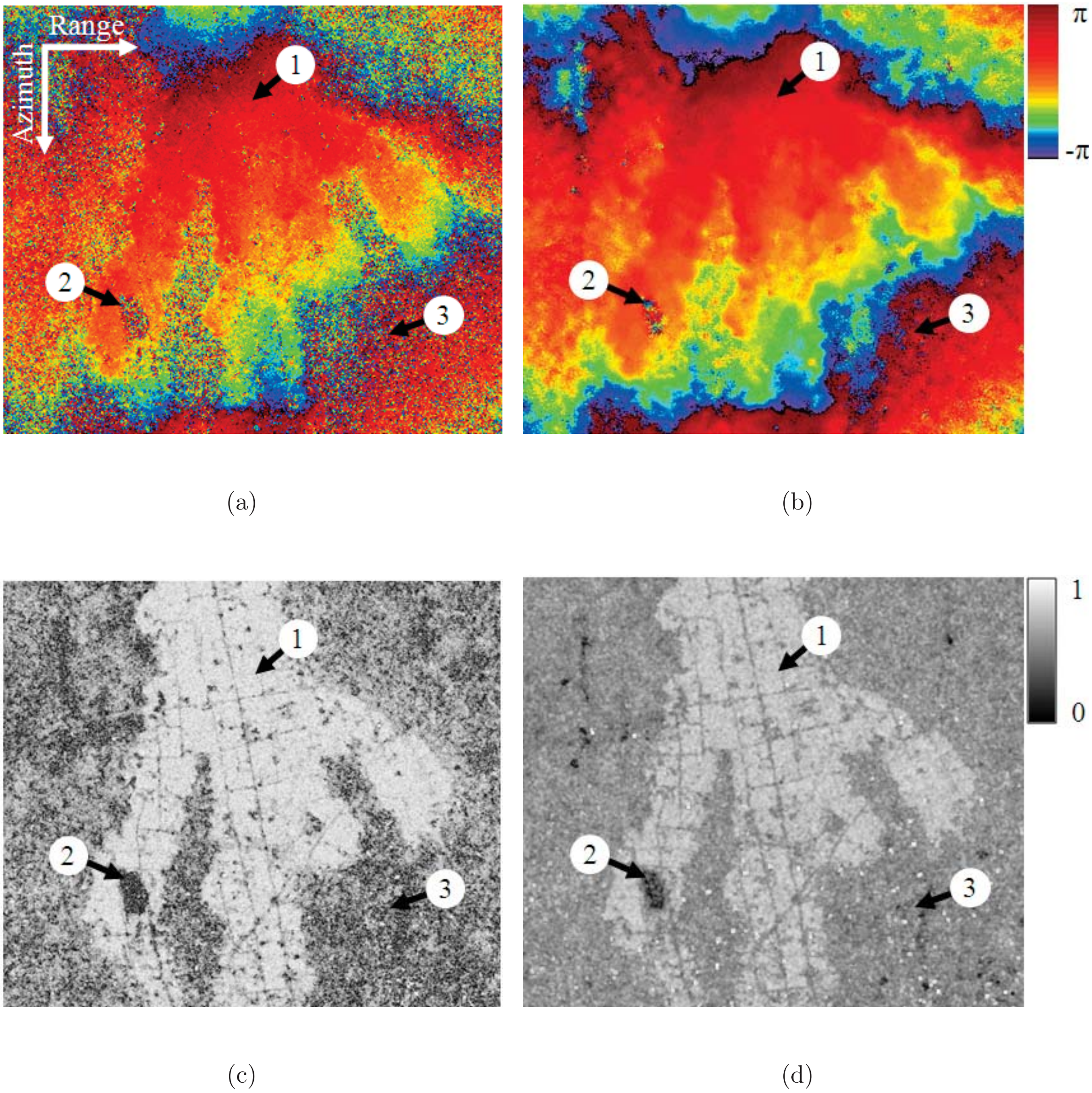

Figure IV.5: Influence of the complex multilooking operation into the interferometric products. (a) Interferometric phase obtained without complex multilooking. (b) Interferometric phase obtained with a complex multilooking factor of 2 (both in range and azimuth directions). (c) Coherence image obtained without complex multilooking. (d) Coherence image obtained with a complex multilooking factor of 2 (both in range and azimuth directions).

cultivated parcel as in Figure IV.5(c)-2 are characterized by low coherence (dark-colored pixels). The rest of the scene is affected by the volume decorrelation caused by the foliage as in Figure IV.5(c)-3, what makes the coherence low. Figure IV.5-(d) depicts the coherence image corresponding to the interferometric phase of Figure IV.5-(b). The coherence

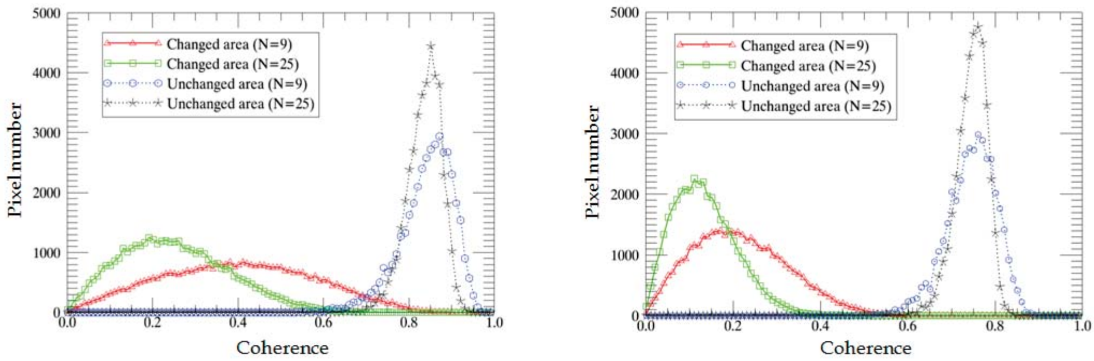

(a) (b)

Figure IV.6: Coherence histograms evaluated for different values of N. (a) Coherence of changed and unchanged areas obtained without complex multilooking. (b) Coherence of changed and unchanged areas obtained using complex multilooking.

map of Figure IV.5-(d) represents more faithfully the real scene coherence but at expense of the spatial details preservation, which is required in the CCD application. Results of Figure IV.5 show clearly the difficulty of using the interferometric products without reducing speckle in SAR data.

IV.4.2 Influence of the number of samples N

In this section, we are interested by the significance of the number of samples N on the coherence estimation when high resolution SAR images are used. It consists in studying the coherence behaviour in two specific areas, which are the cultivated parcel of Figure IV.5(c)-2 and undisturbed parcel of Figure IV.5(c)-1.

Figure IV.6-(a) depicts histograms of coherence images evaluated for different number N of samples. The presence of a lot of highly coherent pixels can be seen inside the changed area (light-colored pixels inside the cultivated parcel in Figure IV.5(c)-2). In CCD application, these highly coherent pixels inside changed areas are considered as outliers and must be discarded. According to Figure IV.6-(a), the coherence evaluated using $N = 5 \times 5$ represents more faithfully the coherence of the changed area than the coherence evaluated by $N = 3 \times 3$, as there are less highly coherent samples inside the changed area. The coherence mean value of the selected changed area is about 0.24 with $N = 5 \times 5$ against 0.43 for $N = 3 \times 3$. It is important to point out that the coherence histograms of the changed area correspond to the same selected area, as in Figure IV.5(c)-2, and the discrepancy in the results is only due to the increasing number N of samples. On the contrary, in case of the unchanged area as in Figure IV.5(c)-1, the coherence mean value is practically not affected by increasing the number N of samples. According to Figure IV.6-(a), the coherence mean value of the unchanged area is about 0.82 for both $N = 3 \times 3$ and 5×5, which may be explained by the fact that the coherence estimate is particularly biased for the low coherence values. Figure IV.6-(b) shows that the use of the complex multilooking of the SAR images leads to a better separation between the changed and unchanged areas, but at the expense of the spatial resolution.

The results of Figure IV.6, similar to those in [15], show the necessity to increase the number of samples to obtain a good separation between coherence values of the changed and unchanged areas. In CCD applications, the challenge consists in separating as much as possible the changed and the unchanged pixels, using small window-size N and without complex multilooking, to preserve subtle changes as much as possible.

In the rest of the thesis, the SAR interferometric processing is done in full resolution with a small window-size of $N = 3 \times 3$ pixels, corresponding approximately to an area of 2.4×2.4 m^2. According to Figure IV.6, this corresponds to the most unfavorable situation of bad separation between the changed and unchanged classes, thus an additional processing step is necessary to improve the InSAR coherence map.

IV.5 Conclusion

In this chapter, the InSAR coherence estimation is investigated and particular attention is paid to the coherence bias that affects the low coherence values. The theoretical study shows that the bias is more pronounced in the low coherence areas and that the effect of the bias can be reduced by increasing the number of samples used for estimating the coherence. When high resolution SAR images are used, it has been demonstrated that the cause of this bias, in addition to the presence of speckle in SAR data, is the appearance of highly coherent pixels inside changed areas, which complicates the coherence analysis and interpretation. In CCD applications, which require spatial details preservation, the coherence must be evaluated in full resolution and with using low number of samples. Unfortunately, this corresponds to the most unfavorable situation of bad separation between the changed and unchanged areas coherences. For that reason, it is interesting to investigate in Chapter V methods that are able to improve the coherence map quality without affecting spatial resolution.

CHAPTER V

INSAR COHERENCE IMPROVEMENT

V.1 Introduction

In CCD, the coherence between two SAR images is evaluated and analyzed to detect ground changes. The ultimate goal is to produce a binary map corresponding to two classes: change and no change. As shown previously in Chapter IV, the sample coherence estimator is biased, especially for low-coherence values. The cause of this bias, in addition to the presence of speckle in SAR data, is the appearance of highly coherent pixels inside changed areas. Within this context, the detection performance will considerably degrade, particularly when using high resolution SAR data. In this study we did not interested in reducing the SAR speckle via filtering (e.g. Lee, Frost, ..., etc.) as the existing filters act only on the intensity of the SAR images.

A speckle based method has been proposed in [16] for InSAR coherence estimation. It has been demonstrated that in case of low coherences, the stochastic behavior of the Hermitian products [Equation III.25] is determined by a complex additive speckle noise component. On the contrary, speckle in high coherence areas is determined by a multiplicative noise component. Various algorithms have been proposed in [16] to reduce the effect of the coherence bias, but unfortunately these methods are inefficient when tested on high resolution SAR data.

This chapter is dedicated to methods that permit improvement of the InSAR coherence maps, while preserving detection of small size changes. In the first part of this chapter, the change detection performance of the basic MLD method is investigated, and compared to the Ordered Statistic (OS) and the Censored Mean Level Detector (CMLD) methods. The second part of this chapter concerns the use of Local Fringe Frequencies (LFF), as a second change indicator to better analyze the InSAR coherence image. Two LFF-based methods are developed and tested on high resolution SAR data. A comparative study highlights the advantages and the limitations of the proposed methods in various environment types. Finally, the enhanced method to build CCD maps is applied to earthquakes damages assessment.

V.2 Coherent Change Detection

A simple threshold applied to the coherence image may be used to distinguish between the changed and unchanged regions in the scene [5]. This detector offers low detection performance which is due to the presence of highly coherent pixels inside changed areas (see

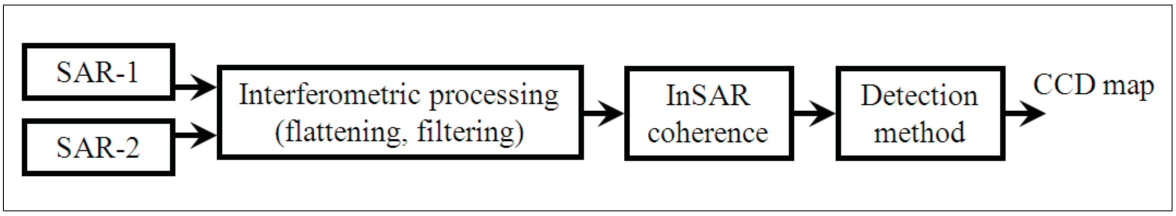

Figure V.1: General scheme of the CCD map generation process.

Section V.3, more details are found in [49]). According to Figure IV.6, the results show the necessity of increasing the number N of samples to obtain a good estimate of the coherence, which leads to a better separation between changed and unchanged coherence areas. But using high N values also causes the loss of spatial details in the coherence image, hence the necessity to develop detection methods that improve the CCD map. In this section we are interested in detection strategies with a structure given by the diagram of Figure V.1. After InSAR coherence estimation, methods are applied for detection performance improvement in order to obtain reliable CCD maps.

V.2.1 Mean Level Detector (MLD)

In order to improve the change detection performance, one can evaluate the average of coherence samples over a M-pixel local area. This method was proposed by Touzi et al. [15] to remove the coherence estimate bias:

$$z_1 = \frac{1}{M}\sum_{i=1}^{M}\gamma_i \underset{H_1}{\overset{H_0}{\gtrless}} T_1 \tag{V.1}$$

where H_0 is a realization of the null hypothesis (scene changes of interest absent) and H_1 is the alternative hypothesis (scene changes of interest present). To make a decision, the statistic z_1 is compared to a threshold T_1.

V.2.2 Ordered Statistic (OS) detector

The OS detector was initially proposed to deal with impulsive interference [50]. The aim of using the OS detector is to reject some samples with high coherence value over a M-pixel local area. The OS can be used to detect changes by evaluating the following statistic:

$$z_2 = \gamma'_{n_{os}} \underset{H_1}{\overset{H_0}{\gtrless}} T_2 \tag{V.2}$$

where $\gamma'_1 \leq \gamma'_2 \cdots \leq \gamma'_M$ are the ordered sample coherence values over a M-pixel local area and n_{os} is the detector order. In order to make a decision, the statistic z_2 is compared to a threshold T_2. Note that n_{os} determines the detection performance of the statistic z_2.

V.2.3 Censored Mean Level Detector (CMLD)

The CMLD detector is based on the combination of the two statistics z_1 and z_2 [51]:

$$z_3 = \frac{1}{k}\sum_{i=1}^{k} \gamma_i' \underset{H_1}{\overset{H_0}{\gtrless}} T_3 \tag{V.3}$$

where $k \in [1, M[$ is the length of selected and ordered sample coherence over an M-pixel local area. The statistic z_3 is compared to a threshold T_3 to decide whether the pixel under test is made from hypothesis H_0 or H_1. Note that for $k = M$, z_3 is identical to the statistic z_1.

V.2.4 Guard Cell (GC) to improve detection performance

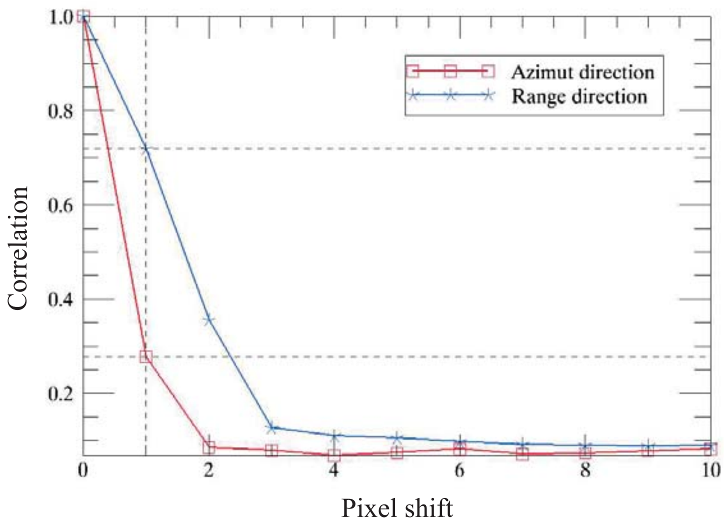

Figure V.2: Spatial correlation of the coherence samples.

In the present work, we have studied the spatial correlation of the coherence data obtained for various CSK data. We have found that for a one pixel shift, the spatial correlation is about 0.28 in the azimuthal direction and 0.72 in the range direction (see Figure V.2).

In order to keep more details in the changed scene, our proposed methods are based on the incorporation of guard cells (GC) only in the range direction. The evaluation of statistics such as z_1, z_2 and z_3 with GC means that the two pixels (cells) directly adjacent to the pixel under test have been ignored (see Figure V.3(b)). In radar detection procedures, GC is mostly used to enhance clutter power estimation [50].

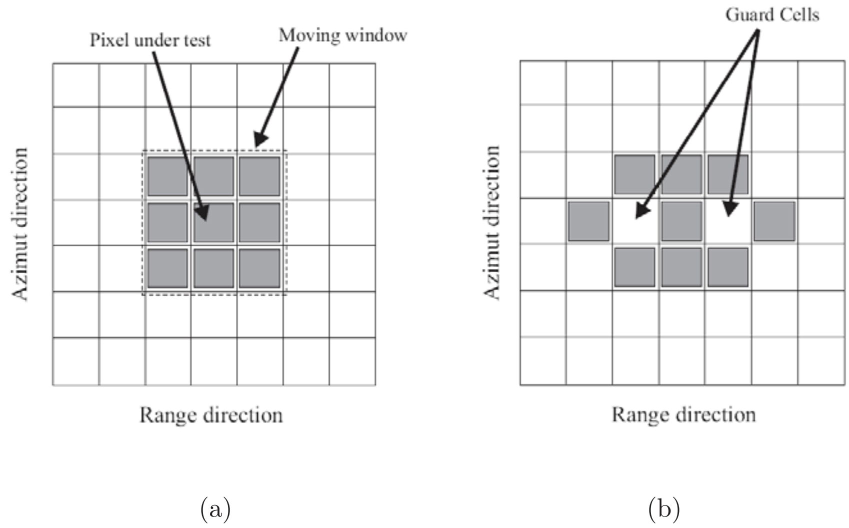

Figure V.3: Moving window configurations. (a) Classical moving window. (b) Moving window with incorporation, in range direction, of two guard cells directly adjacent to the pixel under test.

V.3 Experimental evaluation of the ROC curves

In order to evaluate the quality of a change map independently of the choice of the threshold level, the evolution of the detection probability (P_d) as a function of the false alarm probability (P_{fa}) may be evaluated in the case where a set of constant thresholds are applied to the whole image. These are the so-called Receiver Operating Characteristics (ROC) and the plots $P_d(P_{fa})$ are called ROC curves.
To evaluate experimentally ROC curves, changed and unchanged areas have been selected carefully as ground truth. The simple thresholding of the different statistics (z_1, z_2 and z_3) may be used to distinguish between the changed and unchanged regions in the scene. For a given threshold T, the detection performance may be quantified by evaluating the probability of detection P_d and the corresponding probability of false alarm P_{fa} [5]:

$$P_d = \int_0^T P(\hat{\gamma}|\gamma = \gamma_{changed})d\hat{\gamma} \tag{V.4}$$

$$P_{fa} = \int_0^T P(\hat{\gamma}|\gamma = \gamma_{unchanged})d\hat{\gamma} \tag{V.5}$$

Let us now consider the detection performance of the detectors presented above. The procedure used to estimate experimentally P_d and P_{fa} is based on Equations V.4 and V.5. At first, the selection of the changed and unchanged areas must be done carefully. The selected changed area (inside cultivated parcel in Figure III.12) is composed of N_c

pixels and the selected unchanged area (as indicated in Figure III.12) is composed of N_u pixels. The pixel under test is set in the middle of the moving window which is sliding to scan all coherence data of the selected changed area. To evaluate the actual probability of detection, we perform the test given by Equations V.1, V.2 or V.3. The actual P_d is then given by the ratio of the total number of times the test exceeds the threshold and the total number of pixels in the selected changed area (N_c). Similarly, the probability of false alarm can be evaluated in the same way by using coherence data of the selected unchanged area. The actual P_{fa} is then given by the ratio of the total number of times the test exceeds the threshold and the total number data in the selected unchanged area (N_u). In the present work, $N_c = 110 \times 115$ and $N_u = 61 \times 40$. Figure V.4 shows the probability of false alarm versus threshold T plots obtained for several detectors. For a given P_{fa} value, e.g. $P_{fa} = 5 \times 10^{-3}$ (see the horizontal line), each detector requires distinct threshold value T_i to offer a probability of detection P_d.
A good detection technique is one offering the highest P_d, while using the same values of N, M and P_{fa}.

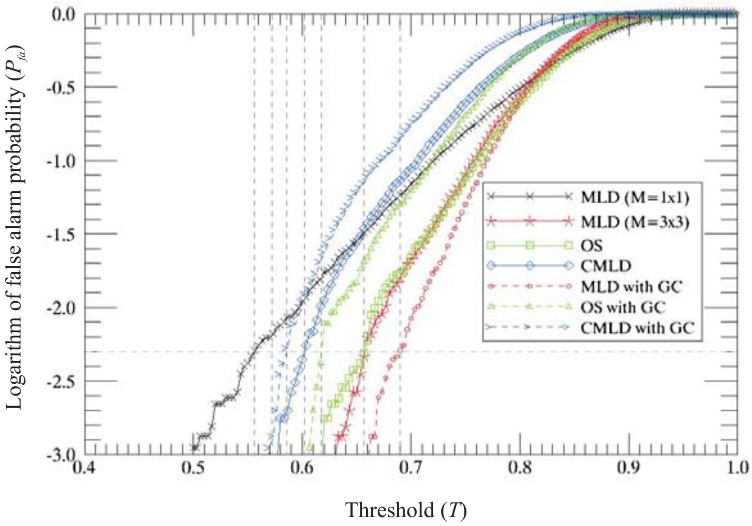

Figure V.4: Experimental probability of false alarm versus threshold T. $M = 3 \times 3$, $n_{os} = 5$ and $k = 5$.

Figure V.5(a) shows the results obtained using MLD statistic with $M = 1 \times 1$ (this corresponds to the case of a simple thresholding operation with $T = 0.556$). This detector offers only $P_d = 0.734$, and the CCD map is unusable. When increasing the window-size M in the local area and for the same P_{fa}, the probability of detection increases. This is presented in Figure V.5(b) with $M = 3 \times 3$ and $T = 0.656$. In this case the MLD gives

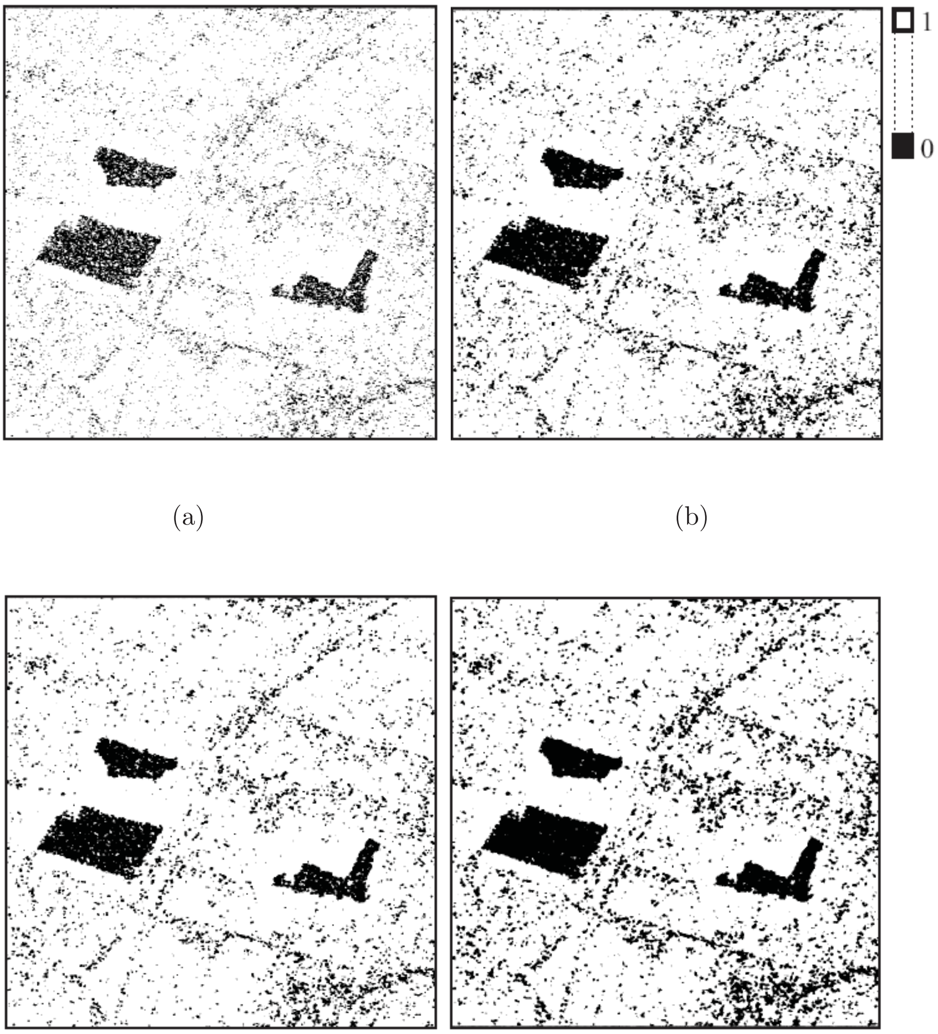

(a) (b)

(c) (d)

Figure V.5: Change detection results for $P_{fa} = 5 \times 10^{-3}$. (a) MLD change map with $M = 1 \times 1$, $T = 0.556$, and $P_d = 0.734$. (b) MLD change map with $M = 3 \times 3$, $T = 0.656$, and $P_d = 0.958$. (c) CMLD change map with $M = 3 \times 3$, $T = 0.603$, $k = 5$, and $P_d = 0.968$. (d) CMLD (with GC)change map for $M = 3 \times 3$, $T = 0.587$, $k = 5$, and $P_d = 0.994$.

$P_d = 0.958$. The increase of the probability of detection from Figures V.5(a) to V.5(b) is clearly noticeable. These results match those obtained in [15], that is the spatial averaging of coherence samples improves the estimation of coherence, especially of low values.
Figure V.5(c) shows the CMLD change map obtained with the following parameter values: $M = 3 \times 3$, $k = 5$ and $T = 0.603$. This detector provides $P_d = 0.968$, which is a value larger than the ones obtained by the MLD and the OS detectors. Hence, the CMLD offers

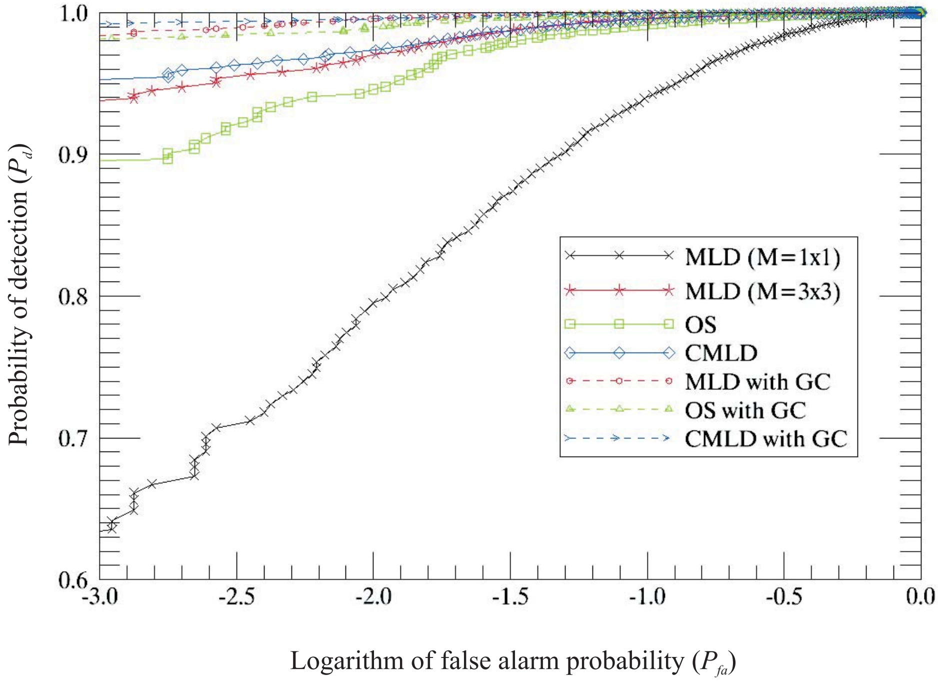

Figure V.6: Experimental ROC curves corresponding to coherence of Figure III.12. $M = 3 \times 3$, $n_{os} = 5$ and $k = 5$.

the best performance. As shown in Figure V.5(d), the use of GC permits an additional change detection improvement. In order to assess the validity of the studied detectors, the detection performance is evaluated by computing the associated ROC curves, which indicate, for a given detection threshold T, the probability P_d of detecting a changed pixel and the corresponding probability P_{fa} of false alarm. The experimental detection performance is shown in Figure V.6 and indicates that CMLD outperforms both MLD and OS. This improvement in the probability of detection is significant for low probability of false alarm ($P_{fa} < 10^{-2}$). For high false alarm rates ($10^{-2} < P_{fa} < 1$), CMLD performs as good as MLD and OS. These results show that the proposed detectors, which are based on the incorporation of GC in the range direction, allow for an increase of nearly 4% in detection probability at $P_{fa} < 10^{-3}$. For more details please refer to [49]. Unfortunately, these change detection improvements are achieved at the expense of a loss of the spatial resolution in the corresponding CCD map.

V.4 Improving CCD performance by using LFF

As shown in Sections V.2 and V.3, a large number of samples N and a large window-size M are needed to detect all the changes, which is obviously at the expense of the spatial details preservation. For that reason, another change information source is recommended to better analyze InSAR coherence.

A careful analysis of the interferometric products, obtained with more than 10 high resolution SAR images, reveals that the interferometric phase of changed areas is characterized by high Local Fringe Frequencies (LFF) values. For an unchanged areas (i.e. without surface activity) the corresponding interferometric phase mainly consists of the topographic information with quite steady values, i.e. low LFF values.

V.4.1 LFF estimation

With medium resolution SAR data, the LFF can be used in InSAR processing at different stages, such as interferogram filtering and phase unwrapping [52]. In mountainous areas, the LFF can be used for the local phase slope compensation during the coherence estimation [48], and also as input to a speckle model in order to reduce the coherence bias [16]. In the present work, we use the LFF as a second information source to better analyze the InSAR coherence in the context of change detection.

Using 2-D notation, the complex InSAR phase can be modeled by a first-order approximation as (for simplicity, noise is neglected) [48]:

$$e^{j\phi(k,l)} = e^{j[2\pi(kf_x+lf_y)]} \tag{V.6}$$

where f_x and f_y are the LFF components respectively in range and azimuth directions.

By assuming that the neighboring pixels have the almost identical terrain height, the LFF components may be obtained by directly differentiating the interferometric phase for measuring the change term of Equation III.28.

From Equation III.25, the interferometric phase $\phi(k,l)$ includes all the frequencies components (f_{xi}, f_{yi}) that exist inside N-pixels local area. However, the measured interferometric phase is heavily influenced by noise and differentiating it will increase the noise. In order to avoid this drawback, the LFF estimation may be realized by the Maximum Likelihood (ML) method [52] or by the MUltiple SIgnal Classification (MUSIC) method [53].

To make use of the LFF, both in range and azimuth directions, we propose the following change statistic:

$$z_4 = \frac{1}{\sqrt{2}M}\sum_{i=1}^{M}\sqrt{f_{xi}^2 + f_{yi}^2} \gtrless T_4 \tag{V.7}$$

where z_4 represents an estimation of the interferometric phase variability inside a M-pixels local area, and T_4 is the detection threshold.

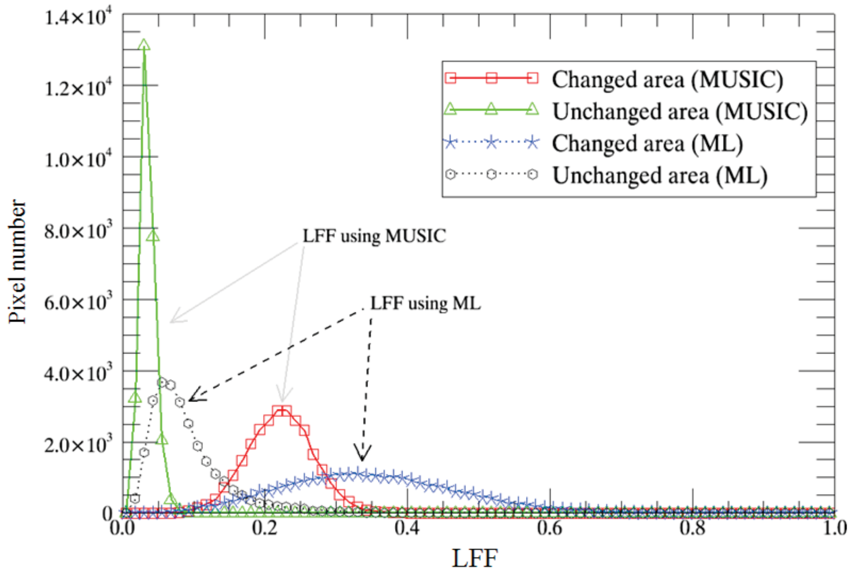

Figure V.7: Histograms of the statistic z_4 in the selected changed and unchanged areas of Figure III.12.

In a CCD application, the topographic information is not the main concern and the number of samples M is selected as small as possible to confer to z_4 the measurement of only ground changes. In the present work, the same window size ($N = M = 3 \times 3$) is selected for both coherence and z_4 estimation to preserve the spatial resolution of the data.
As shown in Figure V.7, that is obtained with the interferogram corresponding to the coherence of Figure III.12, the highly coherent pixels inside the changed area are clearly characterized by high LFF values. Here, the MUSIC method (see appendix A) is used since its provides better LFF histograms separation than the ML method. Note that the estimated LFF, over a small window-size, do not conflict with the real topography particularly when using high resolution SAR data. This is because that LFF components caused by ground changes are much higher than the fringe frequencies due to the topographic variation.
Various SAR image pairs have been used to evaluate LFF histograms for both changed (cultivated parcels, sea area) and unchanged areas. It was observed that the location of the histograms intersection does not change significantly. As a result, it is possible to set the LFF threshold to $T_4 = 0.1$ as shown in Figure V.7.

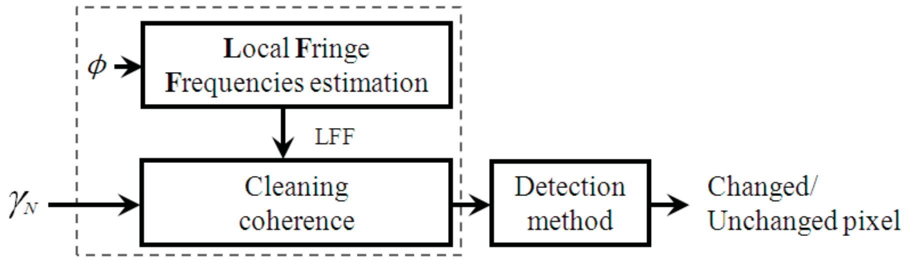

Figure V.8: Scheme of the LFF-based cleaning method.

V.4.2 LFF-based cleaning method

In order to improve the CCD performance, the proposed method uses LFF (statistic z_4) as additional change information to clean the coherence image as presented in Figure V.8. The cleaning coherence step consists in the elimination of only highly coherent pixels, that are considered as aberrant values, inside changed areas. In case of z_4 exceeding the threshold T_4, the corresponding coherence value is set to 0 (changed pixel). Otherwise, in case of low LFF value, the coherence value remains unmodified. Finally, the cleaned coherence is followed by the MLD detector for further detection performance improvement. Figure V.9 depicts the ROC curves evaluated for several values of M. The ROC curve corresponding to $N = 3 \times 3$ and $M = 1$ offers the worst performances. Increasing the number N of samples improves the detection performances. However, it also causes the loss of subtle changes in the coherence image. Substantial improvements may be obtained simply by space-averaging the coherence when using a window-size $M = 3 \times 3$. The LFF-based cleaning method offers a further improvement of about 6% of the detection probability when the false alarm rate is set to $P_{fa} = 10^{-3}$. The proposed method is tested over agricultural fields, with cultivated parcels, and the CCD results are presented in Figure V.10. It can be noticed that the result of simple thresholding method ($M = 1$) of the coherence, see Figure V.10(a), is not usable ($P_d = 0.64$) due to the presence of a large number of highly coherent pixels inside the changed areas. An enhancement of the result is achieved by space-averaging coherence, see Figure V.10(b), by using a window of size $M = 3 \times 3$. In this case, the detection probability improves to $P_d = 0.94$ but remains insufficient. The best result is obtained with the proposed method, as presented in Figure V.10(c), with a detection probability $P_d = 0.99$. In this case, the highly coherent pixels inside changed areas are mostly reduced (detection of almost all changes). The zoom of the changed area, as presented in Figure V.10(d), clearly indicates that the proposed

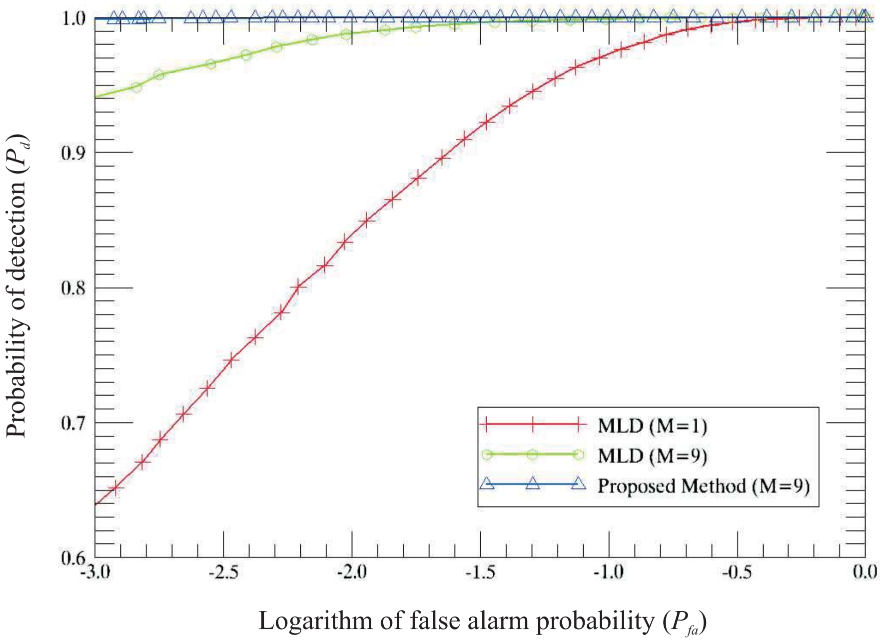

Figure V.9: Experimental ROC curves of the LFF-based cleaning method. Number of samples $N = 3 \times 3$.

method outperform the existing method MLD. The method has been successfully tested on another CSK image pair. The results show that the method also works in steep terrain. The limitation of the method can be noted in some situations where the phase contribution related to the topography is confined inside a window-size of 3×3. The advantage of the proposed method is that it allows an enhancement of about 6% in detection probability with respect to the coherence space-averaging method. In addition, this improvement is achieved by using only a small window size ($N = 3 \times 3$ and $M = 3 \times 3$) to preserve the detection of subtle changes.

V.4.3 LFF-based adaptive method

The LFF-based cleaning method that eliminate aberrant values of the biased coherence offers significant detection performance improvements but some isolated coherent targets are also characterised by high LFF values and then cleaned. This method offers significant detection performance improvement in cropped areas, surface water, but remains limited for activity monitoring within e.g. harbour environment where unmoved targets (i.e. vehicle, container) are also characterised by high LFF values.

Here, we propose an adaptive method for the coherence estimation based on the use of

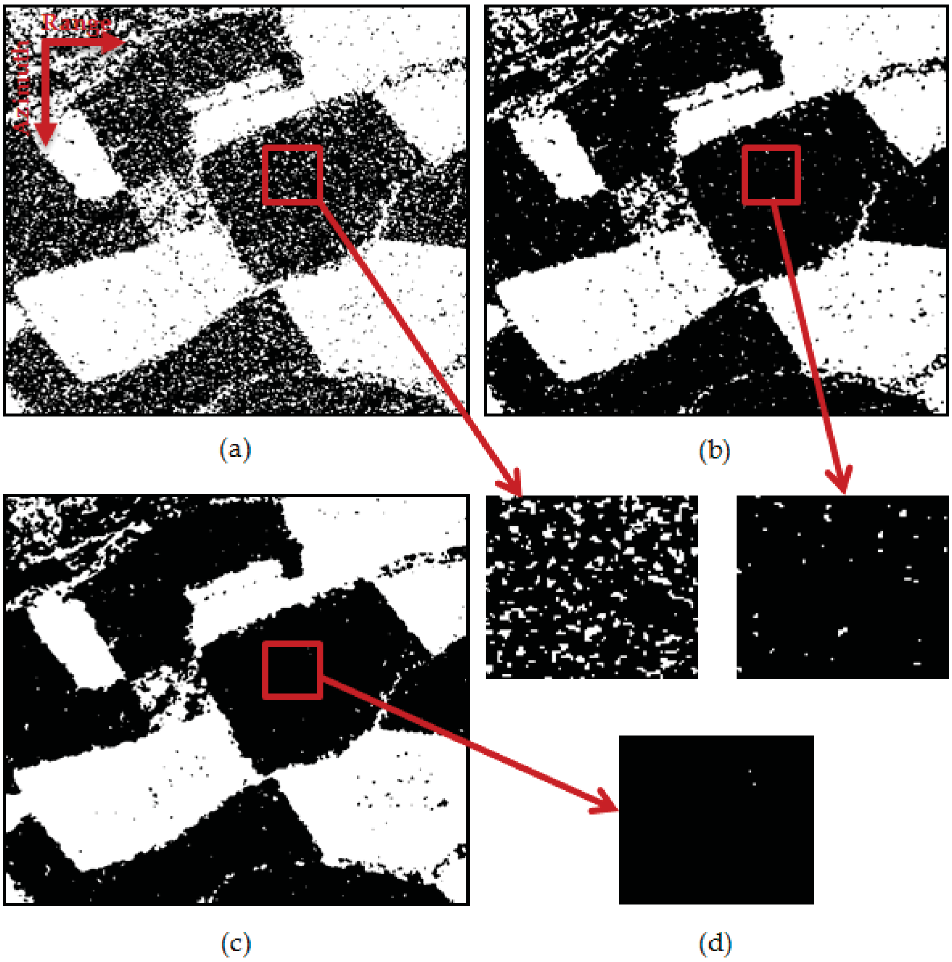

Figure V.10: CCD results for $N = 3 \times 3$ and $P_{fa} = 10^{-3}$. (a) MLD change map with $M = 1$ and $P_d = 0.64$. (b) MLD change map with $M = 3 \times 3$ and $P_d = 0.94$. (c) Change map with the LFF-based cleaning method, $M = 3 \times 3$ and $P_d = 0.99$. (d) Zoom on a cultivated parcel.

LFF to select the appropriate number of samples N. As depicted in Figure V.11, the proposed method uses the LFF information to select the appropriate number of samples N_i. The coherence of the pixel (i, j) is estimated using the number of samples N given by

$$\begin{cases} N = N_1 = 3 \times 3 & \text{if } \; z_4 \leq T_4 \\ N = N_2 = 5 \times 5 & \text{otherwise.} \end{cases} \tag{V.8}$$

The method uses a large value of samples (N_2) in changed areas to reduce the coherence bias and a small value of samples (N_1) is used in unchanged area to preserve the detection of small size changes.

Figure. V.12 depicts the ROC curves evaluated for different values of N. We note that the

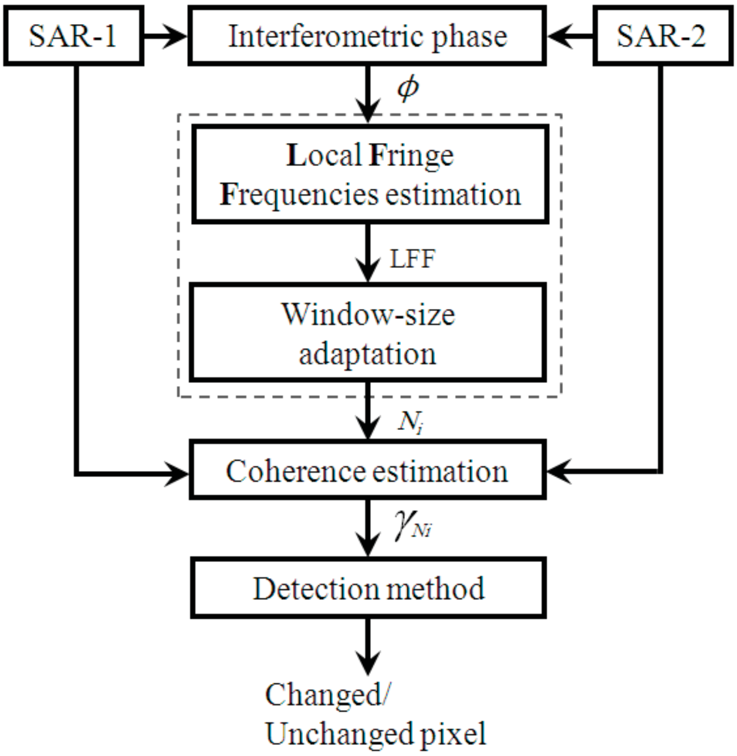

Figure V.11: Scheme of the LFF-based adaptive method.

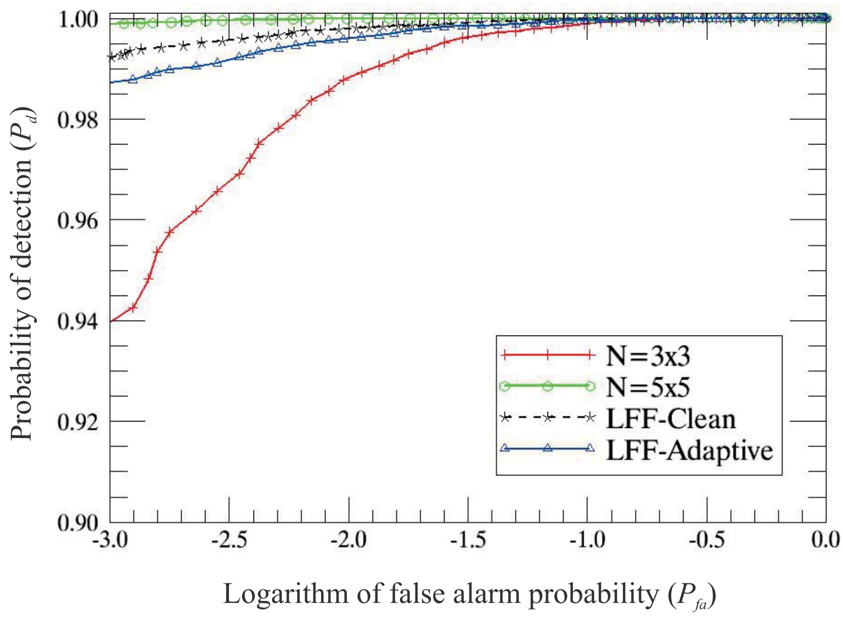

Figure V.12: Experimental ROC curves of the two LFF-based methods.

use of adaptive N approaches the performance obtained by the use of fixed-size window of $N_2 = 5 \times 5$, although the adaptive method uses the two windows size ($N_1 = 3 \times 3$ and $N_2 = 5 \times 5$) with the same rate. We note that the LFF-based adaptive method allows

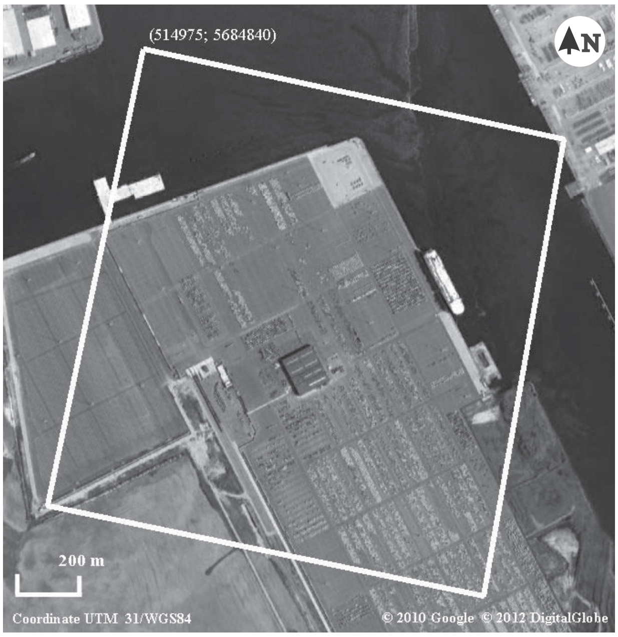

Figure V.13: Optical image from Google Earth of the test site. The rectangle indicates the area of interest corresponding to the SAR image sub-chip size of 1000 × 1000 pixels.

detection improvement of 5 % with respect to the use of a fixed-size window of $N_1 = 3 \times 3$. The LFF-based adaptive method provides less detection performance (of about 1 %) with respect to the LFF-based cleaning method, but offers the great advantage of preserving the small coherent targets. The same detection improvement are also obtained for other well selected changed and unchanged areas.

To assess the validity of the proposed method, a pair of CSK images acquired over Zeebrugge harbour have been selected. Figure V.13 shows the geographical area of the test zone in Zeebrugge harbour. The imaged zone (indicated by the rectangle) consists of a dock for cars and surrounded by the sea (upper part). Figure V.14 shows the coherence map of the imaged area obtained with CSK acquisitions of 15 and 19 June, 2011. Light-colored pixels represents values of coherence near 1, while dark pixels represent values near 0. On the dock, areas with high coherence correspond to the absence of activity (e.g unmoved vehicles in Figure V.14, 1). Places with low coherence corresponding to displaced vehicles between the two acquisitions dates, are located e.g. in Figure V.14, 2. A typical area with various changes is indicated in Figure V.14, 3 and enlarged in Figure V.15. Figure V.15 compares two SAR intensity images (a-b) of the dock area and the CCD results obtained with fixed-size window of $N = 3 \times 3$ in Figure V.15 (c) and with the proposed method in Figure V.15 (d). As in Figure V.8, a space-averaged coherence window

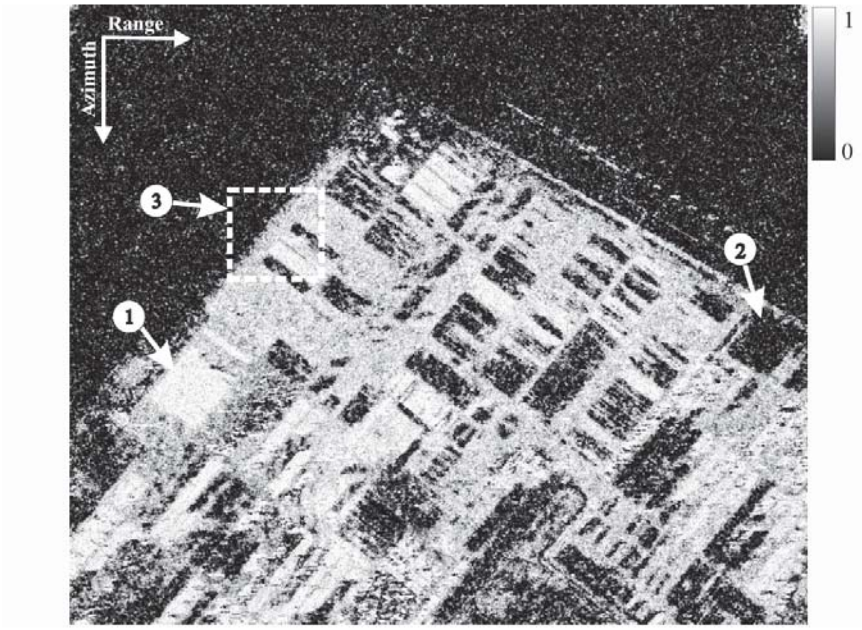

Figure V.14: Coherence map of the Zeebrugge harbour. Sub-set size of 1000×1000 pixels, and $N = 3 \times 3$. COSMO-SkyMed^{TM} Product-ASI [2011] processed under license from ASI-Agenzia Spaziale Italiana.

of $M = 3 \times 3$ is used for further coherence bias reduction. The CCD maps are obtained using detection thresholds (T) that correspond to the same false alarm value $P_{fa} = 10^{-3}$ as in Figure V.12. In Figure V.15 (c), the use of fixed-size window of $N_1 = 3 \times 3$ reveals various changes (black colored pixels) but in the changed areas, like in the sea, some pixels are still classified unchanged (white colored pixels). This missed detection, which is due to the high coherence bias that affects particularly the low coherence areas [49], complicates the CCD map interpretation. In Figure V.15 (d), the changes related to sea area and to the moved vehicles as indicated in Figure V.15 (a-b), 3 are well detected. The adaptive method detects also the subtle changes and achieves the results obtained with the fixed-size window of $N_1 = 3 \times 3$ as indicated in Figure V.15 (a-b), 2. An enhancement of the change detection is then achieved, when compared to the use of the fixed-size window $N_1 = 3 \times 3$, and the coherent pixels inside the sea area are classified as changed.

The CCD results are in agreement with the ROC curves of Figure V.12. The CCD map corresponding to the use of large window size $N_2 = 5 \times 5$ offers a slight change detection improvement with respect to the proposed method. Nevertheless, the use of a large fixed-size window is inappropriate as it presents the inconvenience of loosing the detection of small changes and also of cleaning the small coherent targets confined inside changed areas. For example, the unmoved vehicles surrounded by changes that are indicated in

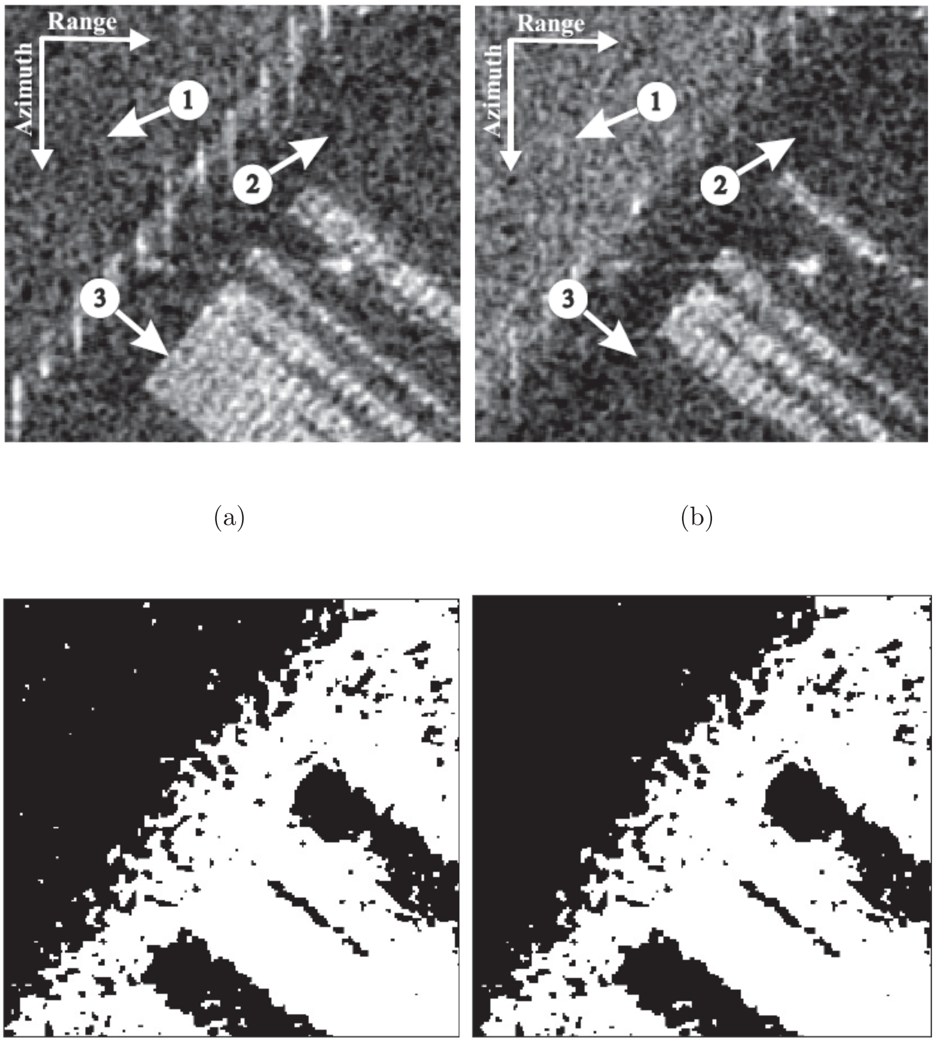

(a) (b)

(c) (d)

Figure V.15: SAR intensity images and CCD results. (a) SAR intensity image of 15 June, 2011. (b) SAR intensity image of 19 June, 2011. (c) CCD map obtained with fixed-size window of $N_1 = 3 \times 3$ samples. (d) CCD map obtained with the adaptive method.

Figure V.16, 1 and 2 are lost when using $N_2 = 5 \times 5$ while they are still detectable with the two other methods ($N_1 = 3 \times 3$, N adaptive).

V.5 Application for earthquakes damages assessment

On 04-Sep-2010 (local time), the Canterbury region in New Zealand (NZ) was shaken by a Mw=7.1 earthquake, and then by series of aftershocks [54]. Two months later, in the frame of the project "SIstema di osservazione spaziale per la Gestione del RIschio

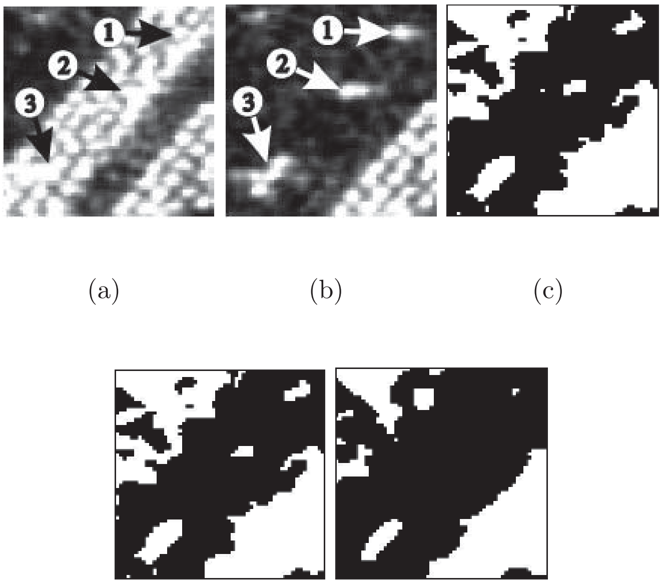

(a) (b) (c)

(d) (e)

Figure V.16: Zoom on unmoved vehicles surrounded by surface changes. (a) SAR image intensity of 15 June, 2011. (b) SAR image intensity of 19 June, 2011. (c) CCD map obtained with fixed-size window of $N_1 = 3 \times 3$ samples. (d) CCD map obtained with the proposed adaptive method. (e) CCD map obtained with fixed-size window of $N_2 = 5 \times 5$ samples. Sub-chip size of 70×70 pixels. The vehicles 1, 2 and 3 in (b) are unmoved between the two dates.

Sismico" (SIGRIS), the Italian Space Agency (ASI) monitored the city of Christchurch with CSK images because aftershocks were expected to take place. Indeed, two deadly events hit the town the 22-Feb-11 - local time - (Mw=6.2) and the 13-Jun-11 (Mw = 5.3 and Mw = 6.0). Widespread damages and soil liquefaction occurred. ALOS, Envisat, and CSK differential interferograms revealed the global dislocation patterns [55].
At local scale, owing to the high resolution of 2.3 m and the X-Band frequency, CSK data revealed confined effects affecting decameters to kilometers wide zone. There, the coherence level remained high, i.e. the relative position between ground scatterers and their orientations was unchanged before and after the quake. These unexpected observations raised questions, especially in areas of extreme shaking (vertical acceleration of around 2 g, and horizontal acceleration of 0.8 g [56]).

In this work, we are interested by the use of improved (enhanced) coherence image to map correctly the boundaries of these zones. The area of interest is essentially covered

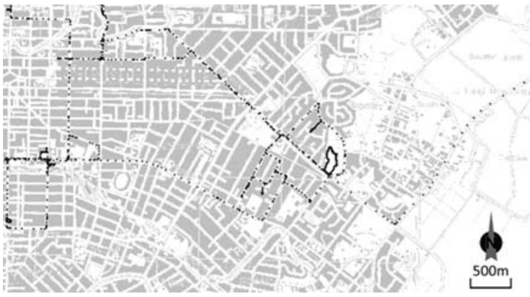

(a)

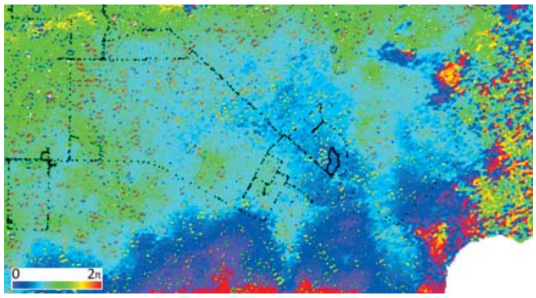

(b)

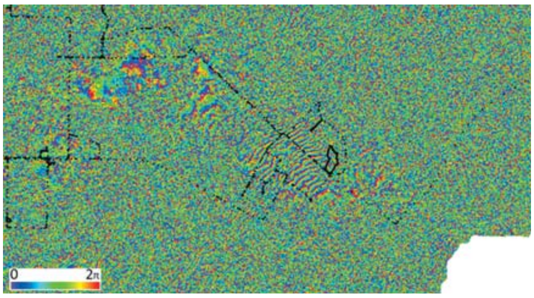

(c)

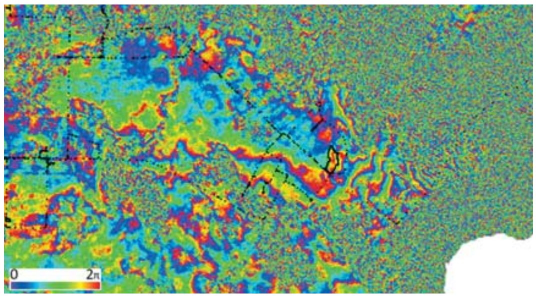

(d)

Figure V.17: (a) Linwood Avenue and its neighborhood. Black dots correspond to GPS track of the field survey carried out in April 2011. (c) Seismic waves' absorption sites recorded during the 22-Feb-11 aftershock (center and upper left corner). (b) and (d): Comparison with the ground deformations recorded in September 2010 and June 2011 events.

by buildings as shown on Figure V.17(a). The C-band Envisat unwrapped interferogram for the 04-Sep-2010 earthquake is found in Figure V.17(b). It shows a small deformation in Christchurch (practically 2 fringes or 5.6 cm). Figure V.17(c) shows the X-band CSK dislocation pattern in ascending mode of the magnitude 6.3 aftershock that struck Christchurch on 22-Feb-11. It revealed an unidentified active strike fault crossing the city [55]. The earthquake caused a large number of fatalities and widespread damage with the collapse of many buildings and significant disruption of lifelines. The CSK interferogram is particularly noisy in the most affected places because the energy involved generated unprecedented Peak Ground Acceleration (PGA) both horizontally and vertically. At a closer look, the interferogram shows at least a dozen of hectometers to kilometers wide areas with important fringe densities that have been interpreted as zones

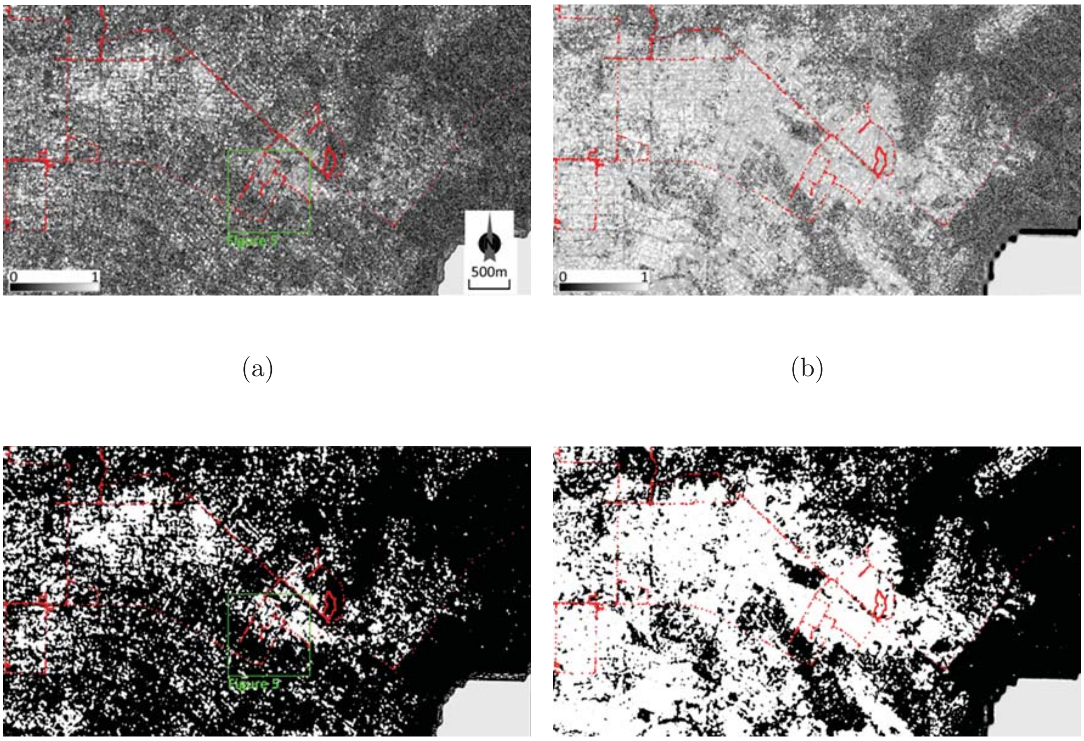

(a) (b)

(c) (d)

Figure V.18: (a) and (b): Coherence images for the 22-Feb-11 and 13-Jun-11 events; (c) and (d): same information but enhanced to define the boundaries of the areas having preserved the coherence (white color) after the tremors. Red dots correspond to GPS tracks recorded in April 2011. Green square represents an area of 1 × 1 km (see Figure V.19) over a representative segment of boundary between high and low coherence.

of high attenuation of seismic waves. Figure V.17(d) shows the X-band CSK dislocation pattern in descending mode of the magnitude 6.3 aftershock that hit on 13-Jun-11. This event produced severe shaking in and around Christchurch, destroying some buildings and causing additional damage to many structures affected by previous earthquakes. The interferogram is far less noisy by comparison with Figure V.17(c). Less energy was released towards the city.

Figure V.18(a) and (b) show coherence images, in greyscale, associated to the interferograms of Figure V.17(c) and (d). GPS tracks are in red color. The important losses observed in Figure V.18(a) are the consequence of the tremors which was characterized by widespread soil liquefaction and the collapse of buildings. Figure V.18(c) and (d) display exactly the same information than in Figure V.18(a) and (b) but the coherence artefacts have been eliminated (see Section V.4.3). Such a post-processing provides far better inputs for data analysis in the GIS and field surveys since the boundaries can be directly extracted.

As an example, a subset of the images (green squares in Figure V.18(a) and (c)) corresponding to an area of 1 km $\times$ 1 km (Figure V.19(a), (b), (d)) had been selected to perform a detailed study of the damages along the limit detected over the interferogram Figure V.17(c) and its associated coherence image Figure V.18(c). This zone was also one of the areas of interest investigated during the field survey in April 2011 (see GPS tracks). Figure V.19(a) is a 1 km^2 subset of a typical urban district crossed by a NW-SE limit between high and low coherence (Figure V.18(c)). The aerials images acquired only two days after the 22-Feb-11 event shows clearly the damages.

In the GIS, one polygons layer corresponding to the damages had been created. When performing manual digitizing, it was possible to feel the transition zone and this understanding became even clearer when superimposing the vector layer to the coherence data (Figure V.18(b) and (d)).

Figure V.19(b) shows the subset of the enhanced coherence image of the February event. Most red polygons are located in low coherence area (black). The (dashed, continuous) green lines come from the ground deformation model realized from GPS data by GNS Science (online). It shows that the area of interest is close to the fault at the origin of the earthquake (lower right corner). In Figure V.19(d), the same polygons are superimposed over the enhanced coherence image of the June aftershock. The energy released was less important than the one of the 22-Feb-11. Therefore, more surfaces preserved the coherence. The most affected zone, however, still continue to correspond to the ones affected four months before.

In this section, we used SAR interferometry technique to detect areas, in Christchurch City, that remain coherent whilst patches around them are incoherent. Enhanced coherence images allow an efficient delineation of their boundaries. Ten centimeters resolution color orthophotography and field data collections confirmed the existence of the sites where the damages are either limited or absent. Damping capabilities seems reproducible from a quake to another. The results suggest a new approach to refine predictions' models for economic losses and propose an alternative method for earthquakes damages assessment in civil engineering purposes.

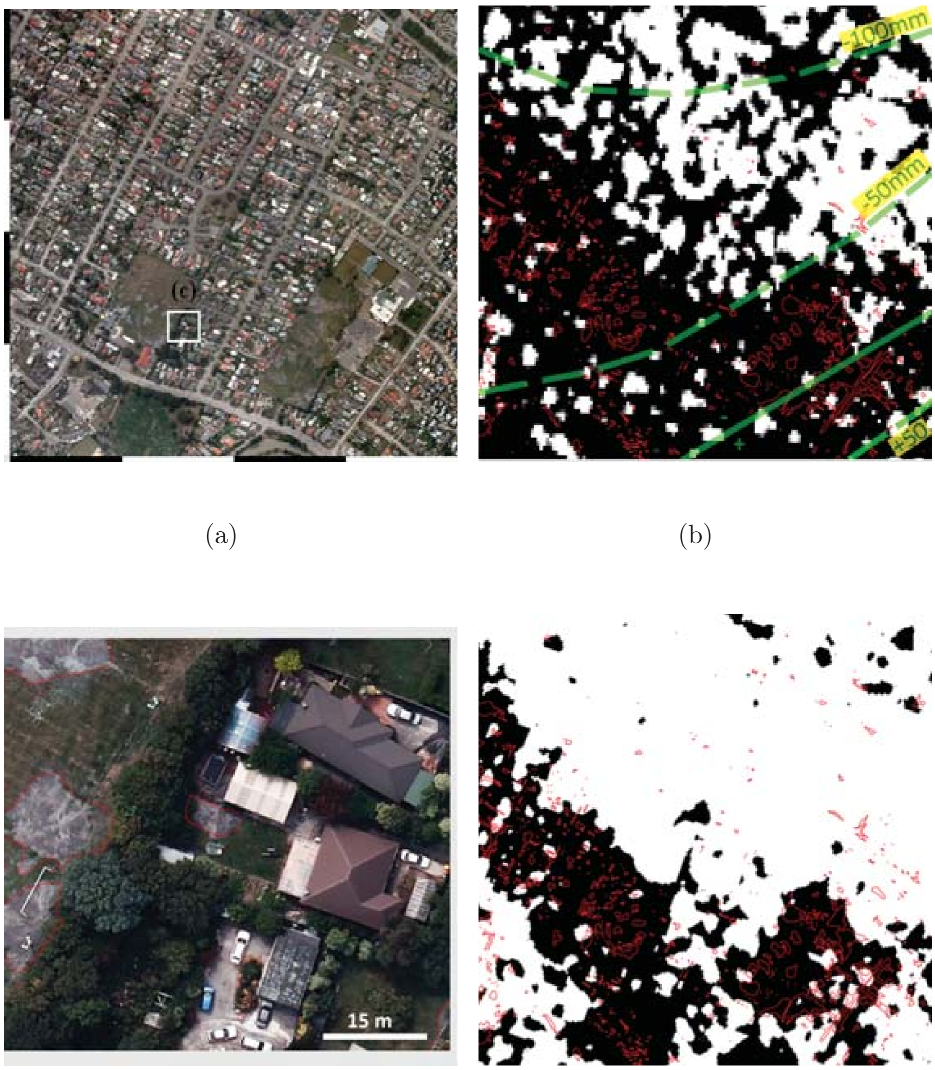

(a) (b)

(c) (d)

Figure V.19: (a) 1 × 1 km color orthophotography at 10 cm resolution (www.koordinates.com, accessed 03-Jun-2013) used to map soil liquefaction, roof and building collapses; (c) detailed view, red line are vectors digitized in the GIS; (b) enhanced coherence image of the 22-Feb-11 event with polygons of damages, essentially liquefaction. Green lines come from GPS deformation map realized by GNS Science; (d) enhanced coherence image of the 13-Jun-11 event and the same polygons than in (b).

V.6 Conclusion

In the present Chapter, methods that improve CCD performance have been investigated. The first part of the chapter has been dedicated to methods using only InSAR coherence information. Three detectors (MLD, OS, and CMLD) have been used to improve change detection performance. Experimental ROC curves have been evaluated and used to quantify the detection performance of the studied methods. The results obtained using high resolution SAR data show that the CMLD outperforms the two other detectors. It has been shown that the studied detectors need large window size to detect all the changes, but this is done at the expense of small change detection. The second part of the chapter has been dedicated to methods using both coherence and LFF information. Two LFF-based methods have been studied and tested. The LFF-based cleaning method, on one hand, that eliminates aberrant values of the biased coherence offers significant detection performance improvements. Nevertheless some isolated coherent targets are also characterized by high LFF values and then cleaned by this method. The adaptive LFF-based method, on the other hand, offers less detection performance improvement compared to the LFF-based cleaning method but with the advantage of preserving isolated coherent targets. The results show that the LFF-based adaptive method presents the best compromise between the detection performance and the preservation of small changes. The application of the enhanced InSAR coherence images to earthquake damage assessment was demonstrated. The obtained results in the present chapter show the advantage of improving coherence map, but it remains difficult to interpret in urban environment. For this, a change classification stage is also needed and will be discussed in the next Chapter VI.

CHAPTER VI

CHANGE CLASSIFICATION

VI.1 Introduction

With the recent arrival of satellite constellations, such as COSMO-SkyMed and TerraSAR-X delivering high-resolution SAR images, it becomes possible to detect surface changes with fine spatial details and with a short revisiting time. This aspect makes the CCD technique ideal for use in military and scientific applications such as border security and environmental monitoring. However, two main difficulties must be overcome in order to improve the analysis of CCD results.

The first difficulty concerns the SAR coherence misestimation. Indeed, the sample coherence estimator is biased, especially for low-coherence values which complicate the InSAR coherence interpretation (see Chapter IV). Various methods that improve the detection performance have been developed and successfully tested in the Chapter V.

The second difficulty of the CCD technique concerns the change identification. As the coherence is affected by several other factors (such as baseline decorrelation and volume decorrelation), the coherence map can reveal changes that are not only due to man-made activities. An area of low-backscatter strength (e.g., water surface, smooth surface, shadows) leads to decorrelation in the coherence image which is not exactly the change of interest. As example, an area of low-backscatter strength (e.g., water surface in Figure V.15 (a, b)1, smooth surface, shadows) leads to decorrelation in the coherence image (e.g. in Figure V.15 (c)-1) which is not truly the change of interest. In addition to the biased coherence estimator, the detection and identification of man-made changes remain difficult, and further investigation is needed.

In this chapter, we present a change classification scheme and the significance of each of the eight resulting classes. The proposed scheme is based on the improved coherence map which is combined with the two corresponding SAR intensity images, in order to identify the types of changes (man-made activity, natural surface decorrelation,...etc.). The two SAR intensity images are not used to detect changes, but only to help the coherence map analysis and interpretation. A set of high-resolution CSK SAR data are selected for the validation process, which concerns different types of environments: an agricultural region in Maymana (Afganistan), a harbour in Zeebrugge (Belgium) and an airport in Goma. A comparative study of the classification results obtained with and without introducing the LFF information is performed. Several examples are presented and discussed to assess the validity of the proposed classification scheme. High-resolution visible images are also used in visual qualitative validation process.

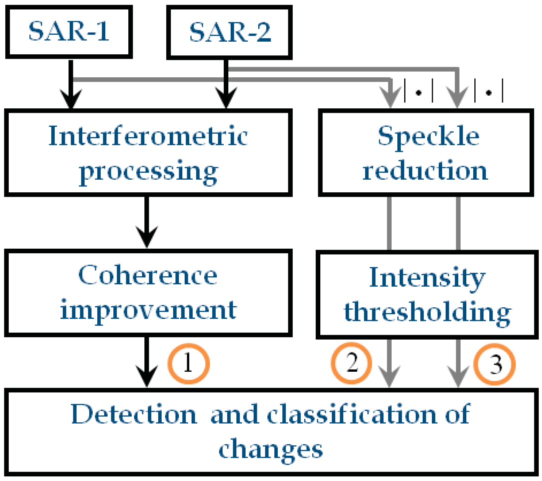

Figure VI.1: Schematic overview of the change detection and classification scheme.

VI.2 Classification scheme

After improvement of the InSAR coherence, the detected changes must be identified as the coherence is affected by several decorrelation sources. For this, we combine the improved coherence map with the two corresponding SAR intensity images, in order to identify all the man-made activities by building a so-called CCD map. Figure VI.1 presents a schematic overview of the processing chain used for the change classification.

Human activities are thus characterized by a low coherence and a high intensity in at least one of the two SAR images. However, any decision based on SAR intensity is hampered by the presence of speckle which increase the number of false alarms. Therefore, a speckle reduction is performed prior to the change classification: a 3×3 Lee filter [57] is applied to SAR intensity images in this work.

The developed classification scheme is quite simple and is based on a combination of the three features, i.e. the improved coherence and the Lee-filtered intensity images. Each of the two SAR intensity images is subdivided into a low (L) and a high (H) value area, with thresholds that are determined from the histograms of the learning set. The learning set consists in two classes: low backscattered area (smooth surface or water surface) and high backscattered area (rough surface). Various SAR images have been used to evaluate intensity histograms for both smooth and rough areas. It was observed that the location of the histograms intersection does not change significantly. As a result, it is possible to set the intensity threshold to $T_I = 0.25$ as shown in Figure VI.2.

The proposed change detection and characterization scheme is a rule-based set of decisions

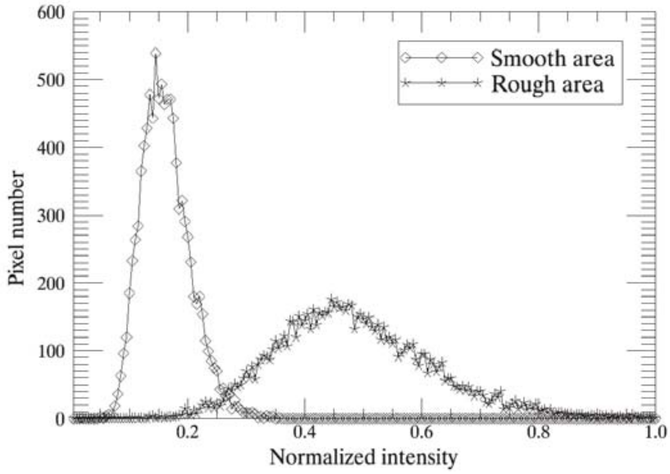

Figure VI.2: Histograms of the learning set.

applied to the thresholded SAR intensity images and to the enhanced coherence map. Dividing each of the three feature sets into two value regions leads to 8 combinations, thus 8 possible classes given by

$$x \in \quad \mathtt{C}_k \qquad \mathtt{if}: \begin{cases} |s_1| \gtrless T_I \\ |s_2| \gtrless T_I \\ \gamma_N \gtrless T_z \end{cases} \tag{VI.1}$$
$$0 \qquad \qquad \mathtt{elsewhere}$$

Table VI.1 presents an overview of the properties of these classes. Classes of interest for change detection and activity monitoring are C2, C3 and C4. Classes C1, C5 and C8 contribute to the overall scene understanding. C6 and C7 represent classes in which the coherence is high but the intensity changes between both images. If this situation occurs, it is due to the fact that the coherence (or intensity) value supersedes the threshold T_I in a region where it shouldn't (tails of the histograms).
It is also possible to divide the coherence into 3 regions; low (L), medium (M) and high (H). This situation would lead to 12 classes that complicate further the CCD map analysis and interpretation. This is the reason why we have opted to begin with the binary thresholding of the coherence, which proves to be sufficient for identification of all man-made changes. In future work, we will analyze the influence of the intermediate (medium) level on the quality of the final result.

Class	Features			Interpretation
	Coherence	SAR-1	SAR-2	
C1	L	L	L	Specular surfaces: water, roads, roofs, shadows
C2	L	L	H	Man-made objects present in SAR-2, not in SAR-1
C3	L	H	L	Man-made objects present in SAR-1, not in SAR-2
C4	L	H	H	Man-made object present in both images but it changed from SAR-1 to SAR-2
C5	H	L	L	Bare soil or low vegetation
C6	H	L	H	Invalid class (problem of intensity thresholding caused by speckle)
C7	H	H	L	Invalid class (problem of intensity thresholding caused by speckle)
C8	H	H	H	Scatterers present in both scenes: fixed structures (e.g. parts of buildings, railways), undisturbed areas

Table VI.1: Overview of the eight classes resulting from the change detection and classification.

VI.3 Overview of the dataset

During the preparation of the thesis, a set of several CSK SAR images were available and 3 image pairs were chosen to make the validation of the proposed classification method. Here, we are interested by three types of environments:

- Agricultural environment in Maymana (Afghanistan).
- Harbor environment in Zeebrugge (Belgium).
- Airport environment in Goma (DRC).

Table VI.2 presents the main characteristics of the used SAR data. As reminder, each image pair was acquired with the same acquisition geometry in order to allow InSAR processing.

Region, Country	Maymana, Afghanistan	Zeebrugge, Belgium	Goma, DRC
Acquisition Dates	1/1 & 1/9/2010	6/15 & 6/19/2011	3/24 & 3/28/2011
Image Size (Rg×Az)	19255×14403	15312×14486	14568×14376
Time Acquisition	01h41 UTC	18h05 UTC	15h50 UTC
Pass	Ascending	Descending	Descending
Incidence Angle	41.5°	28°	26°
Sensor Mode	Spotlight		
Polarisation	HH		
Azimuth Resolution	0.70 m		
Ground Range Resolution	0.66 m	0.57 m	0.73 m
Baseline, Height ambiguity	$B_\perp = 150$ m, $z_{2\pi} = 66$ m	$B_\perp = 22$ m, $z_{2\pi} = 231$ m	$B_\perp = 307$ m, $z_{2\pi} = 15$ m

Table VI.2: Overview of the COSMO-SkyMed SAR images characteristics used in the validation process.

Figure VI.3: Optical image from Google Earth of Maymana (Afghanistan). The red rectangle indicates the test area that corresponds to the available CSK SAR images of 19255×14403 pixels size. © Google Earth 2012. All rights reserved.

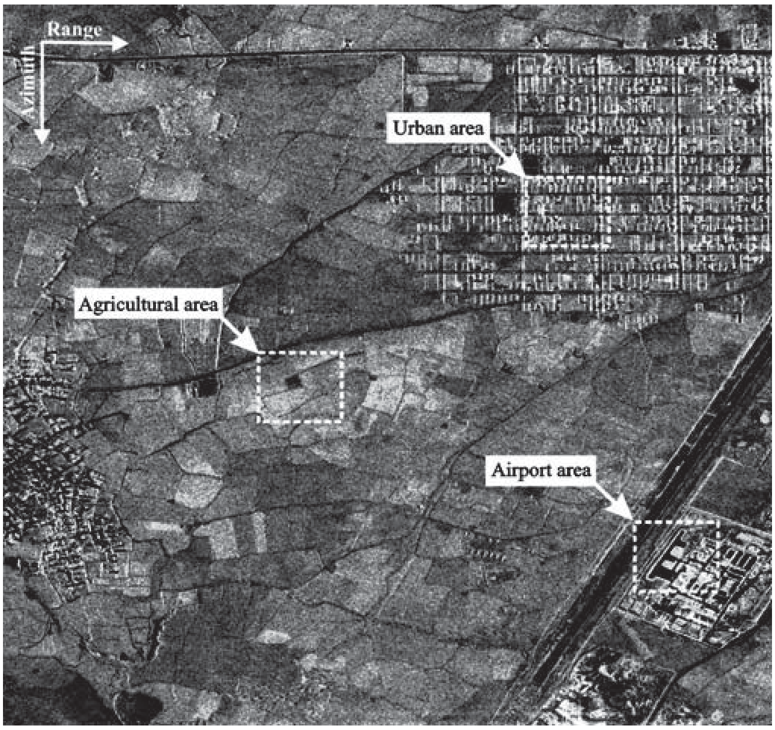

Figure VI.4: CSK SAR intensity image of the Maymana region (Afghanistan), sub-set size of 4000 × 4000 pixels. COSMO-SkyMed^{TM} Product - ASI [2010] processed under license from ASI - Agenzia Spaziale Italiana. All rights reserved.

VI.4 Application in agricultural environment

As shown in Figure. VI.3, the imaged area consists of a plain surrounded by mountains. An important agricultural activity was registered during the acquisition period of 1 to 9 January 2010. Figure VI.4 shows subset of the test area, which is a relatively flat terrain that contains part of airport, agricultural fields and urban area. The coherence map, for the present case study, shows several changed areas corresponding to cultivated parcels with low values of coherence. Indeed, coherence subsets have been geocoded and then projected in Google Earth to perform a comparison with high-resolution visible images. It had been verified that all areas with low values of coherence match perfectly boundaries of the agricultural parcels. In the following sections, classification results related to the different areas (agricultural and urban) as indicated in Figure. VI.4 will be presented and discussed.

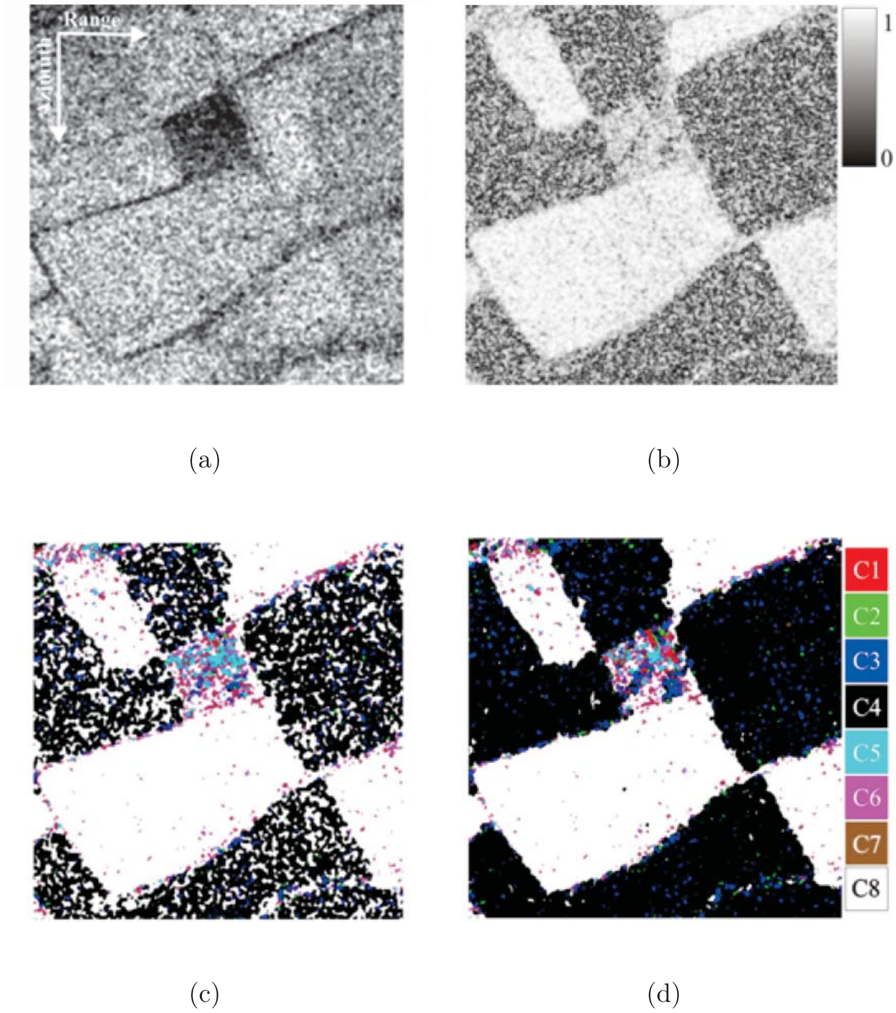

Figure VI.5: Change classification results of the agricultural area in Maymana (Afghanistan), sub-set size of 320 × 320 pixels. (a) CSK SAR image intensity of January 1, 2010. (b) coherence image evaluated by using 3 × 3 pixel spatial estimation window. (c) Change classification result obtained by the classical MLD method. (d) Change classification result obtained by the proposed LFF-based cleaning method.

VI.4.1 Agricultural area

Figure VI.5-(a) shows SAR image intensity corresponding to agricultural fields. As shown in Figure VI.5-(b), the cropped parcels are clearly indicated with low coherence values and the uncultivated parcels preserve the coherence. The change classification results, Figure VI.5-(c), show that the scene is constituted by two dominant classes (C4 and C8). We notice the existence of a large number of coherent pixels (class C8) inside the cultivated fields, which is caused mainly by the coherence bias. Figure VI.5-(d) shows that the use of enhanced coherence map, which is obtained with LFF-based cleaning method, improves the classification results. The changes related to the agricultural activity are almost detected and then classified as C4. By using high resolution optical image, we identify the small field in the center of the scene as a partially dry lake. This complex surface, which appears as a low backscatter surface in Figure VI.5-(a), contains most of the classes C1-C8 as shown in Figures VI.5- (c) and (d).

The agricultural test zone can be considered as an ideal example to demonstrate the importance of the InSAR processing in the classification process, when compared to the intensity-based (incoherent) change detection techniques. Indeed the cultivated fields present nearly the same intensity response in both SAR images and the man-made changes are mainly indicated by only the interferometric phase, and then measured by the coherence.

VI.4.2 Urban area

Figure VI.6-(a) shows SAR image intensity corresponding to urban area. As showed in Figure VI.6-(b), the permanent structures (buildings, boundary walls) are clearly indicated with high coherence. We can also distinguish a large cultivated parcel that is characterized by a low coherence and delimited by walls. The change classification results, Figure VI.6-(c), show that the scene is constituted by two dominant classes (C4 and C8). We notice the existence of a large number of coherent pixels (class C8) inside the cultivated parcel. The roads appear as complex surface with all of the different classes (C1-C8).

Figure VI.6-(d) shows that the use of enhanced coherence map, which is obtained with the LFF-based cleaning method, improves the classification results. The cultivated parcel is classified as C4 and the permanent structures as C8. The roads are represented by only the classes C1-C4, which are the logical results compared to those presented in Figure VI.6-(c).

VI.5 Application in a harbor environment

The geographical location of the test zone that concerns the Zeebrugge harbour is shown in Figure VI.7. During the SAR acquisition period of June 15 to 19, 2011, an important container and vehicle movement was registered, which can be observed easily through the analysis of the SAR intensity images. For the validation of the classification scheme, high

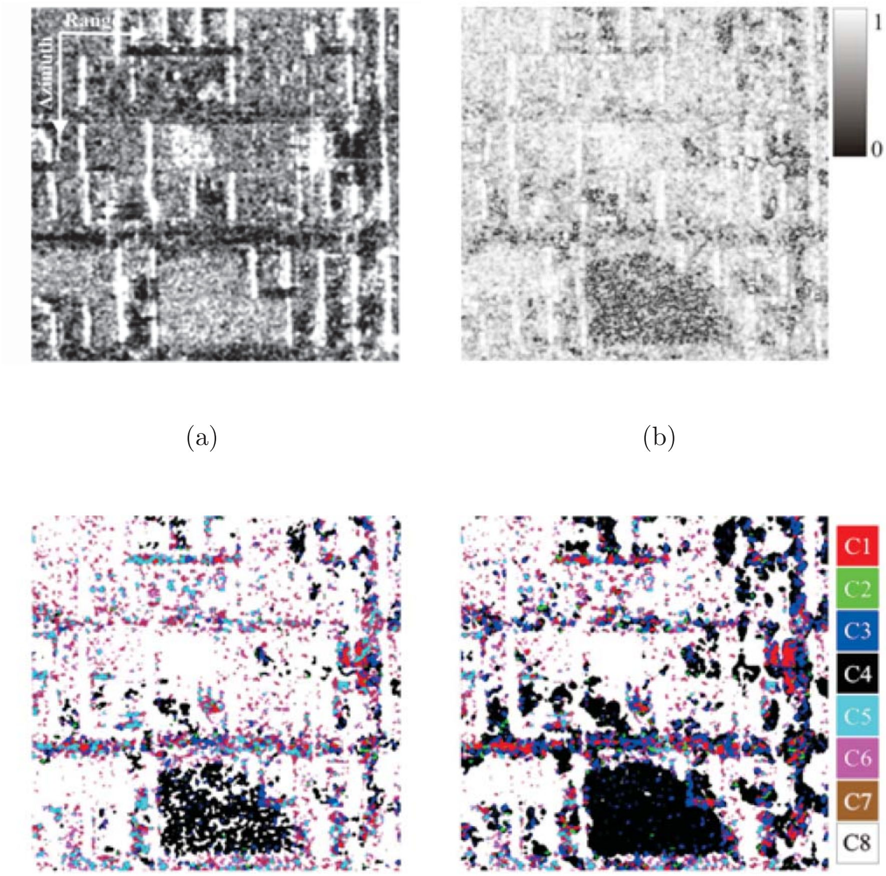

(a) (b)

(c) (d)

Figure VI.6: Change classification results of the urban area in Maymana (Afghanistan), sub-set size of 320 × 320 pixels. (a) CSK SAR image intensity of January 1, 2010. (b) coherence image evaluated by using 3 × 3 pixel spatial estimation window. (c) Change classification result obtained by the classical MLD method. (d) Change classification result obtained by the proposed LFF-based cleaning method.

resolution visible images are used and the SAR intensity images have served as ground truth.

Figure VI.8 shows subset of the test zone, which is a flat terrain that contains part of the port and surface water. In the following sections, classification results related to different areas (sea and container terminal) as indicated in Figure VI.8 will be presented and discussed.

Figure VI.7: Optical image from Google Earth of the Zeebrugge harbor (Belgium). The red rectangle indicates the test area that corresponds to the available CSK SAR images of 15312 × 14486 pixels size.

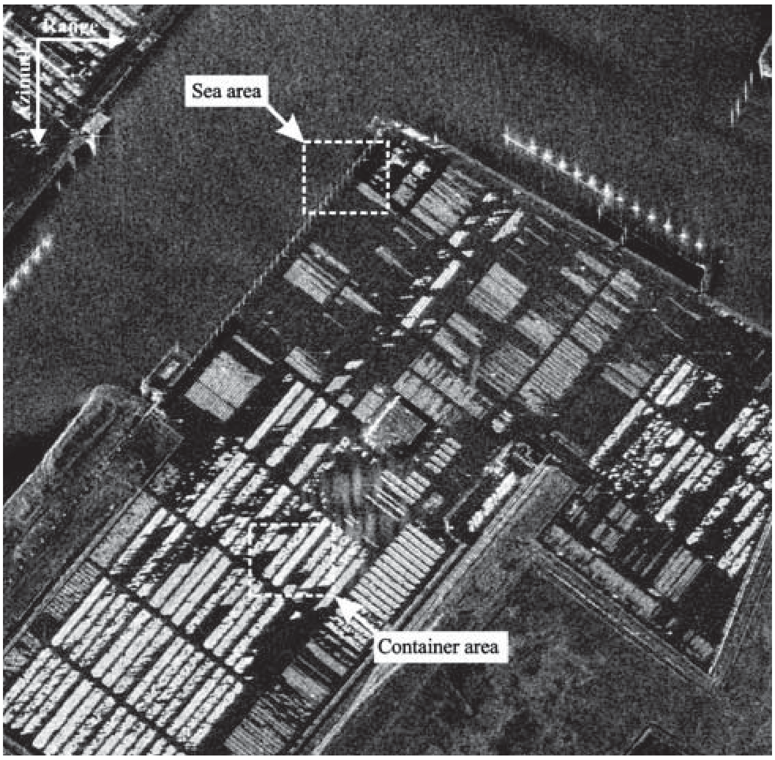

Figure VI.8: CSK SAR intensity image of the Zeebrugge harbor (Belgium), sub-set size of 2000 × 2000 pixels. COSMO-SkyMed^{TM} Product - ASI [2011] processed under license from ASI - Agenzia Spaziale Italiana.

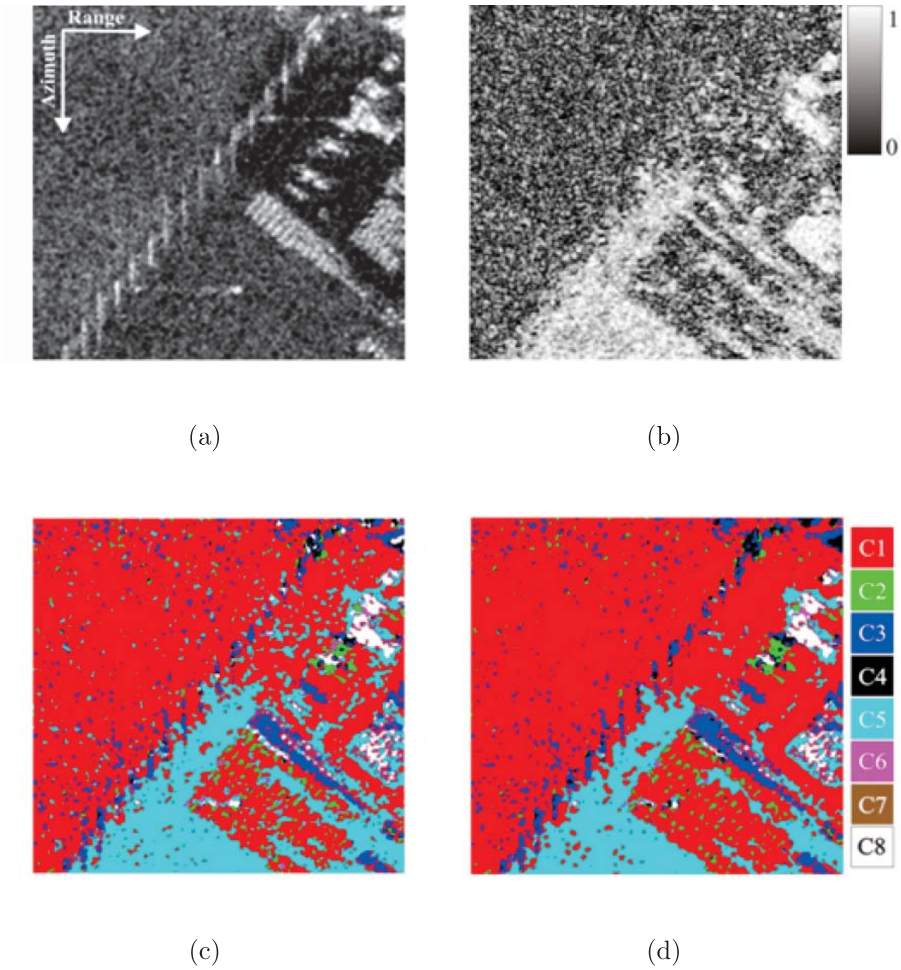

Figure VI.9: Change classification results of the selected sea area in Zeebrugge (Belgium), sub-set size of 300×200 pixels. (a) CSK SAR image intensity of June 15, 2011. (b) coherence image evaluated by using 3×3 pixel spatial estimation window. (c) Change classification result obtained by the classical MLD method. (d) Change classification result obtained by the proposed LFF-based cleaning method.

VI.5.1 Sea area

Figure VI.9-(a) shows SAR intensity image of the selected sea area which consists of dock for vehicles surrounded by the sea (left part). On the dock, Figure VI.9-(b), areas with high coherence correspond to the absence of activity (unmoved vehicles). Places with low coherence correspond mostly to displaced vehicles between the two acquisition dates, which are also visible by the analysis of the two SAR intensity images. The change classification results, Figure VI.9-(c), show that the scene is constituted by three dominant classes (C1, C3 and C5). Unlike the agricultural environment in Figure VI.5, we note the absence of the class C4 or at least not a lot. This is due to the fact that the change in the harbour environment is of class C2 and C3 (objects exist in one image but not in the other). We can also notice in Figure VI.9-(c), that the surface of the dock that is not concerned by the man-made changes is classified into two classes; C1 in the upper part and C5 in the down part of Figure VI.9-(c). With using high resolution optical image, we verify that the surface corresponding to C1 in the dock is more smooth (special soil coating and appears with different color), while the surface corresponding to C5 is the normal rough surface of the dock.

This example shows also the ability of the change classification scheme to discriminate surface roughness. Figure VI.9-(d) shows that the use of the enhanced coherence map, which is obtained with LFF-based cleaning method, improves the classification results. The water surface, which is an incoherent medium, is classified as C1 in Figure VI.9-(d). But we note some pixels of the classes C2 and C3 which are not due to man-made objects but simply due errors in the SAR intensity separation. Indeed, the radiometric response of the water surface depends on whether the sea is calm or not which complicates the separation between low and high backscatter surfaces.

VI.5.2 Container terminal area

Figure VI.10-(a) shows SAR image intensity of the selected container terminal area, in which columns of vehicles with high backscatter are clearly visible. In Figure VI.10-(b), areas with high coherence values correspond to unmoved vehicles, while places with low coherence corresponding to displaced vehicles between the two acquisitions dates. The change classification results in Figure VI.10-(c), show that the scene contains almost all of the classes (C1- C8). Figure VI.10-(c) shows also changes of class C4, which corresponds to vehicles that appear in both SAR images but not the same ones. This example shows again the ability of CCD technique to detect type of changes, which is not possible with image intensity-based techniques. Figure VI.10-(d) shows that the use of the enhanced coherence map (obtained with LFF-based cleaning method) improves the classification results, but with an inconvenient of cleaning some coherent targets surrounded by changes. Indeed, some isolated unmoved vehicles as in Figure VI.10-(a) 1 and 2, which are characterized by high coherence and classified as C8 in Figure VI.10-(c) are cleaned by the LFF-based cleaning method and then classified as C4 instead of C8.

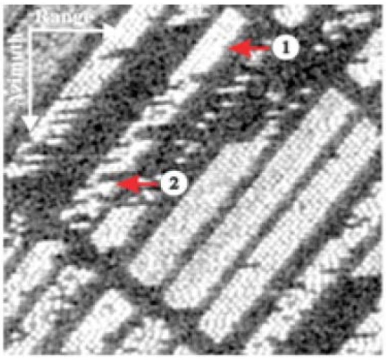

(a)

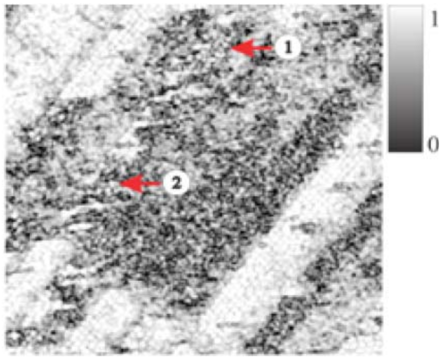

(b)

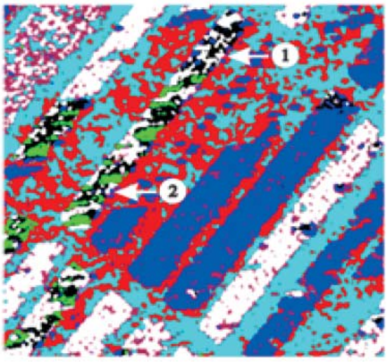

(c)

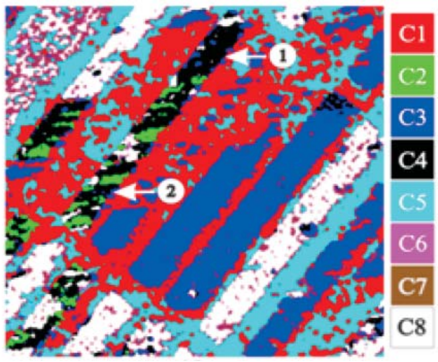

(d)

Figure VI.10: Change classification results of the container terminal area in Zeebrugge (Belgium), sub-set size of 300×300 pixels. (a) CSK SAR image intensity of June 15, 2011. (b) coherence image evaluated by using 3×3 pixel spatial estimation window. (c) Change classification result obtained by the classical MLD method. (d) Change classification result obtained by the proposed LFF-based cleaning method.

VI.6 LFF-based cleaning method versus LFF-based adaptive method

As indicated previously, the LFF-based cleaning method offers significant detection performance improvements in cropped areas, in surface water and in large changed areas, but remains limited for activity monitoring within a harbour environment where unmoved vehicles, which are characterised by high LFF values, are also cleaned. In this situation, an alternative consists in the use of the LFF-based adaptive method which offers slightly lower detection performances but with the advantage of non-elimination of the highly

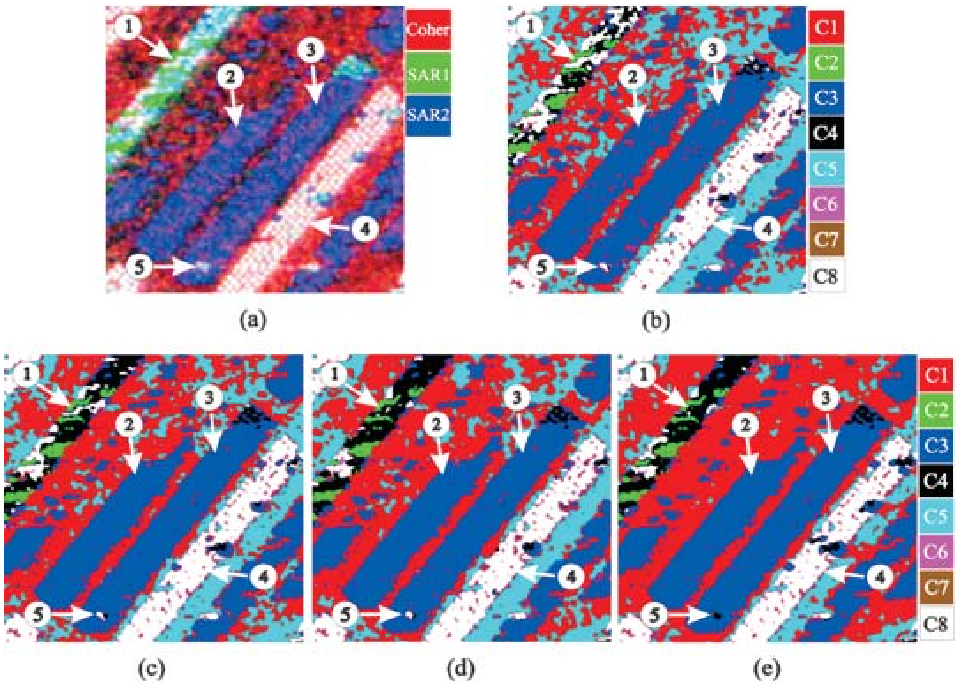

Figure VI.11: Change classification results. (a) RGB color composition of test area, Red: coherence image, Green: CSK SAR image intensity of June 15, 2011 and Blue: CSK SAR image intensity of June 19, 2011. (b) Fixed window of 3 × 3 samples. (c) LFF-based adaptive method. (d) LFF-based cleaning method. (e) Fixed window of 5 × 5 samples. Sub-set size of 220 × 220 pixels.

coherent targets. As depicted in Figure VI.11-(a), the test site is composed mostly of:

1. area with both moved and unmoved vehicles as indicated by (1);
2. areas of only moved vehicles that are indicated by (2 and 3);
3. area of unmoved vehicles as indicated by (4).

The LFF-based adaptive method in Figure VI.11-(c) offers change classification results slightly similar to those obtained by the LFF-based cleaning method in Figure VI.11-(d) and also close to those obtained by a large fixed window size of 5 × 5 samples in Figure VI.11-(e). The advantage of the LFF-based adaptive method is the preservation of subtle details. As showed in Figure VI.11-(e), the use of a fixed large window size of 5 × 5 is inappropriate and presents the following disadvantages: the loss of subtle changes, an increased size of the detected changes (4) and the cleaning of small coherent targets surrounded by changes (5). Figure VI.12 makes a zoom on unmoved vehicles surrounded by changes. The LFF-based adaptive method detect all the vehicles designed

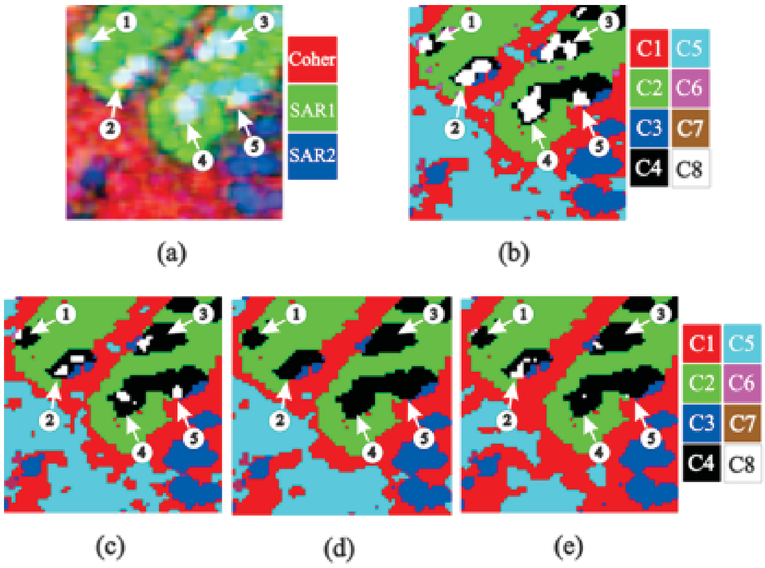

Figure VI.12: Change classification results: Zoom on unmoved vehicles. (a) RGB color composition of test area, Red: coherence image, Green : CSK SAR image intensity of June 15, 2011 and Blue: CSK SAR image intensity of June 19, 2011. (b) Fixed window of 3×3 samples. (c) LFF-based adaptive method. (d) LFF-based cleaning method. (e) Fixed window of 5×5 samples. Sub-set size of 60×60 pixels.

by arrows 1, 2,$\cdots$, 5 in Figure VI.12-(c) while the LFF-based cleaning method looses all the vehicles in Figure VI.12-(d), and by using large a window size only vehicles 2 and 3 in Figure VI.12-(e) are detected.

VI.7 Application to monitoring man-made changes

The results presented in this section are obtained with CSK data in X-band, horizontally polarized in spot-light mode. The test site, shown in Figure VI.14, concerns the Goma airport.

The area of interest, shown in Figure VI.14-(a), concerns part of the Goma airport. The airport was under extension, and an important earthmoving activity was registered during the acquisition period of March 24 to 28, 2011. The scene concerns a wide open field surrounded by buildings and urban areas. The area occupied by the company in charge of the airport extension, as indicated by Figure VI.14(a)-1, is surrounded by roads where earth mover vehicles are clearly visible. The man-made activities are mainly concentrated in the dike as indicated in Figure VI.14(a)-2 and in area pointed by Figure VI.14(a)-3. The dike causes a distortion (shadow) in the SAR image as indicated in Figure VI.14(b)-2.

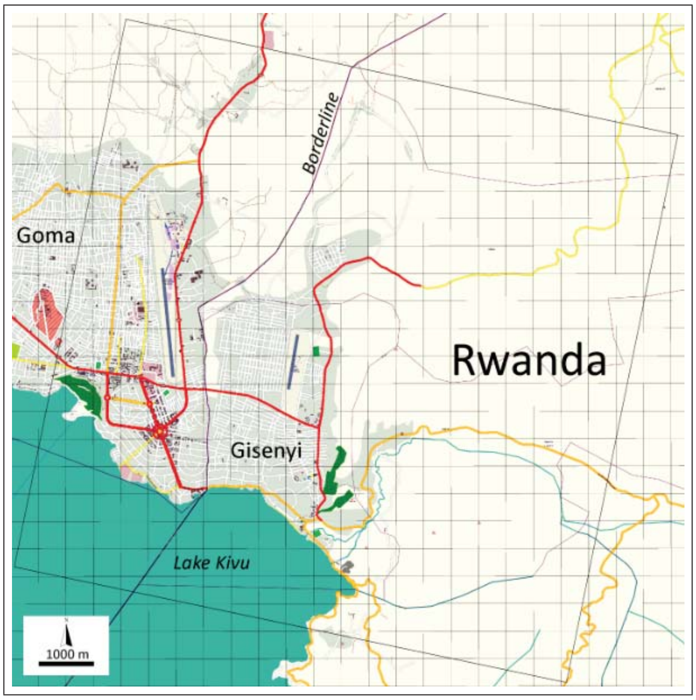

Figure VI.13: Geographical location of the test site in Goma, in the Democratic Republic of Congo, that is characterized by a flat topography. The rectangle indicates the imaged scene corresponding to the used CSK SAR images of 14568 × 14376 pixels.

The airport runway, showed in Figure VI.14(a)-4, is characterized by a low backscatter power as in Figure VI.14(b)-4. In the urban area, left side of Figure VI.14-(b), we can observe that the roofs are also characterized by a low backscatters.

Figure VI.14-(c) shows the enhanced coherence map (LFF-based adaptive method) of the imaged area obtained by using the CSK acquisitions of March 24 and 28, 2011. Areas with high coherence correspond to the absence of surface activity. Places with low coherence, corresponding to the disturbed areas between the two acquisitions dates, are located e.g. in Figure VI.14(c)-1, 2 and 3. We can see that all roads leading to the holding area of Figure VI.14(c)-1 lost the coherence, which is obviously caused by the earth mover vehicles movement. The analysis and interpretation of the coherence map becomes complicated in the presence of man-made structures. Indeed, for instance, the big building in Figure VI.14(a)-1, that is characterized by low coherence in Figure VI.14(c)-1 is not exactly the change of interest.

The change classification results corresponding to the period of 24 and 28 March, 2011 are depicted in Figure VI.14-(d). Only the changes C2, C3 and C4 are of interest, and the other classes help the scene analysis. Besides the advantages of the coherence to detect

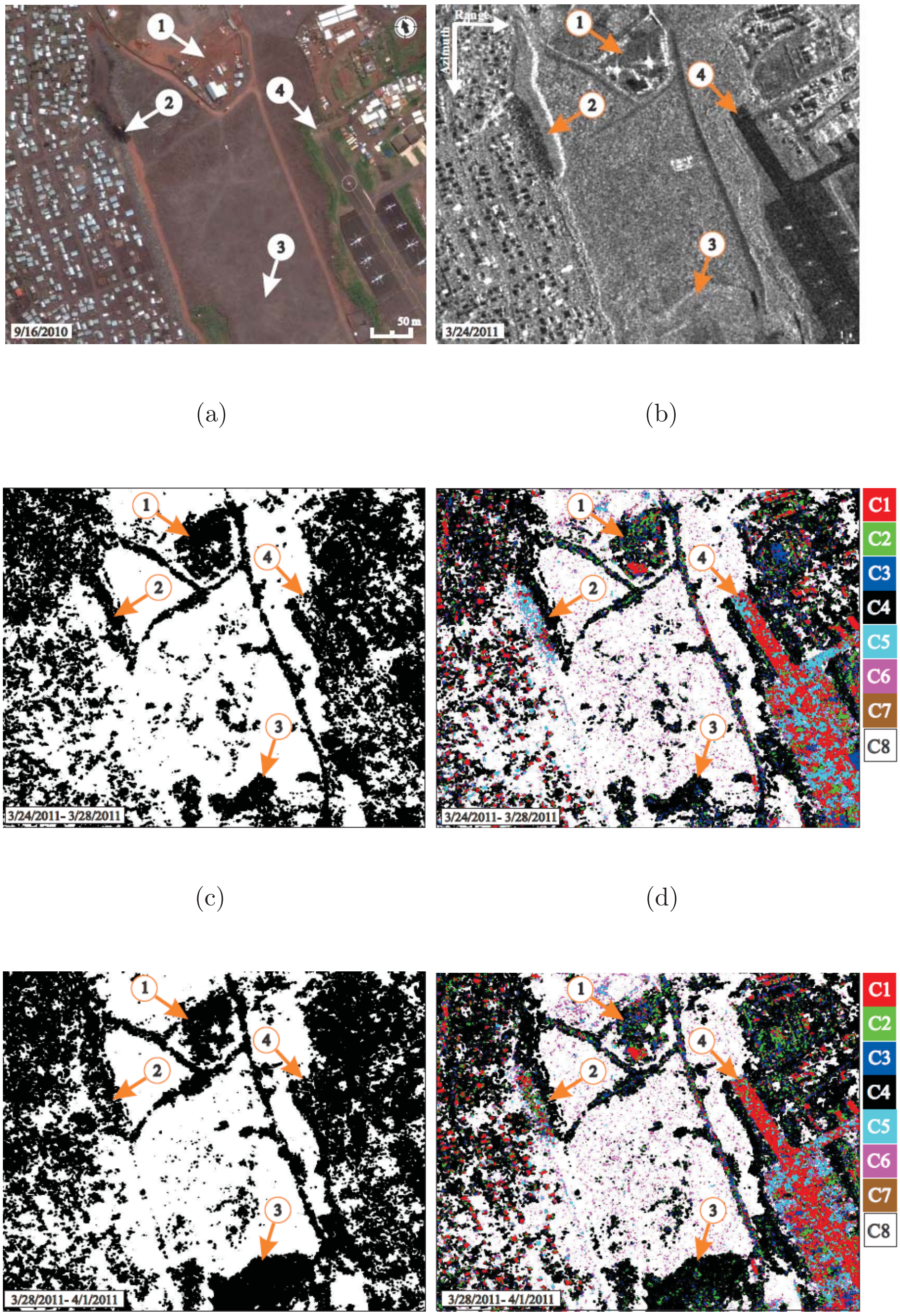

(a) (b)

(c) (d)

(e) (f)

Figure VI.14: Change classification results. (a) Visible image of the test site. (b) CSK SAR image intensity of 3/24/2011. (c) Coherence map of 3/24 and 3/28/2011. (d) Change classification result of 3/24 and 3/28/2011. (e) Coherence map of 3/28 and 4/1/2011. (f) Change classification result of 3/28 and 4/1/2011.

subtle changes, the classification contributes to the scene analysis. The large building in Figure VI.14(d)-1, and the most of the urban area on the left side of Figure VI.14-(d), are now classified as C1 instead of change in the coherence map.

Analysis of Figures VI.14-(c) and (d) show that in a sample environment without obstacles (i.e. open field in the center of Figure VI.14-(a)), the classification method identifies the man-made changes as of classes C2, C3 or C4 while the coherence map confuses all the changes in a single category. In a complex environment, e. g. the urban area in Figure VI.14-(a) and the airport runway in Figure VI.14(a)-4, the coherence map (in Figure VI.14(c)) becomes hard to interpret and the proposed change classification scheme (in Figure VI.14(d)) well identifies the man-made changes and contributes significantly to the overall scene understanding.

The results of Figures VI.14-(e) and (f), obtained by using an other image pair (March 28 and April 1, 2011) confirm the validity of the classes proposed in Table VI.1. All areas of the scene are classified in the same way in Figures VI.14-(d) and (f), except in the presence of man-made changes as in Figure VI.14(d)-3. In addition, the results show that the class C5 is encountered only in the specular surface and shadowed areas; it can be also assimilated to the class C1. Despite the complexity of the environment, the invalid classes C6 and C7 are rarely present in the scene. According to the results of Figures VI.14-(d) and (f), we conclude that the proposed classification method helps the monitoring of the man-made changes, which are mostly localized in the two areas indicated by (2) and (3).

VI.8 Summary

A comparative study of the classification results obtained with and without introducing the LFF information to the classification scheme has been performed. A set of high resolution CSK SAR data are selected for the validation process which concerns different environments. High resolution optical images are used in the validation process, and the SAR intensity images were used as ground truth. In a complex environment, the results show that the coherence map reveals changes but remains hard to interpret. The proposed change classification scheme identifies well the man-made changes, and contributes significantly to the overall scene analysis and understanding. The classification results, related to the various selected test sites, show that the use of the enhanced coherence map (using one of the two LFF-based methods) enhances the man-made change classes. The LFF-based cleaning method works well in wide areas, but remains limited in harbour environment where unmoved vehicles surrounded by changes are also cleaned. The classification results show also that the LFF-based adaptive method offers a better compromise between the enhancement of the change classes and the preservation of the small details. The results obtained using other image pairs confirm the validity of the proposed changed-unchanged classes. The proposed method is an improvement for the analysts in charge of the exploitation of information derived from radar imagery.

$\boxed{\text{CHAPTER VII}}$

CONCLUSION

We have studied the use of the SAR interferometry technique to detect subtle ground changes using high resolution SAR images. The main advantage of using SAR data is the fact that changes of the order of the centimeter significantly increase the interferometric phase variance in the impacted resolution element. These changes induce a decrease in InSAR coherence, which offers to coherent change detection methods the potential to detect very subtle scene changes that may remain undetectable using only SAR intensity images. InSAR coherence is widely used in the literature for mapping ground surface changes especially with the advent of satellite constellations such as COSMO-SkyMed that deliver high-resolution SAR images with fine spatial details and with a short temporal baseline. We started our work by developing an interferometric SAR process including interferogram formation, filtering and coherence estimation. At this stage, we have developed a new interferometric phase filter based on a subspace projection method that permits a better separation between the changed and unchanged coherence areas.
As shown in Chapter IV, the cause of the coherence bias, in addition to the presence of speckle in SAR data, is the appearance of highly coherent pixels inside changed areas which complicates the InSAR coherence map analysis and interpretation. Unfortunatly, there are no consistent studies concerning the coherent change detection using this type of data. For this reason, we have developed several detection methods for improving coherence map quality. We started by using some well known techniques such as MLD, OS, and CMLD. The results obtained using high resolution SAR data show that the CMLD outperforms the other two detectors. ROC curves have been used to quantify the detection performance. By studying the spatial correlation of the coherence data, we have also proposed the use of guard cells in the range direction to improve the detection performance. It has been shown in Section V.2 that the studied detectors need a large window size to detect all the changes, but this is done at the expense of small change detection.
In Section V.4, we have opted for another detection strategy based on the use of LFF (a measure of interferometric phase variability) to better analyze the InSAR coherence. In Section V.4.1, we have demonstrated the appropriateness of the LFF as a second change information source to improve the InSAR coherence map. Two LFF-based methods have been studied and tested. The first method, LFF-based cleaning method, eliminates aberrant values of the biased coherence and offers significant detection performance improvements. Nevertheless some isolated coherent targets are also characterized by high LFF values and then cleaned by this method. The second method, adaptive LFF-based method, offers less detection performance improvement compared to the LFF-based clean-

ing method but with the advantage of preserving isolated coherent targets. The results show that the LFF-based adaptive method offers the best compromise between detection performance and small change preservation.

The application of the enhanced InSAR coherence map to earthquake damage assessment was presented in Section V.5. We found it possible to map areas less affected by damages, although they are located in zones of extreme shaking (vertical acceleration of around 2 g).

As InSAR coherence is also affected by other decorrelation factors which are not caused by man-made activities, we have opted in our work for an additional change classification stage. The proposed classification scheme combines the improved InSAR coherence with the two corresponding SAR intensity images. It is important to note that the two SAR intensity images are not used to detect changes, but only to help the coherence map analysis and interpretation. A set of high resolution CSK SAR data is selected for the validation process. This set concerns different types of environments: an agricultural region in Maymana (Afganistan), a harbour in Zeebrugge (Belgium) and an airport in Goma (Democratic Republic of Congo). A comparative study of the classification results obtained with and without introducing the LFF information in the classification process is performed. High resolution optical images are used in the validation process and the SAR intensity images are used as ground truth. It was found that in a complex environment, the coherence map reveals changes but remains hard to interpret. The proposed change classification scheme well identifies the man-made changes and contributes significantly to the overall scene analysis and interpretation.

The results of the present work suggest that InSAR coherence improvement followed by a classification scheme permits a better characterization of the ground changes. This process is particularly suitable for border security application in desert areas.

VII.1 Summary of our contributions

Our contributions concern all InSAR process steps starting from signal processing with the development of a new subspace projection based phase filter, the improvement of detection techniques, and finally the exploitation of the results in a Geographical Information System.

- In [40], we propose a new projection subspace method for InSAR phase filtering. In addition to the phase noise reduction benefits, subspace projection based methods present the advantage of being robust in the presence of coregistration errors. Benefiting from the polynomial formulation of the cost function, the proposed method avoids the minimization process, thus leading to a fast and efficient interferometric phase filtering. The effectiveness of the method is verified using real SAR data. The results obtained using high resolution SAR data also show better separation between the changed and unchanged coherence areas, proving the appropriateness of the proposed method in man-made change detection.

- In [49], we study the detection performance of the three detectors MLD, OS, and CMLD which are applied to the coherence image in order to detect ground surface changes. The probability of detection and false alarm are evaluated experimentally using CSK images. It is shown that the proposed method, CMLD with guard cells only in the range direction, is robust and provides almost 4% higher detection probability in the case of low probability of false alarm.
- In [58], a new CCD method based on the use of the LFF components to clean coherence images has been presented. To make use of the LFF both in range and azimuth directions, a new statistics that measures phase variability to eliminate the aberrant highly coherent pixels inside changed areas is proposed. The proposed method is tested successfully in the case of high resolution CSK SAR images acquired over fields with agricultural activities. The results show an improvement of the detection performance of about 6% with respect to the method of space-averaging coherence while preserving the detection of subtle changes. We show that the proposed method is an improvement for the analysts in charge of the vectorization of information derived from radar imagery inside a Geographical Information System.
- The SAR interferometry technique is used to detect areas affected by a strong earthquake in Christchurch City. These areas remain coherent while patches around them are incoherent. Enhanced InSAR coherence images allow an efficient delineation of their boundaries. Ten-centimeter resolution color orthophotography and field data collections confirm the existence of the sites where the effects of soil liquefaction are absent. We show that the regions which remain coherent are shock wave absorption zones. Damping capabilities seem reproducible from a quake to another. We suggest a new approach to refine prediction models for economic losses and propose an alternative method for earthquake damage assessment in civil engineering.

- [17] deals with the development and the validation of coherent change detection and classification method. The enhanced InSAR coherence is combined with the two corresponding SAR intensity images to build a CCD map using a simple change classification scheme. The test area of interest concerns the Goma airport, which is a flat and busy test site. It is shown that the proposed change classification scheme well identifies the man-made changes and contributes significantly to the overall scene analysis and understanding. The results obtained using other image pairs confirm the validity of the proposed changed and unchanged classes.

VII.2 Future work

For future work, we propose:

- the investigation of the unsupervised methods to separate changed and unchanged areas in InSAR coherence images.

- the analysis of the influence of the intermediate thresholding of the InSAR coherence on the quality of the final CCD map.

- the application of data fusion algorithms for the development of new classification schemes based on external data sources such as optical images, vegetation maps,..., etc.

- the investigation of the potential of polarimetric SAR interferometry for the SAR coherence optimisation.

Bibliography

[1] Rignot E. J. Change detection techniques for ers-1 sar data. *IEEE Trans. on Geosci. Remote Sens.*, Vol. 31(4):896–906, 1993.

[2] Massonnet D. and Feigl K. L. Radar interferometry and its applications to changes in the earth's surface. *Review of Geophysics*, Vol. 36(4):441–500, 1998.

[3] Lopes A., Nezry E., Touzi R., and Laur H. Structure detection and statistical adaptive filtering in sar images. *International Journal of Remote Sensing*, Vol. 14(9):1735–1758, 1993.

[4] Preiss M. Scene coherency at x-band from repeat pass polarimetric interferometry. *Proc. IEEE Int. Geosci. Remote Sens. Symp.*, pages 1081–1084, 2005.

[5] Preiss M., Gray A., and Stacy N. J. S. Detecting scene changes using synthetic aperture radar interferometry. *IEEE Trans. on Geosci. Remote Sens.*, Vol. 44(8):2041–2054, 2006.

[6] Goldstein R., Zebker H., and Werner C. Satellite radar interferometry: Two-dimensional phase unwrapping. *Radio Science*, Vol. 23(4):713–720, 1988.

[7] Just D. and Bamler R. Phase statistics of interferograms with applications to synthetic aperture radar. *Applied Optics*, Vol. 33(20):4361–4368, 1994.

[8] Zebker H. A. and Villasensor J. Decorrelation in interferometric radar echoes. *IEEE Trans. on Geosci. Remote Sens.*, Vol. 30(5):950–959, 1992.

[9] Zabker H., Rosen P. A., Hansley S., and Mouginis-Mark P.J. Analysis of active lava flows on kilauea volcano, haweii, using sir-c radar correlation measurements. *Geology*, Vol. 24(5):495–498, 1996.

[10] Dietterich H. R., Poland M. P., Schmidt D. A, Cashman K. V., Sherrod D. R., and Espinosa A. T. Tracking lava flow emplacement on the east rift zone of kilauea, hi., with synthetic aperture radar coherence. *Geochemistry, Geophysicsn, Geosystems*, Vol. 13(5):495–498, 2012.

[11] Simons M., Fialko Y., and Rivera L. Coseismic deformation from the 1999 mw 7.1 hector mine, california, earthquakes as inferred from insar and gps observations. *Bulletin of the Seismological Society of America*, Vol. 92(4):1390–1402, 2002.

[12] Fielding E. J., Talebian M., Rosen P. A., Nazari H., Jackson J. A., Ghorashi M., and Walker R. Surface ruptures and building damage of the 2003 bam, iran, earthquake mapped by satellite synthetic aperture radar interferometric correlation. *J. Geophysi. Res.*, Vol. 110(B3):B03302, 2005.

[13] Hoffmann J. Mapping damage during the bam (iran) earthquake using interferometric coherence. *Int. J. of Remote Sens.*, Vol. 28(6):1199–1216, 2007.

[14] Milisavljevic N., Closson D., and Bloch I. Detecting potential human activities using coherent change detection. *in proc. Image Processing Theory, Tools and Applications (IPTA), 2nd Int. Conf. on*, pages 482–485, July, 2010.

[15] Touzi R., Lopes A., Bruniquel J., and Vachon P. W. Coherence estimation for sar imagery. *IEEE Trans. on Geosci. Remote Sens.*, Vol. 37(1):135–149, 1999.

[16] Martinez C. L. and Pottier E. Coherence estimation in synthetic aperture radar data based on speckle noise modeling. *Applied Optics*, Vol. 46(4):544–558, 2007.

[17] Bouaraba A., Milisavljevic N., Acheroy M., and Closson D. Change detection and classification using high resolution sar interferometry. *Chapter in the book entitled: Land Applications of Radar Remote Sensing*, INTECH Edition, ISBN: 980-953-307-1017-3, 2014.

[18] Skolnik M. I. *Radar Handbook*. McGraw-Hill, 1970.

[19] Ulaby F. T., Moore R. K., and Fung A. K. *Microwave remote sensing: active and passive*. Artech House Inc., 1981.

[20] Curlander J. C. and McDounough R. N. *Synthetic Aperture Radar, Systems and Signal Processing*. John Wiley & Sons, 1991.

[21] Thompson T. W. A user's guide for the nasa/jpl synthetic aperture radar and the nasa/jpl l- and c-band scatterometers. *JPL Publication*, pages 83–38, 1986.

[22] Lillesand T. and Kiefer R. *Remote sensing and image interpretation:fifth edition*. John Wiley & Sons, 2004.

[23] Massonnet D. and Souyris J. C. *Imaging with Synthetic Aperture Radar: first edition*. EFPL Press, 2008.

[24] Goodman J. W. Some fundamental properties of speckle. *Journal of Optical Society America*, Vol. 66(11):1145–1150, 1976.

[25] Cloude S. R. *Polarisation: Applications in Remote Sensing*. Oxford University Press, 2009.

[26] Bamler R. and Hartelet P. Synthetic aperture radar interferometry. *Inverse Problems: IOP Publishing LTD*, Vol. 14:123–137, 1998.

[27] Graham L. C. Synthetic interferometer radar for topographic mapping. *Proceeding of IEEE*, Vol. 62:763–768, 1974.

[28] Gabriel A. K. and Goldstein R. M. Crossed orbit interferometry: theory and experimental results from sir-b. *International Journal of Remote Sensing*, Vol. 9:857–872, 1988.

[29] Hanssen R. F. *Radar interferometry: data interpretation and error analysis*. Kluwer Academic Publishers, 2001.

[30] Geudtner D. and Schwabisch M. An algorithm for precise reconstruction of insar imaging geometry: Application to "flat earth" phase removal, phase-to-height conversion, and geocoding of insar-derived dems. *in Proc. of European Conference on Synthetic Aperture Radar (EUSAR1996).*, 1996.

[31] Moreira. J. X-sar interferometry: First results. *IEEE Trans. on Geosci. Remote Sens.*, Vol. 33(4):950–956, 1995.

[32] Candeias A. L. B. Interferogram phase noise reduction using morphological and modified median filters. *Geosci. and Remote. Sens. Symp. (IGARSS), 1995 IEEE International*, Vol. 1:166–168, 1995.

[33] Geudtner D. and Winter R. Sar-interferometry with ers-1 data. *in Proc. Progress In Electromegnetic Research Symposium*, 1994.

[34] Kampes B. M. *et al.* Baran I., Stewart M. P. A modification to the goldstein radar interferogram filter. *IEEE Trans. on Geosci. Remote Sens.*, Vol. 41(9):2114–2118, 2003.

[35] Zhenfang L., Zheng B., and Zhiyong S. A joint image coregistration, phase noise suppression, and phase unwrapping method based on subspace projection for multi-baseline insar systems. *IEEE Trans. on Geosci. Remote Sens.*, Vol. 45(3):584–591, 2007.

[36] Hai L. and Renbiao W. An estimation method for insar interferometric phase using correlation weight joint subspace projection. *EURASIP Journal on Advances in Signal Processing*, Vol. 27:1–11, 2013.

[37] Guisheng L. and Hai L. Estimation method for insar interferometric phase based on generalized correlation steering vector. *IEEE Trans. on Aero. and Elect. Syst.*, Vol. 46(3):1389–1403, 2010.

[38] Schmidt R. O. Multiple emitter location and signal parameter estimation. *in Proc. RADC Spectral Estimation Workshop*, pages 243–258, 1979.

[39] Friedlander B. The root-music algorithm for direction finding with interpolated arrays. *Signal Processing*, Vol. 30:15–25, 1993.

[40] Bouaraba A., Belhadj-Aissa A., Borghys D., Acheroy M., and Closson D. Insar phase filtering via joint subspace projection method: Application in change detection. *IEEE Geosc. and Remote Sens. Letters*, Vol. 11(11), DOI:10.1109/LGRS.2014.2310493, 2014.

[41] Rodriguez E. and Martin J. M. Theory and design of interferometric synthetic aperture radars. *IEE Proc.*, Vol. 139(4):147–159, 1992.

[42] Ferretti A. Permanent scatterers in sar interferometry. *IEEE Trans. on Geosci. Remote Sens.*, Vol. 39(1):8–20, 2001.

[43] Berardino P. A new algorithm for surface deformation monitoring based on small baseline differential interferograms. *IEEE Trans. on Geosci. Remote Sens.*, Vol. 40(11):2375–2383, 2002.

[44] Joughin I. R. and Winebrenner D. P. Effective number of looks for a multilook interferometric phase distribution. *in:International Geoscience and Remote Sensing Symposium*, pages 2276–2278, 8-12 August 1994.

[45] Gatelli F., Guamieri A., Parizzi M., Pasquali P., Prati C., and Rocca F. The wavenumber shift in sar interferometry. *IEEE Trans. on Geosci. Remote Sens.*, 32(4):855–865, 1994.

[46] Teng W. and Mingsheng L. and Daniele P. Insar coherence-decomposition analysis. *IEEE Geosci. and Remote Sens. Letters*, 1(7):156–160, 2010.

[47] Hagberg J. O., Ulander L. M. H., and Askne J. Repeat-pass sar interferometry over forested terrain. *IEEE Trans. on Geosci. Remote Sens.*, 2(33):331–340, 2010.

[48] Vasile G., Petillot I., and Bolon P. High-resolution sar interferometry: Estimation of local frequencies in the context of alpine glaciers. *IEEE Trans. on Geosci. Remote Sens.*, 46(4):1079–1090, 2008.

[49] Bouaraba A., Younsi A., Belhadj-Aissa A., Acheroy M., Milisavljevic N., and Closson D. Robust techniques for coherent change detection using cosmo-skymed sar images. *Progress In Electromagnetics Research M*, Vol. 22:219–232, 2012.

[50] Rohling H. Radar cfar thresholding in clutter and multiple target situations. *IEEE Trans. on Aeros. and Elect. Syst.*, Vol. 19(4):608–621, 1983.

[51] Rickard J. T. Adaptive detection algorithms for multiple target situations. *IEEE Trans. on Aeros. and Electr. syst.*, Vol. 13(10):338–343, 1977.

[52] Spagnolini U. 2-d phase unwrapping and instantaneous frequency estimation. *IEEE Trans. on Geosci. Remote Sens.*, Vol. 33(5):579–589, 1995.

[53] Trouvé E., Caramma M., and Maitre H. Fringe detection in noisy complex interferograms. *Appl. Opt.*, Vol. 35(20):3799–3806, 1996.

[54] Stramondo S., Kyriakopoulos C., Bignami C., Chini M., Melini D., Moro M., Picchiani M., Saroli M., and Boschi E. Did the september 2010 (darfield) earthquake trigger the february 2011 (christchurch) event ?. *Nature, Scientific Reports*, Vol. 1(98), 2011.

[55] Atzori S., Tolomei C., Antonioli A., Merryam Boncori J. P., Bannister S., Trasatti E., Pasquali P., and Salvi S. The 2010-2011 canterbury, new zealand, seismic sequence: Multiple source analysis from insar data and modeling. *Journal of Geophysical Research*, (117), 2012.

[56] Fry B., Benites R., and Kaiser A. The character of accelerations in the mw 6.2 christchurch earthquake. *Seismological Research Letters*, (82):846–852, 2012.

[57] Lee J. S. Digital image enhancement and noise filtering by use of local statistics. *IEEE Trans. on Pattern Analysis and Machine Intelligenc*, Vol. PAMI-2:165–168, 1980.

[58] Bouaraba A., Borghys D., Belhadj-Aissa A., Acheroy M., and Closson D. Improving ccd performance by the use of local fringe frequencies. *Progress In Electromagnetics Research C*, Vol. 32:123–137, 2012.

APPENDIX

APPENDIX A

MUSIC FOR LFF ESTIMATION

The MUltiple SIgnal Classification (MUSIC) method [53] used to estimate the 2-D LFF (f_x, f_y) of SAR interferograms on boxcar windows is based on the structure of a 'signal vector' resulting from the concatenation of the lines of a 2-D complex sine-wave signal $s(k,l) = e^{j\phi(k,l)} = e^{j[2\pi(kf_x + lf_y)]}$. If this signal is observed on a $N \times N$ window, the size of the signal vector v_s is N^2 and the size of its covariance matrix Γ_s is $N^2 \times N^2$. With this model, Γ_s can be written as

$$\Gamma_s = \begin{bmatrix} 1 \\ e^{j2\pi f_x} \\ e^{j2\pi 2f_x} \\ \vdots \\ e^{j2\pi(N-1)f_x} \\ --- \\ e^{j2\pi f_y} \\ e^{j2\pi(f_x+f_y)} \\ e^{j2\pi(2f_x+f_y)} \\ \vdots \\ e^{j2\pi((N-1)f_x+f_y)} \\ --- \\ \vdots \end{bmatrix} [v_s^H] \tag{A.1}$$

Accordingly, this covariance matrix presents a $N \times N$ block structure: inside the blocks, lines are equal to the previous lines multiplied by $a_x = e^{j2\pi f_x}$ and each block is equal to the previous block multiplied by $a_y = e^{j2\pi f_y}$.

To determine frequency vectors by use of MUSIC one needs to diagonalize of Γ_s. Orthogonal bases of signal space and noise space are built according to the P largest eigenvalues. Then, the expected frequencies $(f_x,\ f_y)$ can be estimated by P maximizations of the projection of $v_s(f_x,\ f_y)$ on noise space β_n. One can perform the minimization step by evaluating the pseudospectrum

$$J = 1/v_s^H(f_x, f_y)\beta_n\beta_n^H v_s(f_x, f_y) \tag{A.2}$$

on a fine grid of the $[-0.5, 0.5] \times [-0.5, 0.5]$ frequency domain.

Inside one block, the 2-D LFF of SAR interferograms may by estimated by the following equations [53]:

$$\begin{aligned} f_x &= v_1^H v_2 / v_1^H v_1 \\ f_y &= v_1^H v_4 / v_1^H v_1 \end{aligned} \tag{A.3}$$

where $v_i = \Gamma_s(1:N, i), i = 1$, 2 and 4.

The final LFF estimates may correspond to the average of the values obtained in the $N \times N$ blocks.

Azzedine BOUARABA was born in Tizi-ouzou, Algeria in 1980. He graduated in electronic engineering in 2005, received the magister degree in 2008 and his doctorate degree in electronic engineering in 2014 from 'Ecole Militaire Polytechnique' of Algeria and from 'Royal Military Academy' of Belgium. His general interests are radar remote sensing, synthetic aperture radar Interferometry, change detection, digital elevation model. Currently, he is a member of the radar and microwaves laboratory at 'Ecole Militaire Polytechnique'.

Abstract

The work presented in this thesis concerns the application of Synthetic Aperture Radar Interferometry (InSAR) for mapping subtle ground changes. The changes of interest correspond to those caused by man-made activities such as vehicle movement or to those related to natural disaster such as earthquake damages. Various methods have been developed and tested for improving the InSAR coherence estimation. In order to better identify the man made changes of interest, a particular interest was given to the change classification step. Various high resolution SAR image pairs were used for the validation process.

Résumé

Le travail présenté dans cette thèse concerne l'application de l'interferometrie radar SAR pour la cartographie des changements à la surface imagée. Les changements utiles sont ceux causés par une activité humaine telle que les traces de véhicules ou ceux provoqués par un événement naturel telle que les dégâts après un tremblement de terre. Plusieurs méthodes ont été développées et testées pour l'amélioration de l'estimation de la cohérence InSAR. Un intérêt particulier a été accordé au développement d'un schéma de classification afin de mieux identifier les changements d'origine humaine. Plusieurs paires d'images SAR à haute resolution on été utilisées durant l'étape de validation.

Key words (Mots clés)

SAR interferometry, coherence, coherent change detection, CosmoSky-Med.